Entanglement of Distant Atoms
for Quantum Networks

Tim Bernardus Maria van Leent

München 2023

Entanglement of Distant Atoms
for Quantum Networks

Tim Bernardus Maria van Leent

Dissertation at the Faculty of Physics
of the Ludwig-Maximilians-Universität München

by Tim Bernardus Maria van Leent
from Amstelveen, the Netherlands

München 06.03.2023

Abstract

Quantum networks promise many revolutionary applications, such as secure quantum communication and distributed quantum computing. Central to these networks is the ability to distribute entanglement between distant nodes using photonic channels. Various physical candidates are under active research to serve as quantum system in the nodes. Here, we employ neutral single-atoms to realise a quantum network link between two independent nodes located in buildings 400 m apart. This thesis focusses on two topics, namely, the demonstration of a device-independent quantum key distribution protocol and entanglement distribution between the nodes over tens of kilometres of telecom fibre employing quantum frequency conversion.

Device-independent quantum key distribution enables the generation of secret keys over an untrusted channel using uncharacterized and potentially untrusted devices. The proper and secure functioning of the devices can be certified by a statistical test probing a Bell inequality, thereby leaving only the integrity of the users' locations to be guaranteed by other means. The realisation of device-independent protocols, however, is challenging—mainly because it is difficult to establish high-quality entangled states between two remote locations with high detection efficiency. Here we present an experimental system that allows for quantum key distribution in a fully device-independent setting. By achieving an event-ready atom-atom entanglement fidelity of $\mathcal{F} \geq 0.892(23)$, we observe a significant violation of a CHSH Bell inequality of $S = 2.578(75)$—above the classical limit of 2—and a quantum bit error rate of 0.078(9). For the implemented random key-bases protocol, this results in a secret key rate of 0.07 bits per entanglement generation event in the asymptotic limit, and thus demonstrates the system's capability to generate secret keys in a device-independent setting.

The second topic is long-distance entanglement distribution over optical fibres, for which it is essential to operate at telecom wavelengths to overcome high attenuation losses. Most quantum system under active research, however, operate in the visible or near infrared. We employ polarization-preserving quantum frequency conversion in both nodes to transform the wavelength of the photons that are entangled with the atoms from 780 nm to the telecom S band. Enabled by an unprecedented external device conversion efficiency of 57% and minimal induced noise, we report on the observation of atom-photon and heralded atom-atom entanglement generated over telecom fibre links with a length up to 33 km. We analyse the entanglement fidelity for different fibre link lengths and show that for longer links the fidelity is mainly limited by atomic decoherence. The atom-atom entanglement is analysed only after receiving the heralding signal including a time delay to account for classical communication times between the nodes to simulate a realistic quantum network link scenario.

The results presented in this thesis pave the way towards the ultimate form of quantum secure communications in future quantum networks and are a milestone on the road to realise long-distance quantum network links.

Zusammenfassung

Quantennetze versprechen viele revolutionäre Anwendungen, wie zum Beispiel sichere Quantenkommunikation und verteiltes Quantencomputing. Im Mittelpunkt dieser Netze steht die Fähigkeit, die Verschränkung zwischen weit entfernten Knoten über photonische Kanäle zu verteilen. Verschiedene physikalische Kandidaten werden aktiv erforscht, um als Quantensystem in den Knoten zu dienen. Hier verwenden wir neutrale Einzelatome, um eine Quantennetzwerkverbindung zwischen zwei unabhängigen Knoten zu realisieren, die sich in 400 m voneinander entfernten Gebäuden befinden. Diese Arbeit konzentriert sich auf zwei Themen, die Demonstration eines geräteunabhängigen Quantenschlüsselverteilungsprotokolls und die Verschränkungsverteilung zwischen den Knoten über Dutzende von Kilometern Telekommunikationsfaser mit Hilfe von Quantenfrequenzumwandlung.

Die geräteunabhängige Quantenschlüsselverteilung ermöglicht die Erzeugung geheimer Schlüssel über einen nicht vertrauenswürdigen Kanal unter Verwendung nicht charakterisierter und potenziell nicht vertrauenswürdiger Geräte. Das ordnungsgemäße und sichere Funktionieren der Geräte kann durch einen statistischen Test mit einer Bell-Ungleichung bestätigt werden, so dass nur noch die Integrität der Nutzerstandorte mit anderen Mitteln garantiert werden muss. Die Realisierung geräteunabhängiger Protokolle stellt jedoch eine Herausforderung dar— hauptsächlich da es schwierig ist hochwertige verschränkte Zustände zwischen zwei entfernten Orten mit hoher Detektionseffizienz herzustellen. Hier stellen wir ein experimentelles System vor, das die Verteilung von Quantenschlüsseln in einem völlig geräteunabhängigen Szenario ermöglicht. Indem wir eine ereignisbereite Atom-Atom-Verschränkungstreue von $\mathcal{F} \geq 0.892(23)$ erreichen, beobachten wir eine signifikante Verletzung der CHSH-Bell-Ungleichung von $S = 2.578(75)$—oberhalb der klassischen Grenze von 2—und eine Quantenbitfehlerrate von $0.078(9)$. Für das implementierte Protokoll mit Zufallsschlüsseln ergibt sich daraus eine Geheimschlüsselrate von 0.07 Bit pro Verschränkungsereignis im asymptotischen Limit, was die Fähigkeit des Systems zur Erzeugung von Geheimschlüsseln in einem geräteunabhängigen Szenario demonstriert.

Das zweite Thema ist die Verschränkungsverteilung über große Entfernungen mit optische Fasern, für die es unerlässlich ist, bei Telekommunikationswellenlängen zu arbeiten, um hohe Dämpfungsverluste zu überwinden. Die meisten Quantensysteme, die derzeit erforscht werden, arbeiten jedoch im sichtbaren Licht oder nahen Infrarot. Wir verwenden eine polarisationserhaltende Quantenfrequenzumwandlung in beiden Knotenpunkten, um die Wellenlänge der mit den Atomen verschränkten Photonen von 780 nm in das S-Band der Telekommunikation zu transformieren. Dank einer beispiellosen Effizienz der externen Konversion von 57% und minimalem induziertem Rauschen berichten wir über die Beobachtung von Atom-Photon- und angekündigter Atom-Atom-Verschränkung, die über Telekom-Glasfaserverbindungen mit einer Länge von bis zu 33 km erzeugt wurde. Wir analysieren die Verschränkungstreue für verschiedene Glasfaserverbindungslängen und zeigen, dass diese bei längeren Verbindungen hauptsächlich

durch die atomare Dekohärenz begrenzt ist. Die Atom-Atom-Verschränkung wird erst nach dem Empfang des Ankündigungssignals analysiert, das eine Zeitverzögerung enthält, um die klassischen Kommunikationszeiten zwischen den Knoten zu berücksichtigen und ein realistisches Szenario einer Quantennetzwerkverbindung zu simulieren.

Die in dieser Arbeit vorgestellten Ergebnisse ebnen den Weg zur ultimativen Form der sicheren Quantenkommunikation in zukünftigen Quantennetzwerken und sind ein Meilenstein auf dem Weg zur Realisierung von Quantennetzwerkverbindungen über große Entfernungen.

List of Publications

Publications resulted from work presented in this thesis

- W. Zhang, **T. van Leent**, K. Redeker, R. Garthoff, R. Schwonnek, F. Fertig, S. Eppelt, W. Rosenfeld, V. Scarani, C. C.-W. Lim, and H. Weinfurter.
  A device-independent quantum key distribution system for distant users.
  Nature **607**, 687–691 (2022).

  Contributions: TvL, WZ, KR, RG, RS, CL, and HW designed the experiment. TvL, WZ, RG, and FF performed the experiment. TvL analyzed the data. RS and CL performed the key rate simulations. TvL, KR, VS, CL, and HW prepared the manuscript based on input from all other authors. WZ, TvL, KR, and RG contributed equally.

- V. Zapatero, **T. van Leent**, R. Arnon-Friedman, W.-Z. Liu, Q. Zhang, H. Weinfurter, and M. Curty.
  Advances in device-independent quantum key distribution.
  npj Quantum Information **9**, 10 (2023).

  Contributions: All authors discussed the work together and decided the structure and contents of the paper. VZ, TvL, RAF, and WZL wrote the manuscript. All authors critically read and revised it. MC supervised the project.

- **T. van Leent**, M. Bock, R. Garthoff, K. Redeker, W. Zhang, T. Bauer, W. Rosenfeld, C. Becher, and H. Weinfurter.
  Long-distance distribution of atom-photon entanglement at telecom wavelength.
  Physical Review Letters **124**, 010510 (2020).

  Contributions: TvL, MB, and RG performed the experiment and analysed the data. MB designed and constructed the QFC setup. TvL prepared the manuscript based on input from all other authors. TvL, MB, and RG contributed equally.

- **T. van Leent**, M. Bock, F. Fertig, R. Garthoff, S. Eppelt, Y. Zhou, P. Malik, M. Seubert, T. Bauer, W. Rosenfeld, W. Zhang, C. Becher, and H. Weinfurter.
  Entangling single atoms over 33 km telecom fibre.
  Nature **607**, 69–73 (2022).

  Contributions: MB, CB, TvL, WZ, WR, and HW devised the project. TvL, WZ, FF, SE, YZ, and PM performed the experiments. TvL analysed the data. MB designed and constructed the QFC sytems, assisted by TB. RG desinged and constructed the fluorescence collection setups in both nodes, assisted by MS. TvL prepared the manuscript and all authors contributed to the final version. TvL, MB, and FF contributed equally.

Further publications

- M. Bock, C. Becher, F. Fertig, and **T. van Leent**.
  Verschränkte Atome über eine 33 km Glasfaserstrecke.
  Physik in unserer Zeit **53**, 6 (2022).

- Y. Zhou, P. Malik, F. Fertig, M. Bock, **T. van Leent**, W. Zhang, C. Becher, and H. Weinfurter.
  Robust quantum memory for atom-photon entanglement over 101 km optical fiber.
  To be published (2023).

Contents

Chapter 1

Introduction

The development of quantum mechanics laid the theoretical foundation for a drastically different, but very accurate, description of nature. It is a mathematical framework based on a set of relatively simple rules that have interesting yet famously unintuitive consequences. The uncertainty principle, for example, introduces a fundamental limit to the measurement accuracy of certain pairs of observables, such as the position and momentum of a particle. Or, maybe even more striking, the concept of entanglement: describing a quantum state shared between multiple particles that is non separable, even when the particles themselves are spatially separated. This non-local and non-realistic description of nature, however, left many unsatisfied, leading to a dispute over multiple decades about the interpretation and correctness of quantum theory.

The most acclaimed effort to combine quantum mechanics with a local realistic world view is by extending the theory with so called local hidden variables [1], aiming to explain the probabilistic features by underlying variables. In 1964, John Bell proposed an experimental test predicting different outcomes for quantum mechanics and local hidden variable theories, allowing to disprove all local realistic theories using a statistical argument [2]. Not much later, the first experimental Bell test were realized agreeing with quantum mechanics [3, 4]. These tests, however, all relied on system assumptions due to experimental imperfections, opening loopholes for more advanced local hidden variable theories. Only recently, experiments were conducted showing a violation of a Bell inequality while having the major loopholes closed, thus contradicting all local realistic theories [5–9].

Today, quantum mechanics is not only a fundamental or theoretical annotation, but quantum technologies have matured and prove to be a valuable resource allowing users to perform tasks that are not possible by classical means. Hand-in-hand with the gain in experimental control of individual and coherent many-body quantum systems, more applications of quantum technologies are introduced and complete fields of research emerged. Quantum systems consisting of many particles are now used to simulate complex problems—as envisioned four decades ago by Richard Feynman [10]—typically for solid-state systems, for example, quantum simulators based on neutral atoms [11, 12] successfully studied quantum phase transitions [13]. More generally, the field of quantum computation leverages the quantum properties of superposition and entanglement to perform calculations that a classical computer cannot perform [14–16]. The development of novel algorithms, such as Shor's algorithm for factoring integers [17], shows the revolutionary potential of these quantum computers. Recently, experimental efforts lead to the development of a superconducting qubit based apparatus that, for the first time, outperformed a classical computer in a specific computational task [18]. Another category of applications is being studied in the emerging fields of quantum metrology [19, 20], where optical atomic clocks

are the worlds most accurate time keepers [21], and quantum sensing, where correlations between photons boost the detection of faint objects [22]. In the field of quantum communication, the distribution of quantum states is exploited for cryptographic applications [23]. Over the last two decades, quantum key distribution developed from experimental demonstrations over a 1 km long spooled fibre inside a laboratory [24], to the realization of a 4600 km long network connecting various cities for key distribution using trusted nodes via satellites and fibres [25], and commercially available quantum key distribution systems. In many of the applications mentioned above, entanglement between particles plays a pivotal role. Sharing of high-quality entanglement between distant quantum devices has the potential to even further increases the range and impact of these quantum technologies.

Quantum networks will facilitate the distribution of entangled states between distant locations [26]. These networks are subject to extensive theoretical and experimental research and consist out of stationary quantum nodes that can distribute, store, and process quantum information, as illustrated in Figure 1.1. Fundamental in the distribution process are interconnects to exchange the quantum states—efficiently mediated by photons. In the current vision of a worldwide quantum network two methods are used in parallel to realize these photonic quantum channels [27]: one uses free-space links, employing, for example, satellites to distribute entanglement over thousands of kilometres, and the other uses optical fibres employing the already existing fibre infrastructure. Accordingly, entanglement is distributed between nodes without direct interaction of the quantum systems, using entanglement swapping and quantum teleportation protocols [28, 29]. Furthermore, in case two network nodes share several pairs of entangled quantum systems, infidelities in the quality of the states can be compensated for using entanglement distillation [30], i.e., multiple low-quality entangled pairs can be purified to one high-quality entangled pair. While photons are the ideal carrier of quantum information due to the high travel speed and non-interactive nature, single photon losses in the quantum channel are inevitable and cause the communication efficiency of a channel to decrease exponentially with the channel length. To overcome this exponential decay, the concept of quantum repeaters was introduced [31, 32]. In a quantum repeater scheme, two distant end-nodes are not entangled directly, but the quantum channel is divided into various segments, which are first entangled individually (see Figure 1.1). Thereafter, the entanglement is transferred to the end-nodes using entanglement swapping protocols, resulting in a polynomial decrease in communication efficiency with the total channel length, thus enabling for large-scale quantum networks.

Many quantum network applications have been proposed over the last years—and stimulated by recent experimental progress it is likely that more will follow. Quantum computers, for example, can use the distribution of entanglement to combine multiple quantum processors and allow for joint calculations. This directly provides a modular approach to quantum computing: building a large quantum processor out of many smaller ones solves problems like qubit cross-talk and restricted space [33]. Another application is blind quantum computing—allowing a user to perform computations on a remote quantum computer without compromising full information about the computing task [34, 35]. Furthermore, distributed entanglement has the potential to advance global timekeeping [36], e.g., for accurate positioning systems, to give all users direct access to precise time. One more important application, especially for this thesis, lays in cryptography. When quantum networks deterministically provide high-quality entanglement between remote locations, it will be possible to implement so called device-independent quantum key distribution protocols [37–40]. So far, these are the most advanced key distribution protocols that not only secure the quantum channel based on the laws of physics, but simultaneously test the proper functioning of the employed device and hence are secure against implementation
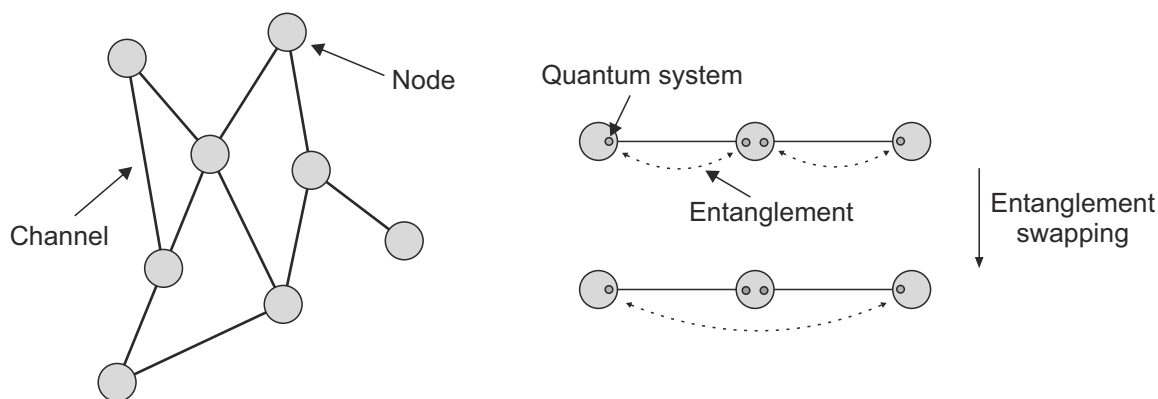
Figure 1.1: **Schematic of a quantum network and quantum repeater scheme.** On the left, schematic of a quantum network containing quantum nodes that are connected and can be entangled via the quantum channels. Every node contains one or more quantum systems that allow to store, process, and distribute quantum information. The quantum channels are formed by the exchange of photons. On the right, a schematic of a quantum repeater scheme with two end-nodes and one middle-node is depicted. First, two pairs of quantum systems, located in two end-nodes and a middle-node, are entangled. Thereafter, the entangled is swapped to the end-nodes by a projective measurement of the two quantum systems in the middle-node.

flaws.

The requirements to serve as quantum system in quantum network nodes are very demanding and various physical platforms are under active research [41, 42]. The most fundamental capability for such quantum systems is to generate or transfer entanglement between light and matter, which has been realised for various systems, such as, neutral single-atoms [43], ions [44, 45], atomic ensembles [46–48], vacancy centres in diamond [49], semiconductor quantum dots [50, 51], or rare earth ions in solids [52, 53]. The generation of entanglement between nodes can be achieved by employing controlled light-matter interactions, e.g., by storing the state of a single photon entangled with a first node into a second node [54], or via entanglement swapping using two entangled light-matter pairs [55–57]. For efficient entanglement distribution in quantum networks, however, the entanglement needs to be generated at high rate, with high fidelity, and with long coherence times. In particular, to overcome the probabilistic nature of the distribution process and allow for deterministic generation of entanglement, the generation rate should exceed the entangled-state decoherence rate [58]. For this, the generation rates were improved by the implementation of optical cavities to increase photon collection efficiencies [59–61], resulting in close-to-optimal collection efficiencies for, e.g., ion-photon interfaces [62], and for many platforms coherence times have been reported that exceed hundreds of milliseconds [63–65] up to several hours [66]—thus approaching the requirements for large-scale quantum networks. Regarding the entanglement fidelity, two-qubit gate fidelities above 99% have been constrained to intra-node operations only, employing, e.g., micrometre spaced ions [67, 68] or atoms [69]. However, not being limited fundamentally, two-node operations start to approach the intra-node ones by reaching fidelities as high as 96% between nodes separated by 2 m [70]. To further increase fidelities entanglement distillation is a promising solution, which was realised in a two-node network [71]. Very recently, these theoretical and experimental efforts resulted in the realization of the first three-node network using NV-centers with a maximum node distance of 20 m [72] and the demonstration of techniques to non-destructively probe and maintain coherence of two-node

entangled states using single-atoms over a distance of 60 m [73].

Neutral single-atoms—as used in this work—are trapped in small volume optical dipole traps that allow for the individual storage and control of the atom—as first realized in the early 2000s using the alkali atoms cesium [74, 75] and rubidium [76]. Lately, also alkaline-earth atoms were trapped in optical tweezers [77, 78], and with two instead of one valence electron potentially opening up even more applications. Over the last years, various critical properties required to serve in a quantum network node have been demonstrated, such as atom-photon entanglement generation and the observation of heralded atom-atom entanglement with high fidelity over distances up to 400 m [8, 73, 79]. A big advantage of neutral atoms above other platforms is the ability to relatively simply scale up the number of traps by introducing multiple, reconfigurable optical dipole trap beams or by the generation of multiple trap sites in an optical lattice. The deterministic loading of hundreds of micrometre spaced atoms was demonstrated using spatial light modulators [80, 81] or acousto-optic deflectors [82]. This scalability is in sharp contrast to other platforms, where increasing the number of quantum systems per node frequently requires additional fabrication processes. Quantum gates can be realised using atom-atom interactions at the micrometre scale via highly-excited Rydberg states [83–85]. Optical cavities, on the other hand, can also enable for quantum gates: when multiple atoms are trapped within one cavity, the reflection of a single photon from that cavity can perform a gate between the atoms [86]. Further, improved vacuum conditions allowed trapping lifetimes of several minutes and non-destructive readouts have been realised [69, 87], and single-atom based quantum simulators now include up to 256 programmable atoms [88, 89]. All these achievements make neutral atoms a promising candidate to serve in quantum networks.

For the realization of long-distance fibre based quantum networks, it is indispensable to operate at low-loss telecom wavelengths. Most quantum memories, however, employ transitions in the ultra-violet, visible, or near-infrared wavelengths, hence experiencing high optical attenuation losses in optical fibres. For example, for rubidium atoms operating at 780 nm, the attenuation in fibres is around 4 dB/km, equalling an attenuation of a factor 10 for every 2.5 km fibre, as illustrated in Figure 1.2. This limits the reach of quantum channels to a few kilometres. In contrast, at the telecommunication wavelength of 1550 nm, the attenuation is reduced to around 0.2 dB/km, resulting in an attenuation by a factor 10 for every 50 km fibre and hence enabling for quantum channel lengths of hundreds of kilometres. To overcome this wavelength mismatch, quantum frequency conversion proves to be an effective tool [90–93]. The demands on the conversion devices, however, are high. Ideally, they should have a high conversion efficiency, induce no noise, and preserve the polarisation of the converted photons. Over the past decades, these properties were demonstrated individually, but only recently devices were constructed that simultaneously fulfil all the requirements [94, 95]. Enabled by these devices, two atomic ensembles were entangled over optical fibres with a length up to 50 km and the entanglement was analysed retrospectively [96]. Besides frequency conversion, there exist other approaches to interface quantum memories to telecom wavelengths. One is to generate a pair of entangled photons, of which one photon is at telecom wavelength and the other matches the transition of an absorptive quantum memory in which the photon state is stored. Recently, this method was employed to entangle two multimode solid-state quantum memories over 50 m of optical fibre [97].

In this work, we report on two main results: (i) the first proof-of-concept demonstration of device-independent quantum key distribution and (ii) the generation of heralded entanglement between two atomic quantum memories over tens of kilometres of optical fibre. For this, single rubidium atoms are optically trapped and manipulated in independent set-ups located in build-
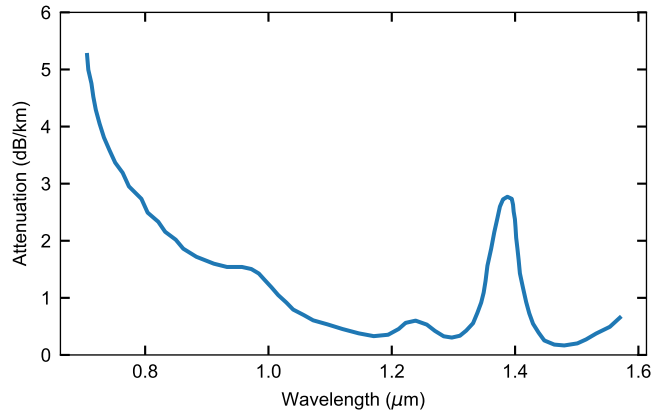
Figure 1.2: **Typical attenuation in an optical fibre for varying wavelength.**

ings 400 m apart. The distant atoms are entangled and analysed in an event-ready scheme: first, the spin state of the atom is entangled with the polarisation of a photon. Next, fibres guide the photons to a Bell-state measurement device where a projective measurement of the photons swaps the entanglement to the atoms. Implementation of a novel key distribution protocol shows that the experimental set-up allows for generation of a secure key in a fully device-independent setting. Furthermore, by employing polarisation-preserving quantum frequency conversion to the low loss telecom band, the reach of the quantum network link is extended to a fibre length of 33 km.

The results presented here relay on prior work conducted in our research group. In this light, it is informative to first reflect on the almost two decades of experimental research involving neutral single atoms using different generations of experimental set-ups—and detailed in numerous exquisite doctoral theses [98–107]. From the start on, the experiments were motivated by performing a loophole-free Bell test: a violation of a Bell inequality while at the same time closing both the detection and locality loopholes. This requires an experimental apparatus that can generate and analyse entanglement shared between two remote locations with a fidelity high enough to violate a Bell inequality, a near unit detection efficiency to close the detection loophole, and a fast state readout to allow for space-like separated measurement outcomes. The project was kick-started by the realization of a simple technique to store a single atom in an optical dipole trap [108]. Utilizing the collisional blockade effect, a single-atom was loaded in a dipole trap from a magneto-optical trap. Not much later, this system was employed to demonstrate entanglement between the spin state of a single atom and the polarisation state of a single photon [43], as well as for the remote state preparation of the atomic quantum memory [109]. To close the locality loophole in the Bell test a fast and high-fidelity state readout is crucial, which was realized by a state-selective ionization scheme and direct detection of the ion and electron using channel-electron multipliers [110]. Subsequently, preparations were made to implement the entanglement swapping protocol via two-photon interference [111] and the coherence time of the atomic state was optimized and characterized [112]. All this, resulted in the generation and analysis of heralded entanglement of two atoms separated by 20 m [55]. The last step involved increasing the distance between the traps to 400 m to allow for space-like separation of the state readout and hence closing the locality loophole. Finally, in 2015 and 2016, a significant violation of a Bell inequality was observed while closing both the detection and locality loopholes—thus

refuting the hypothesis of local realism [8].

Here we employ this event-ready entanglement generation set-up for a proof-of-concept demonstration of device-independent quantum key distribution. To realize the demanding requirements, both experimental and theoretical advancements were made. We describe experimental steps that improved the observed fidelity of the entangled atom-atom state from around 80% to 90%. This is mainly achieved by conditioning the Bell-state measurement on the arrival time of the two photons. Here, a thorough analysis and simulation of the atom-photon entanglement generation and entanglement swapping processes, introduced in [102] and expanded in [106], show time dependent effects that reduce the observed state fidelity. At the cost of event rate, those events are successfully removed. Additionally, the design and implementation of custom high-NA objectives, as detailed in [107], significantly increased the atomic fluorescence collection efficiency and hence the entanglement generation rate. On the theory side, a new protocol was developed by our collaborators at the National University of Singapore, involving two instead of one measurement settings to generate the key [113]. This increases the noise tolerance of the protocol and hence allows for key distribution in a device-independent setting with entangled states of lower quality. Our results show that state-of-the-art quantum network links are able to harness the full quantum advantage for secure communication.

Furthermore, we show an increase in reach of the quantum network link to tens of kilometres of fibre using quantum frequency conversion. The implementation of low noise, high efficiency, and polarisation-preserving conversion devices—designed and constructed by our collaborators of the University of Saarland—interface the atomic quantum memories to telecom wavelength for efficient entanglement distribution via optical fibres. Here we describe the implementation of the conversion devices in the single-atom trap set-ups and present results of atom-photon and atom-atom entanglement distribution over up to 33 km fibre. For the atom-atom entanglement generation, we analyse the atomic states only after receiving a herald that signals that the entanglement generation succeeded, including a time delay to simulate two-way communication between the nodes and the middle station. This heralding scheme allows to employ the generated entanglement as a ready-to-use resource in quantum networks for, e.g., device-independent quantum key distribution or quantum repeater protocols.

This thesis is structured as follows. Chapter 2 lays out the foundation of the experimental methods used to generate and analyse entanglement between two distant atoms. Therefore, we introduce the principles of entanglement distribution with single atoms, describe the methods to trap, control, entangle, and analyse single atoms, after which we exemplary detail on the fidelity estimation of the observed entangled states. Chapter 3 presents the first proof-of-concept demonstration of device-independent quantum key distribution. It begins with a general introduction to quantum key distribution, after which the device-independent scenario and requirements are described. Next, an overview of potential experimental platforms is given after which we report on our experimental implementation. Chapter 4 describes long-distance distribution of atom-photon entanglement at telecom wavelength. Starting with the derivation of the quantum frequency conversion process, it discusses the design criteria for the conversion devices and presents the realised set-up. Afterwards, we show results of observing atom-photon entanglement over fibre lengths up to 20 km, which are extrapolated to estimate the system's performance over up to 100 km fibre. Chapter 5 extends on this by reporting on a two-node set-up and demonstrating the generation and observation of atom-atom entanglement at telecom wavelength over long fibre links. It details on the experimental set-up and sequence, the achieved entanglement generation rate, and the observed atom-atom entanglement fidelities. Finally, Chapter 6 gives a general outlook and conclusion.

Chapter 2

Entangling Distant Atoms

This thesis reports on a proof-of-concept demonstration of device-independent quantum key distribution and entanglement generation between two quantum memories over city-to-city length fibre links. Fundamental in these experiments is the generation and analysis of entanglement between two remote single-atom quantum memories. For this, single rubidium atoms are stored, controlled, and analysed in two independent experimental set-ups located in buildings 400 m apart. In this chapter, we introduce the concepts and methods employed to entangle distant atoms, including the generation of atom-photon entanglement, generation of atom-atom entanglement via an entanglement swapping protocol, and the methods used to analyse the entangled states.

This chapter is organized as follows. Section 2.1 describes the concepts of atom-photon entanglement creation via spontaneous decay and atom-atom entanglement generation employing an entanglement swapping protocol. Next, Section 2.2 details the storage of a single rubidium atom in an optical dipole trap. In Section 2.3, we report on the generation and analysis of atom-photon entanglement, while Section 2.4 describes the methods to generate and analyse atom-atom entanglement. Finally, in Section 2.5, the decoherence effects of the atomic spin states are listed and modelled.

2.1 Principle of entanglement distribution using single atoms

Entanglement shared between distant particles opens up a wide range of innovative applications in the field of quantum science and technology. These applications include fundamental test of nature, secure communication, enhanced sensing, and distributed quantum computing. Quantum networks—a group of spatially separated quantum memories that share entanglement—are envisioned to facilitate the distribution of entanglement that is required for these applications. Photons are the natural choice to carry information over long distances, which can be guided from node to node via optical fibres. Various physical candidates exist to serve in quantum nodes for long-distance distribution of entanglement. They have to fulfil the following critical capabilities:

- Entanglement generation or transfer between light and matter.

- Efficient collection of photons.

- Memory coherence times much longer than the entanglement generation time.
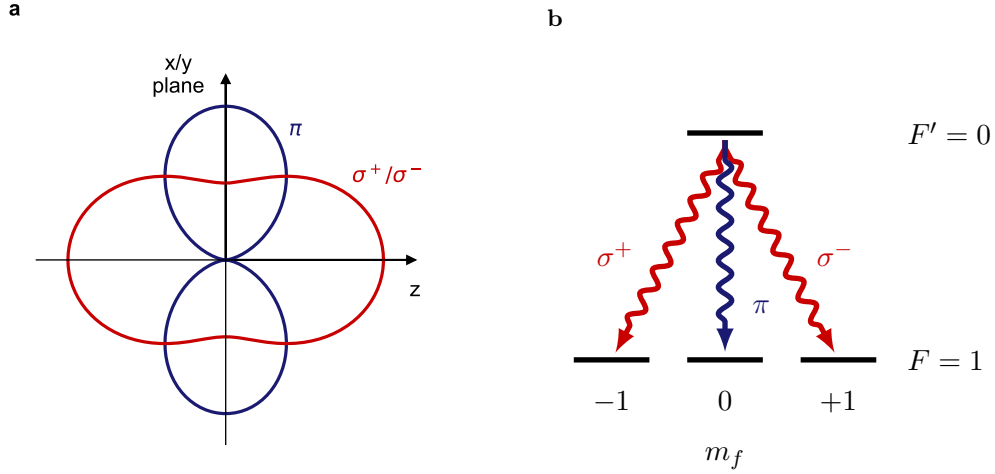
7

Figure 2.1: **Emission of an atom. a**, Dipole emission geometry of an atom for π-polarisation and $\sigma^{\pm}$-polarisation. **b**, Energy level scheme of atom-photon entanglement generation via spontaneous decay.

- High fidelity readout of the quantum memory.

In this work we present experiments with neutral single-atoms, for which all of these critical requirements have been demonstrated over the past decades.

Creation of atom-photon entanglement

Spontaneous emission of an atom generally leads to entanglement between the emitted photon and the atomic state after the decay[1]. Since the initial and final atomic states have well defined angular momentum, conservation of angular momentum defines the spin state of the emitted photon. For an atom in an excited state without angular momentum $F' = 0$ this leads to a decay to the ground state $F = 1$ via three possible decay channels: to $m_F = -1$ when emitting a σ^+-polarised photon, to $m_F = 0$ when emitting a π-polarised photon, or to $m_F = +1$ when emitting a σ^--polarised photon, as illustrated in Figure 2.1. In the case of equal probabilities of the three processes, i.e., similar Clebsch-Gordon coefficients, we can write the entangled atom-photon state as follows

$$|\Psi\rangle_{\mathsf{ap}} = \frac{1}{\sqrt{3}}(|1, -1\rangle|\sigma^+\rangle + |1, 0\rangle|\pi\rangle + |1, +1\rangle|\sigma^-\rangle), \tag{2.1}$$

where the atomic states are denoted as $|F, m_F\rangle$. For a photon analysed along the quantization (z-)axis detection of π-polarised photons is not possible, as shown in Figure 2.1a, resulting in the state

$$|\Psi\rangle_{\mathsf{ap}} = \frac{1}{\sqrt{2}}(|1, -1\rangle|\sigma^+\rangle + |1, +1\rangle|\sigma^-\rangle). \tag{2.2}$$

---

[1]Spontaneous emission is not the only method to generate atom-photon entanglement; another option would be stimulated emission into a cavity mode.

Atom-atom entanglement generation via entanglement swapping

Particles that never interacted can be entangled via the entanglement swapping protocol. For example, starting with two entangled atom-photon pairs, a joint measurement on the photons can swap the entanglement to the atoms. To illustrate this, we write Eq. (2.10) for an entangled atom-photon pair i as

$$|\Psi\rangle_i = \frac{1}{\sqrt{2}}(|\uparrow\rangle_{\mathsf{a}_i}|\downarrow\rangle_{\mathsf{p}_i} + |\downarrow\rangle_{\mathsf{a}_i}|\uparrow\rangle_{\mathsf{p}_i}), \tag{2.3}$$

where subscripts a and p denote the atom and photon state, respectively. The four particle state is now described by

$$\begin{aligned}
|\Psi\rangle =& |\Psi\rangle_1 \otimes |\Psi\rangle_2 \\
=& \frac{1}{\sqrt{2}}(|\uparrow\rangle_{\mathsf{a}_1}|\downarrow\rangle_{\mathsf{p}_1} + |\downarrow\rangle_{\mathsf{a}_1}|\uparrow\rangle_{\mathsf{p}_1}) \otimes \frac{1}{\sqrt{2}}(|\uparrow\rangle_{\mathsf{a}_2}|\downarrow\rangle_{\mathsf{p}_2} + |\downarrow\rangle_{\mathsf{a}_2}|\uparrow\rangle_{\mathsf{p}_2}) \\
=& \frac{1}{2}(|\uparrow\rangle_{\mathsf{a}_1}|\downarrow\rangle_{\mathsf{p}_1}|\uparrow\rangle_{\mathsf{a}_2}|\downarrow\rangle_{\mathsf{p}_2} + |\downarrow\rangle_{\mathsf{a}_1}|\uparrow\rangle_{\mathsf{p}_1}|\downarrow\rangle_{\mathsf{a}_2}|\uparrow\rangle_{\mathsf{p}_2}) \\
&+ \frac{1}{2}(|\uparrow\rangle_{\mathsf{a}_1}|\downarrow\rangle_{\mathsf{p}_1}|\downarrow\rangle_{\mathsf{a}_2}|\uparrow\rangle_{\mathsf{p}_2} + |\downarrow\rangle_{\mathsf{a}_1}|\uparrow\rangle_{\mathsf{p}_1}|\uparrow\rangle_{\mathsf{a}_2}|\downarrow\rangle_{\mathsf{p}_2}).
\end{aligned} \tag{2.4}$$

Rewriting this equation using the four maximally entangled Bell states $|\Phi^\pm\rangle = \frac{1}{2}(|\uparrow\rangle|\uparrow\rangle \pm |\downarrow\rangle|\downarrow\rangle)$ and $|\Psi^\pm\rangle = \frac{1}{2}(|\uparrow\rangle|\downarrow\rangle \pm |\downarrow\rangle|\uparrow\rangle)$ for the atom-atom and photon-photon states results in

$$\begin{aligned}
|\Psi\rangle =& |\Phi^+\rangle_{\mathsf{a}_1,\mathsf{a}_2} \otimes |\Phi^+\rangle_{\mathsf{p}_1,\mathsf{p}_2} \\
&+ |\Phi^-\rangle_{\mathsf{a}_1,\mathsf{a}_2} \otimes |\Phi^-\rangle_{\mathsf{p}_1,\mathsf{p}_2} \\
&+ |\Psi^+\rangle_{\mathsf{a}_1,\mathsf{a}_2} \otimes |\Psi^+\rangle_{\mathsf{p}_1,\mathsf{p}_2} \\
&+ |\Psi^-\rangle_{\mathsf{a}_1,\mathsf{a}_2} \otimes |\Psi^-\rangle_{\mathsf{p}_1,\mathsf{p}_2}.
\end{aligned} \tag{2.5}$$

Hence a projection of the two photons on one of the maximally entangled Bell states results in an entangled atom-atom state of the same type. Remarkably, this entangles particles that never interacted.

Quantum repeaters

The entanglement swapping protocol is not limited to photonic projections, but could also be applied to two pairs of entangled quantum memories. A projective Bell-state measurement on two atoms, each individually entangled with another atom, results in an entangled state between the two atoms that were not measured. This process forms the basis of a potential memory-based quantum repeater, allowing to overcome exponential channel losses during entanglement distribution. The demonstration of a quantum repeater protocol, however, is out of the scope of this thesis.
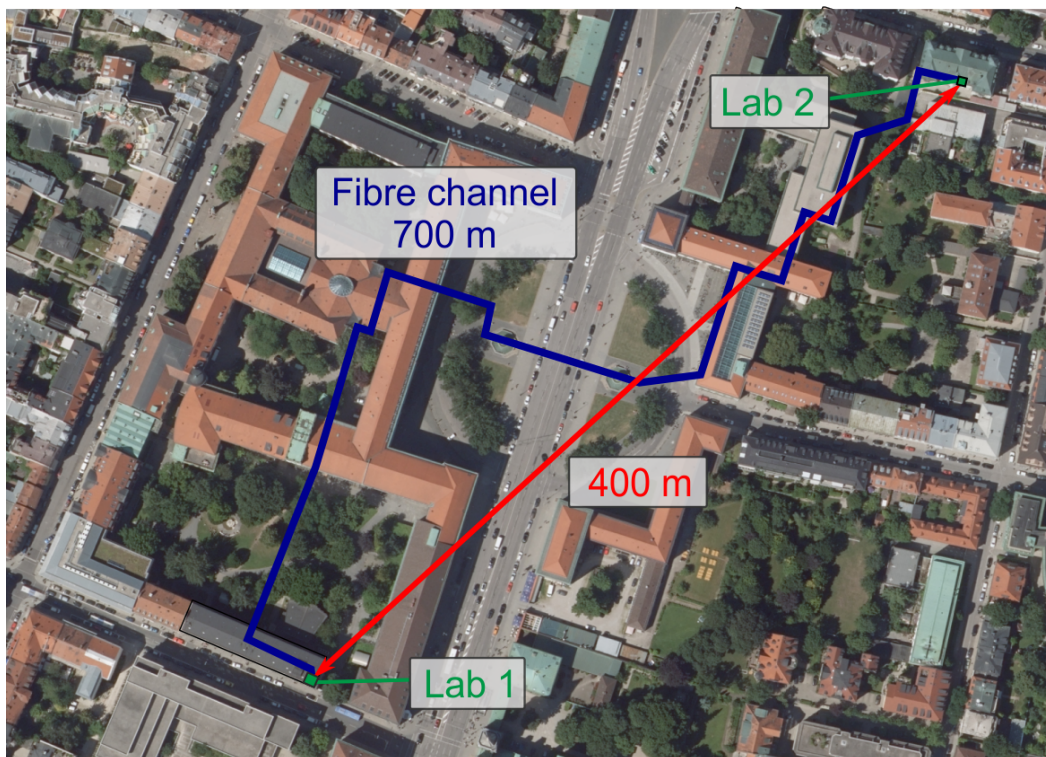
Figure 2.2: **Map of the LMU campus in downtown Munich.** The laboratories are located at opposite sides of the campus with a line-of-sight separation of approximately 400 m. A fibre channel with a length of 700 m connects the laboratories. Map data provided by: © Bayerische Vermessungsverwaltung.

2.2 Single atom trap set-ups

This work describes quantum information experiments using single-atoms trapped in set-ups located in two laboratories at opposite sides of the LMU campus in downtown Munich, as illustrated in Figure 2.2. More specifically, Lab 1 is based at the Faculty of Physics at the Schellingstraße 4 and Lab 2 at the Department of Economics at the Schackstraße 4. The labs are approximately 400 m apart and connect via a 700 m long fibre channel to exchange photons. In the independent set-ups, a single ^{87}Rb atom serves as quantum memory, which can be entangled with a single photon to then entangle the two quantum memories via entanglement swapping, as described before in Section 2.1. The single-atoms are optically trapped, laser cooled, and further isolated from the environment in an ultra-high vacuum set-up.

A ^{87}Rb quantum memory with light-matter interface

Rubidium—an alkaline metal—has a relatively simple energy level spectrum due to its single valence electron. The stable ground state of ^{87}Rb notated by $5^2\mathrm{S}_{1/2}$ and the first excited state notated by $5^2\mathrm{P}$ are relevant for this research, which both are split into various sub-states. In particular, fine splitting of the excited state results in two states, namely $5^2\mathrm{P}_{1/2}$ (D_1-line, 795 nm) and $5^2\mathrm{P}_{3/2}$ (D_2-line, 780 nm). Furthermore, due to the nuclear spin of $3/2$, the ground state is split into hyperfine states $F = \{1, 2\}$ and the excited states into $F' = \{1, 2\}$ and $F' = \{0, 1, 2, 3\}$, respectively. Finally, each hyperfine level is split into $m = 2F + 1$ Zeeman sub-

states. For a detailed overview of the relevant energy levels and physical properties of rubidium we refer to Appendix A.

Rubidium is selected in this research for various reasons. Namely, a qubit is conveniently encoded in the stable ground states $5^2\mathrm{S}_{1/2}\,|F=1, m_F=\pm1\rangle$, where a spontaneous decay from the state $5^2\mathrm{P}_{3/2}\,|F=0, m_F=0\rangle$ generates a maximally entangled state between these atomic qubit states and the polarisation of the emitted photon, as described before in Section 2.1. Furthermore, rubidium possesses a cycling transition $5^2\mathrm{S}_{1/2}\,|F=2\rangle \leftrightarrow 5^2\mathrm{P}_{3/2}\,|F'=3\rangle$, i.e., an excited state that decays to a specific ground state with a very high probability, which can be used for laser cooling of the atom, and lasers to drive the near infrared transitions are widely available.

Vacuum chamber and magneto-optical trap

The atoms are isolated from the environment by an ultra-high vacuum (UHV) set-up, which is built from CF (ConFlat) components of 316L and 316LN stainless steel to minimize magnetic permittivity. Pumping with an ion-getter pump (Varian, UHV-24p) achieves pressures on the order of 10^{-10} mbar and rubidium atoms are released in the vacuum set-up via dispensers. A glass cell provides optical access to the trapping position of the atom with a maximal numerical-aperture (NA) of 0.5. Furthermore, the glass cell contains space for charged particle detectors. A detailed description of the design and construction of the vacuum set-ups is found in [103] and some parts are described in [114].

The experimental sequence to trap a single-atom begins with laser cooling of a cloud of atoms in a magneto-optical trap (MOT) [115, 116]. A MOT relays on both magnetic and optical fields to slow down and localize neutral atoms. It consists of three pairs of circularly polarised counterpropagating beams that overlap in the zero-point of a quadrupole magnetic field generated by a pair of magnetic field coils in anti-Helmholtz configuration. In our set-ups, the light fields originate from a frequency stabilized external-cavity diode laser (Toptica, DL pro) which are red detuned by ∼18 MHz from the cycling transition. Realisation of a MOT for rubidium requires an additional repump laser resonant to the transition $5^2\mathrm{S}_{1/2}\,|F=1\rangle \leftrightarrow 5^2\mathrm{P}_{3/2}\,|F'=2\rangle$, which pumps atoms back into the cycling transition in rare occasion they decay to the state $5^2\mathrm{S}_{1/2}\,|F=1\rangle$.

The configuration generates a cloud of around 10^4 atoms within a radius of 1 mm. The atoms are cooled well below the Doppler limit by polarisation gradient cooling—cold enough to be stored in the shallow potential of an optical dipole trap.

Optical dipole trap

To control and manipulate an individual atom, a single-atom from the MOT is loaded into an optical dipole trap (ODT) [117]. The dipole potential is induced by the AC-stark effect and scales as I/Δ for a given intensity I and frequency detuning Δ. Hence, simply focussing a red detuned beam generates a 3 dimensional trapping potential, as visualised in Figure 2.3. Importantly, since the scattering rate scales with I/Δ^2, an intense ODT beam that is far detuned from the D_1- and D_2-line of rubidium allows for the generation of a trapping potential while at the same time achieving low scattering rates, i.e., minimizing influence of the trapping beam on the internal atomic state. Moreover, when the beam waist is small enough ($< 7\ \mu$m), the collisional blockade effect prohibits loading of more than one atom [75]. For a thorough analysis of the single-atom trapping techniques we refer to [98, 108].

Assuming a linearly polarised light field of the trapping beam, the induced potential is given by

$$U(r, z) = \frac{\pi c^2 \Gamma}{2\omega_0^3} \left(\frac{2}{\Delta_{2,F}} + \frac{1}{\Delta_{1,F}} \right) I(r, z), \tag{2.6}$$

with Γ denoting the spontaneous decay rate of the excited states, ω_0 representing the center transition frequency of the D-line, and the detuning with respect to the D_1- and D_2-line given by $\Delta_{1,F}$ and $\Delta_{2,F}$, respectively. The beam intensity $I(r, z)$ is position dependent and, assuming a Gaussian spatial mode, described as

$$I(r, z) = I_0 \left(\frac{w_0}{w(z)} \right)^2 e^{-\frac{2r^2}{w(z)^2}}, \tag{2.7}$$

where I_0 and w_0 denote the intensity and beam waist at the focus point, respectively, and the beam waist at position z equals

$$w(z) = w_0 \sqrt{1 + \frac{z}{z_R}^2}, \tag{2.8}$$

where the Rayleigh length is given by $z_R = \pi w_0^2 / \lambda$ for a wavelength of λ. We can approximate the potential as harmonic, which results in radial (w_r) and transversal (w_z) trap frequencies given by

$$w_r = \sqrt{\frac{4U_0}{mw_0^2}} \quad \text{and} \quad w_z = \sqrt{\frac{2U_0}{mz_R^2}}, \tag{2.9}$$

where $U_0 = U(0, 0)$ equals the potential depth at the focus point of the trapping beam and m denotes the mass of a ^{87}Rb atom.

In our set-ups, the dipole trap light originates from a free-running, single-mode diode laser at ~ 850 nm, which is amplified by a tapered amplifier (Toptica, TA pro) to a few hundred milliwatts. Moreover, insertion of a single-mode fibre to the beam path guarantees a spatial Gaussian mode. The beam focus coincides with the MOT position and has a waist of $w_0 = 2.05$ μm, resulting in a Rayleigh length of $z_R = 13.6$ μm. Typical initial beam powers of 50 mW result in a potential depths of $U_0 = k_B \times 2.32$ mK and trap frequencies of $w_r = 2\pi \times 73$ kHz and $w_z = 2\pi \times 6.8$ kHz.

Photon collection

Observation of fluorescence from a single-atom forms the basis of the key experimental methods employed, including the single-atom trapping, entanglement distribution, and atomic state readout. Therefore, an objective with a numerical-aperture (NA) of 0.5 (PhotonGear, custom design) collects fluorescence from single-atoms trapped in the ODT. The objective is placed outside of the vacuum set-up and has a working distance of 14 mm. Besides fluorescence collection, the objective is also employed to focus the ODT beam, where a dichroic mirror splits the two beam paths, as illustrated in Figure 2.4. In this configuration, the simplicity and sharing of a large part of the light paths increases the stability of the set-up. The collection axis defines the quantization axis of the system. During the timespan of this thesis, the fluorescence collection efficiency was improved by a factor of 2.5 and 3.5 for Trap 1 and 2, respectively, by implementation of custom designed objectives, which is detailed in [107] and some parts in [118, 119].
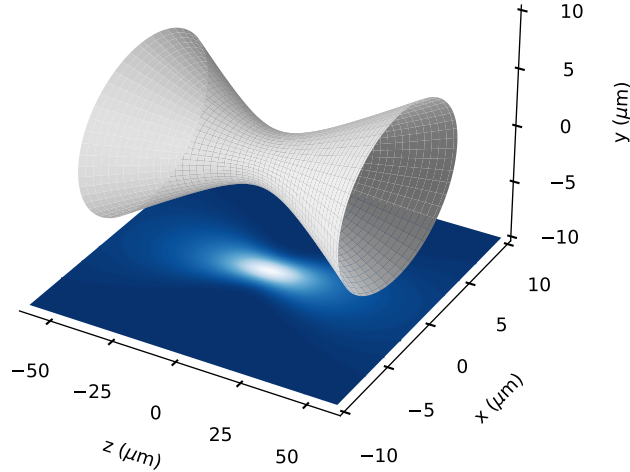
Figure 2.3: **Geometry of the dipole trap beam and generated potential.** The generated potential is proportional to the intensity of the beam $U \propto I(r, z)$, with $r = \sqrt{x^2 + y^2}$. The blue-white colormap visualises the trapping potential in the x, z-plane for $y = 0$.
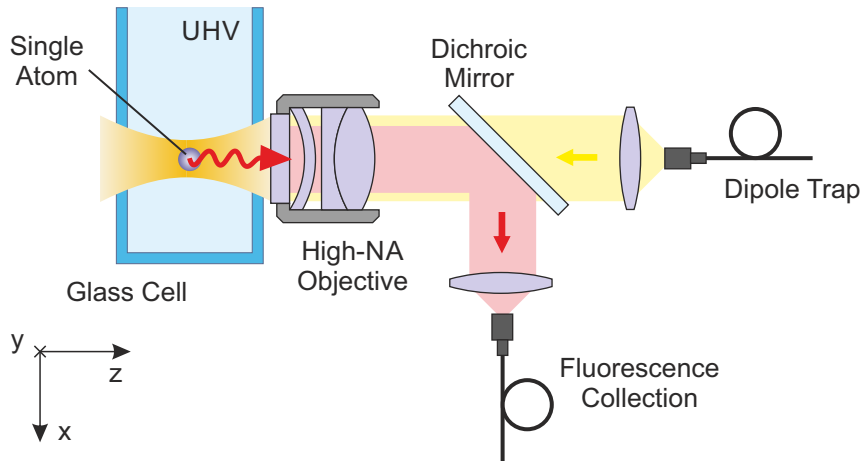
Figure 2.4: **Schematic of the single-atom trap set-up.** A single ^{87}Rb atom is stored in a tightly focussed optical dipole trap at 850 nm. The dipole trap beam is focussed to approximately 2 μm using a high numerical-aperture (NA) objective within an ultra-high vacuum (UHV). The same objective collects the atomic fluorescence at 780 nm wavelength, which is separated from the dipole trap light with a dichroic mirror and coupled into a single-mode fibre. For a detail description of the design criteria, alignment, and characterization of the single-atom trap and fluorescence collection set-up see [107].

Magnetic field control

As mentioned before, the qubit is encoded in the Zeeman sub-states of the atom, which are energy sensitive to magnetic fields. Various sources in- and outside the laboratory induce magnetic fields that can introduce decoherence or uncontrolled precession of the atomic state. In particular, the Munich U-Bahn, passing by at around 60 and 120 m from the labs, produce fields of tens of mG which change on a second timescale; power lines and supplies in the lab introduce field noise at a frequency of 50 Hz; and the earth magnetic field introduces a nearly static field of approximately 500 mG. Hence, control and active stabilization of the magnetic fields is required to prolong the coherence time of the trapped single-atoms.

For this, three pairs of Helmholtz coils, orientated along the x-, y-, and z-axis, control the magnetic field. The coils are centred around the atom position and have dimensions of $170 \times 170 \times 170$ mm. The magnetic field is actively stabilized using a feedback loop with 200 Hz bandwidth. Therefore, a magnetic field sensor (Honeywell, HMC1053) provides the input for stabilization, which is located outside of the vacuum at approximately 2 cm from the atom position. In this configuration, the magnetic fields at the atom position are controlled to better than $\sigma = 0.5$ mG.

Trapping sequence

The sequence to trap a single-atom begins by switching on the cooling and repump beams together with the quadrupole coils to generate a cloud of cold rubidium atoms in a MOT. At the same time, the ODT is switched on and the current through the Helmholtz coils are set such that the position of the atom cloud overlaps with the ODT focus. Probabilistically, an atom from the cloud of atoms is loaded in the dipole trap. Loading of an atom is observed by a sudden increase in registered fluorescence counts detected by single photon detectors (Laser Components, Count-10), which are located behind the fluorescence collection fibre (see Figure 2.4). When the number of counts exceeds a certain threshold, the experimental control switches off the quadrupole coils, resets the magnetic field sensor, and activates the active stabilization of the magnetic fields. Then the experiments can start. The moment an atom is lost from the trap—observed by a sudden drop of detected fluorescence counts—the loading sequence automatically restarts. Figure 2.5a shows a typical fluorescence collection trace during operation. The trace clearly shows two count levels, at 10 and 80 counts per integration time of 40 ms, indicating the trapping of zero or one atom, respectively. The average trapping duration of an atom in the presence of MOT-light is typically around 4 s, as shown in Figure 2.5b.

2.3   Atom-photon entanglement

The storage, control, and fluorescence collection of an individual atom enables for quantum information and quantum communication applications. Here, the long-lived atomic ground states act as quantum memory and spontaneous decay to these states is used as source of entanglement between the spin state of the atom and polarisation state of the emitted photon [43, 99]. In this section, we describe the methods to generate and observe the entangled atom-photon state.
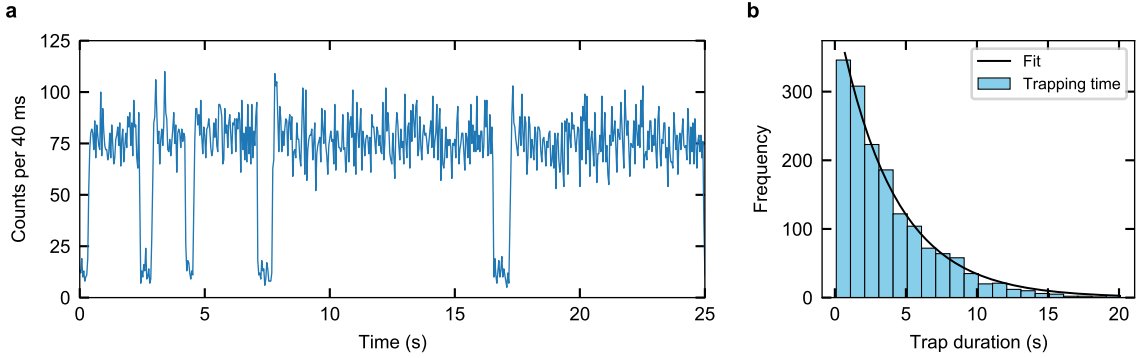
Figure 2.5: **Fluorescence trace and trapping duration histogram. a,** Fluorescence light detection of the atom over time in Trap 1. Two count levels are visible, at approximately 10 and 80 counts per 40 ms, indicating the trapping of zero or one atom, respectively. **b,** A histogram of the trapping duration having a exponential time constant of 4 s.

2.3.1 Generating atom-photon entanglement

Initial state preparation

The entanglement generation process starts by preparing the atom in the $5^2\mathrm{S}_{1/2}\,|F=1, m_F=0\rangle$ state via optical pumping. In this process, the atom is continuously excited with light that is resonant to all long-lived states, i.e., ground-states, except the target state, as illustrated in Figure 2.6. To maximize the probability to decay to the $F=1$ manifold, the atom is excited via transitions at the D_2-line (780 nm) due to the favourable hyperfine transition strength factors. Two groups of light fields are implemented, labelled pump$_{1\rightarrow2}$ and pump$_{1\rightarrow1}$, being resonant with the transitions $5^2\mathrm{S}_{1/2}|F=1\rangle \rightarrow 5^2\mathrm{P}_{3/2}|F'=2\rangle$ and $5^2\mathrm{S}_{1/2}|F=1\rangle \rightarrow 5^2\mathrm{P}_{3/2}|F'=1\rangle$, respectively. Pump$_{1\rightarrow2}$ alternates between left and right circular polarisations to address all Zeeman-states of the $F=2$ ground level. Pump$_{1\rightarrow1}$ is π-polarised which makes the state $5^2\mathrm{S}_{1/2}\,|F=1, m_F=0\rangle$ dark due to the selection rules.

The efficiency of the initial state preparation scheme is approximately 80%. The imperfection is a trade-off with the duration of the optical pumping scheme of 3 μs. To optimize the entanglement generation rate, the initial state preparation duration should be minimized. Note that imperfect state preparation does not drastically influence the atom-photon entanglement quality. The implementation and optimization of the presented state preparation scheme is discussed in detail in [104].

Creating entanglement between an atom and a photon

After the initial state preparation, the atom-photon entanglement is generated during a spontaneous decay of the atom, as detailed in Section 2.1. For this, a π-polarised laser pulse excites the atom to the state $5^2\mathrm{P}_{3/2}\,|F=0, m_F=0\rangle$, as illustrated in Figure 2.7. The excited state has a lifetime of 26.24 ns and spontaneously decays to the states in the $F=1$ manifold. In the decay, the polarisation of the photon that is emitted becomes entangled with the atomic Zeeman state due to conservation of angular momentum. For photon collection along the quantization axis, π-polarised photons are not coupled into the single mode fluorescence collection fibre and hence are filtered out, resulting in the following maximally entangled atom-photon state
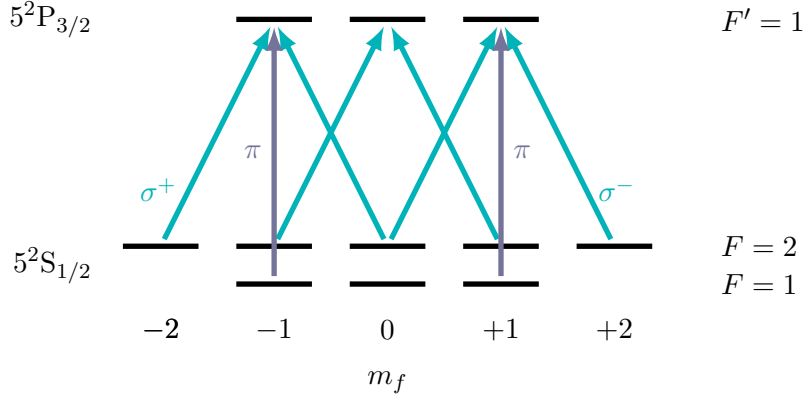
Figure 2.6: **Initial state preparation scheme.**   The atom is prepared in the state $5^2\mathrm{S}_{1/2}\,|F=1, m_F=0\rangle$ via optical pumping. Light fields with alternating σ^-- and σ^+- polarisation (lightblue arrows) pump empty the ground-states $|F=2\rangle$.   The states $5^2\mathrm{S}_{1/2}\,|F=1, m_F=\pm1\rangle$ are emptied with π-polarised light (purple arrows), for which the target state is dark due to the dipole selection rules.

$$|\Psi\rangle_{\mathsf{ap}} = \frac{1}{\sqrt{2}}|\downarrow\rangle_z|L\rangle + |\uparrow\rangle_z|R\rangle, \qquad\qquad (2.10)$$

where $|\downarrow\rangle_z$ and $|\uparrow\rangle_z$ denote atomic spin states $|F=1, m_F=-1\rangle$ and $|F=1, m_F=+1\rangle$, and $|L\rangle$ and $|R\rangle$ denote left- and right-circular photonic polarisation states, respectively. For a complete definition of the coordinate system, photon polarisation, and atomic states we refer to Appendix B. Moreover, during the entanglement generation process the ODT is switched off to revoke introduced light-shift effects on the emitted photons.

Various experimental imperfections in the pumping and excitation processes limit the fidelity of the generated atom-photon state. In particular, by off-resonant excitations to higher excited states due to the finite spectral pulse width or the emission of two photons during a single excitation pulse [102, 106], as illustrated in Figure 2.8. The parameters of the excitation pulse are optimized to suppress these unwanted effects. The temporal pulse shape is chosen Gaussian with a duration of 22 ns FWHM, which is a trade-off between reducing off-resonant excitations with longer pulse lengths and reducing two photon emissions with shorter pulse lengths. Furthermore, the pulse intensity is lowered to 80% of the maximal photon detection efficiency to diminish off-resonant excitations and two photon emissions, while only slightly reducing the entanglement generation rate.

2.3.2   Observation of atom-photon entanglement

To characterize the generated atom-photon entanglement, both the photonic polarisation state and atomic spin state are analysed.

Photonic state analysis

The photons emitted by the trapped atoms are coupled into a single-mode fibre to guide them to a polarisation analysis set-up located next to the trap set-ups. Polarisation drifts in the fibres
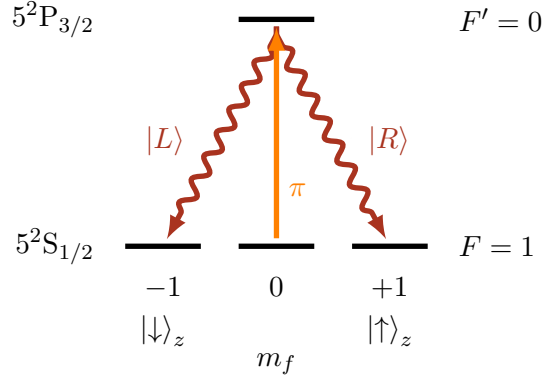
Figure 2.7: **Atom-photon entanglement generation scheme.** An atom is excited to the state $5^2P_{3/2}|F' = 0\rangle$ with a π-polarised laser pulse with a wavelength of 780 nm (orange arrow). In the subsequent spontaneous decay, the polarisation of the emitted photon (red wiggly arrows) becomes entangled with Zeeman state of the atom.

are compensated for using alignment light at the single photon frequency and fibre polarisation controllers. The measurement basis of the analysis set-up is set by half- and quarter-waveplates, after which the photons impinge on a polarising beamsplitter with a single photon detector in each output port to complete the state analysis.

Avalanche photon detectors (APD) detect the single-photons and detection events are accepted within a 208 ns long window. Typical probabilities of detecting a photon after an entanglement generation attempt equal $\eta_{\mathsf{ap}_1} = 5.4 \times 10^{-3}$ ($\eta_{\mathsf{ap}_2} = 6.9 \times 10^{-3}$) for Trap 1 (Trap 2) [107]. Assuming single-photon detector efficiencies of 55% (65%), this results in an estimate on the probabilities to couple a photon into the single-mode fibre after an excitation attempt of 1.0% (1.1%). Note that all efficiencies above include the initial state preparation efficiency of 80% and the excitation success probability set to 80% of its maximum value.

Atomic state analysis

The atomic spin state is analysed using a state-selective ionisation scheme, as illustrated in Figure 2.9. The scheme starts by transferring a certain atomic qubit superposition state from the ground state $5^2S_{1/2} |F = 1\rangle$ to the excited state $5^2P_{1/2} |F' = 1\rangle$ with a 140 ns long laser pulse at 795 nm (named "readout"). Simultaneously, the excited state is ionised using a bright pulse at 473 nm. If the atom decays to the state $5^2S_{1/2} |F = 2\rangle$ before ionisation, as indicated with gray arrows in Figure 2.9, a 780 nm pulse will transfer it to the state $5^2P_{3/2} |F' = 3\rangle$, which is ionised as well. The state readout is completed by either checking the presence of the atom using fluorescence collection since ionised atoms are lost from the trap or by direct and fast detection ($< 1\mu$s) of the ionisation fragments with channel-electron multipliers (CEM).

The measurement setting is controlled by the polarisation of the readout pulse, which is defined as

$$\chi = \cos(\gamma)V + e^{-i\phi}\sin(\gamma)H, \tag{2.11}$$

where V and H denote vertical and horizontal linear light polarisations, respectively, and we define $\gamma = \alpha$ for Trap 1 and $\gamma = \beta$ for Trap 2. Accordingly, two orthogonal atomic qubit state
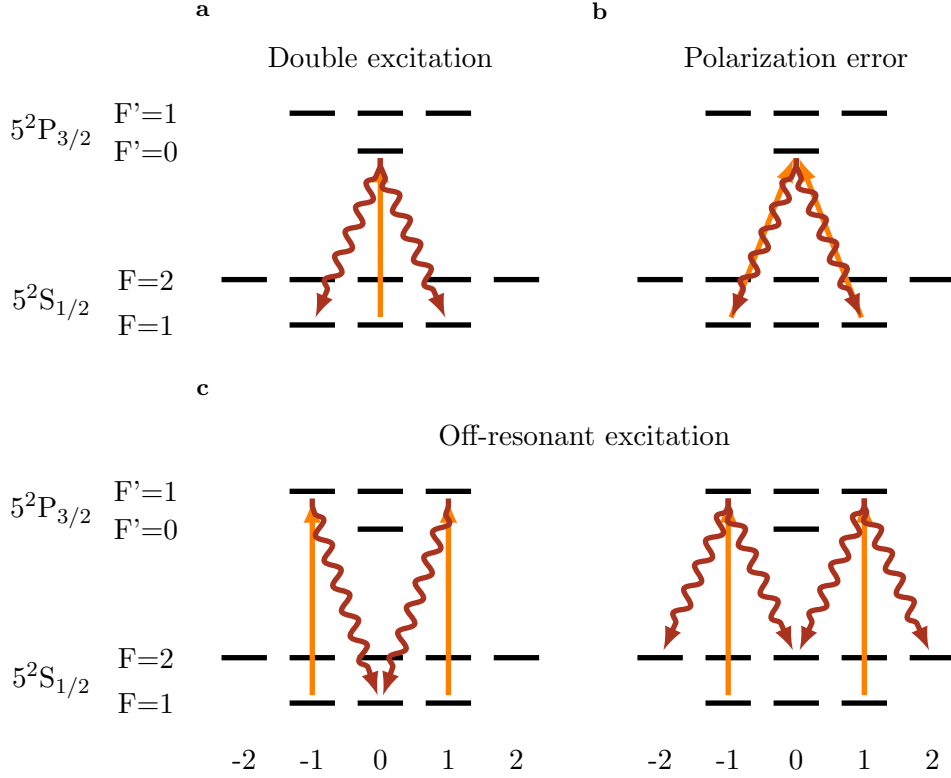
Figure 2.8: **Errors in the excitation process.** Shown are three frequently occurring excitation errors: double excitations, polarisation errors, and off-resonant excitations, conditioned on photon detection, i.e., for circular polarised decay channels (red arrows). **a**, Double excitation events with a first decay from the state $5^2\mathrm{P}_{3/2}|F' = 0, m_F = 0\rangle$ back to the initial state $5^2\mathrm{S}_{1/2}|F = 1, m_F = 0\rangle$ (not shown), and a second excitation and decay as intended generates the targeted entangled atom-photon state (shown), however, with a delayed temporal photon-shape compared to single excitation events. For the chosen excitation pulse parameters, this process occurs in approximately 4% of the single-photon detection events and substantially lowers the two-photon interference contrast. **b**, Polarisation errors in combination with wrong state preparation results in the targeted atom-photon state. **c**, Off-resonant excitation transfers the atom population to the state $5^2S_{1/2}|F = 2\rangle$ after an unsuccessful state preparation. The occurrence probability of this process depends on the excitation pulse intensity and can be estimated from the $F = 2$ population after an excitation attempt [102].

Figure 2.9: **Atomic readout scheme.** A superposition of the atomic qubit state—selected by polarisation of the readout light (red arrows)—is excited to the state $5^2P_{1/2}|F' = 1, m_{F'} = 0\rangle$ and subsequently ionised with a 473 nm laser pulse (blue arrows). If the atom decays to the state $5^2S_{1/2}|F = 2\rangle$ before it is ionised (gray arrows), a 780 nm laser pulse (green arrow) will transfer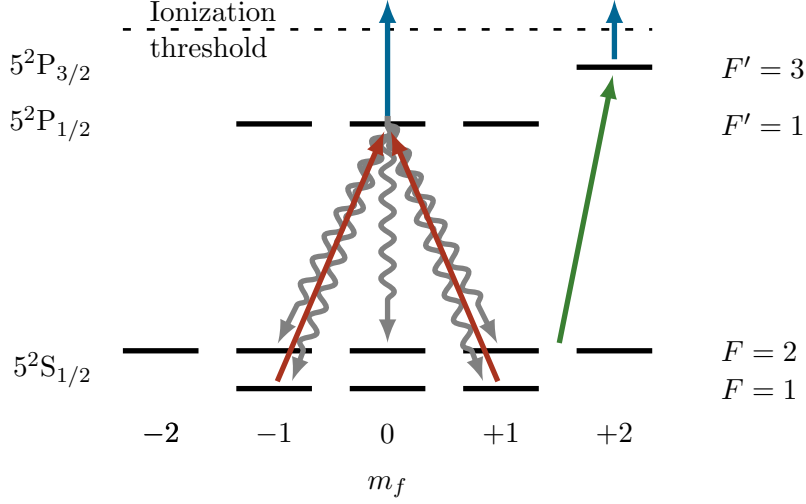 it to the state $5^2P_{3/2}|F' = 3\rangle$, which is ionised as well. Note that atom population in the state $5^2S_{1/2}|F = 1, m_F = 0\rangle$ is ionised for all readout light polarisations.

superpositions can be derived of which one is transferred to the excited state by the readout pulse (bright-state) and the other is not (dark-state), given as

$$|\Psi\rangle_{\text{bright−state}} = \cos(\gamma)\frac{1}{\sqrt{2}}(|\downarrow\rangle_z - |\uparrow\rangle_z) + \sin(\gamma)e^{-i\phi}\frac{i}{\sqrt{2}}(|\downarrow\rangle_z + |\uparrow\rangle_z) \quad \text{and}$$

$$|\Psi\rangle_{\text{dark−state}} = \sin(\gamma)\frac{1}{\sqrt{2}}(|\downarrow\rangle_z - |\uparrow\rangle_z) - \cos(\gamma)e^{-i\phi}\frac{i}{\sqrt{2}}(|\downarrow\rangle_z + |\uparrow\rangle_z).$$

(2.12)

Note that all states except the dark state are excited and hence ionised, and, notably, population in $5^2S_{1/2}|F = 1, m_F = 0\rangle$ is always ionised. This makes the readout scheme a projection measurement onto the dark-state. An intuitive example of the state selectivity is the case of a σ^+-polarised readout pulse. In the Z-basis, as shown in Figure 2.9, this pulse will excite an atom in the state $|\downarrow\rangle_z$ to the state $5^2P_{1/2}|F = 1, m_F = 0\rangle$, however, an atom in the state $|\uparrow\rangle_z$ will not be excited because of the absence of the state $5^2P_{1/2}|F = 1, m_F = 2\rangle$.

   The fidelity of the atomic state preparation and readout cycle equals 97%—by using the fast and direct CEM detection, three main loss mechanisms in this process were further analysed, as detailed in [103]. The first loss mechanism is the occurrence of resonant excitation and subsequent ionisation of the dark state, which reduces the contrast by 1.3%. The origin of this error is a false state preparation of the initial entangled atom-photon state. Secondly, off-resonant excitation of the dark state to the state $5^2P_{1/2}|F' = 2\rangle$ and subsequent ionisation contributes for 2.6%. The third effect inducing losses is unsuccessful ionisation of the bright state due to a fast decay to the dark state before the atom was ionised (gray arrows to states F=1 in Figure 2.9), which reduces the contrast by 2.0%.

   Currently, the atomic state readout is optimized for speed (readout in 820 ns) and hence a trade-off is made with the achieved fidelity. The events that cause loss in contrast due to false
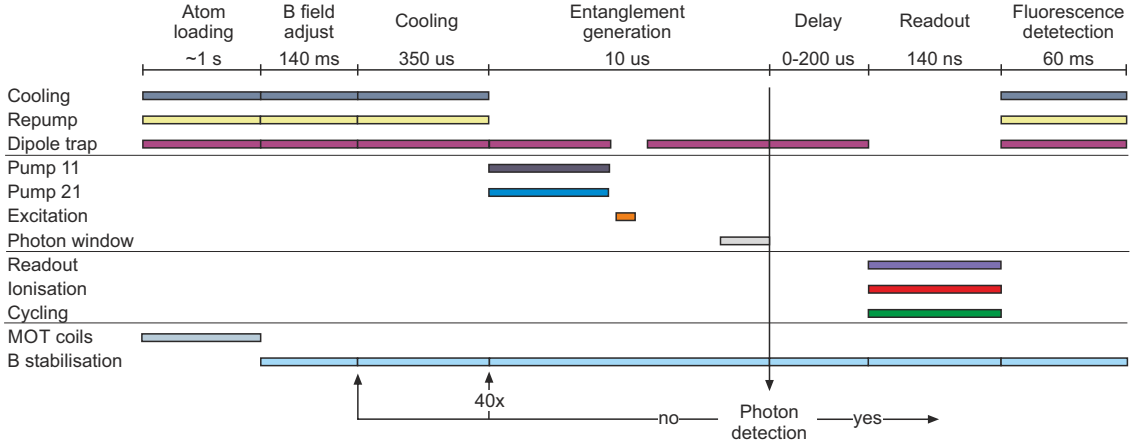
Figure 2.10: **Experimental sequence to generate and observe atom-photon entanglement.** A single-atom is loaded by simultaneously switching on the MOT—including the cooling and repump beams together with the quadrupole field coils—and the dipole trap beam. The entanglement generation tries, involving optical pumping and excitation, are applied in burst of 40, after which the atom is cooled for 350 μs. The tries are repeated until either a photon is detected and the atomic state is read out, or the atom is lost from the trap. The atom presence is continuously monitored by integration of the fluorescence counts during the cooling and pumping periods. The magnetic field (B) is stabilised during the complete entanglement generation and analysis process. The sequence is representative for both nodes, where the duration of the entanglement generation tries varies depending on the optical fibre length between the trap and polarisation analysis set-up.

entangled state preparation can be filter out based on the photon detection time, as will be discussed in Section 2.4.3, yet, at the cost of event rate. Further improvements in fidelity might be possible by a perfect STIRAP together with optimal control of the readout light [120].

Entanglement generation sequence

The experimental sequence to generate and analyse atom-photon entanglement is detailed in Figure 2.10. It starts by loading a single ^{87}Rb atom in the optical dipole trap by testing whether the number of fluorescence counts detected by the APD exceeds a certain threshold—loading of an atom typically takes < 1 s. Thereafter, the entanglement generation tries start, for which the atom is prepared in the initial state $5^2S_{1/2} |F = 1, m_F = 0\rangle$ via optical pumping (3 μs) and excited to the state $5^2P_{3/2} |F' = 0, m_{F'} = 0\rangle$ with a short laser pulse (22 ns FWHM). In the subsequent spontaneous decay, the atomic spin state becomes entangled with the polarisation state of the photon emitted along the quantization (z-) axis, resulting in the maximally entangled atom-photon state given in Eq. (2.10). The entanglement generation cycles are repeated until a single photon is detected at the polarisation analyser, whereby the atom is cooled for 350 μs after each 40 excitations in order to minimize the thermal motion in the trap [104]. After a successful photon detection, the atomic state is measured.
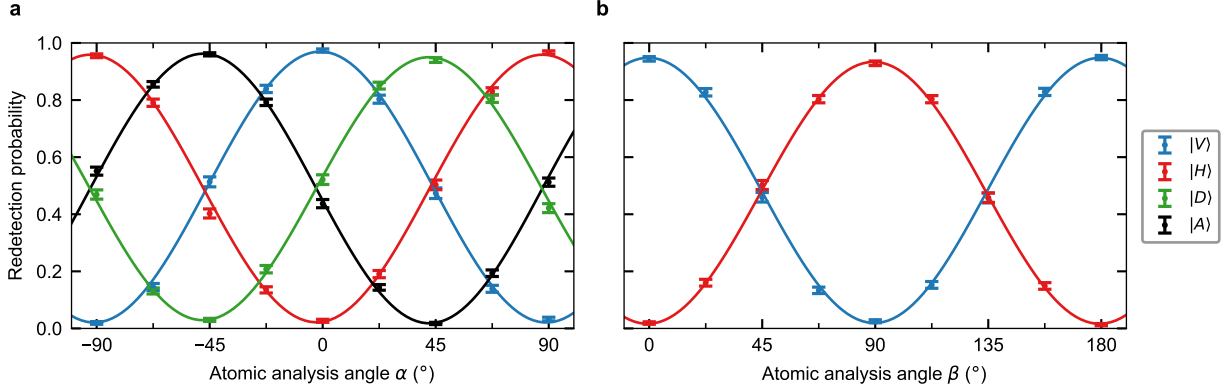
Figure 2.11: **Observation of atom-photon entanglement in both nodes.** Atom-photon state correlations for Trap 1 (**a**) and Trap 2 (**b**). The atomic spin state is analysed 25.6 μs (16.7 μs) after the entanglement generation process in Trap 1 (2). This time allows for an even number of oscillations of the Larmor precession due to the magnetic bias field of 57 mG (168 mG) along the y-axis and rephasing of the atomic state by matching the transverse trap frequencies. In total, we observed $N = 35259$ and 20001 entanglement generation events and the observed atom-photon state fidelity is estimated at $\mathcal{F}_{\text{ap}} \geq 0.952(7)$ and 0.941(7), for Trap 1 and 2, respectively.

Atom-photon state correlations and fidelity

We analyse the atom-photon entanglement by projecting the photonic polarisation in the H/V (horizontal/vertical) and D/A (diagonal/anti-diagonal) basis, while varying the atomic analysis angle, i.e., readout polarisation α (β) in Trap 1 (2), as shown in Figure 2.11. The visibilities (V) of the measured states are obtained by fitting the data with sinusoidal functions. For Trap 1, this results in visibilities of 0.942(14), 0.930(17), 0.942(13), and 0.954(19), for vertical $|V\rangle$, horizontal $|H\rangle$, diagonal $|D\rangle$, and anti-diagonal $|A\rangle$ photonic linear polarisation states, respectively. For Trap 2, the fits give visibilities of 0.943(16) and 0.917(8), for $|V\rangle$ and $|H\rangle$ photonic linear polarisation states, respectively.

To estimate a fidelity of the entangled atom-photon state, one needs to consider that the quantum memory is encoded in two magnetic sub-levels of the rubidium ground state $5^2S_{1/2}|F = 1\rangle$, which, however, is a spin-1 system. Besides the qubit states $|m_F = \pm 1\rangle$, also the state $|m_F = 0\rangle$ can be populated, due to, for example, magnetic fields in a direction not coinciding with the quantization axis. Hence, assuming depolarising noise in this 3×2 state space, the density matrix of the atom-photon state is given by

$$\hat{\rho} = \overline{V} |\Phi_{\text{ap}}\rangle \langle\Phi_{\text{ap}}| + \frac{1}{6}(1 - \overline{V})\hat{1}, \tag{2.13}$$

where $\overline{V}$ equals the average visibility of three orthogonal measurement bases. Hence, a lower bound on the fidelity relative to a maximally entangled state is given by

$$\mathcal{F}_{\text{ap}} \geq \langle\Phi_{\text{ap}}| \hat{\rho} |\Phi_{\text{ap}}\rangle = 1/6 + 5/6\overline{V}. \tag{2.14}$$

When assuming that the visibility of the not measured bases are equal to the measured basis with the lowest visibility, this results in estimated fidelities of $\mathcal{F}_{\text{ap}} \geq 0.952(7)$ and 0.941(7), for

Trap 1 and 2, respectively. Estimating the fidelity with the more common expression for two entangled qubits of $\mathcal{F} = 1/4 + 3/4\overline{V}$ would result in a higher fidelity and overestimates the fidelity of the generated state.

2.4 Heralded atom-atom entanglement

Starting with two entangled atom-photon pairs, a Bell-state measurement on the two photons can swap the entanglement to the atoms, as detailed in Section 2.1, and, at the same time, also heralds that entanglement is available between the two atoms. In this section, we describe the experimental implementation of the entanglement swapping protocol based on two-photon interference and discuss various effects that influence the fidelity of this process, as well as the methods used to evaluate the entangled atom-atom state quality.

2.4.1 Entanglement swapping

An interferometric Bell-state measurement of the two photons swaps the entanglement to the atoms. The quality of the two-photon interference—and hence the entanglement swapping—depends on the indistinguishability of the photons, in particular, in their spectral, spatial, and temporal degree of freedom [111].

Bell-state measurement via two-photon interference

Two-photon interference on a beamsplitter could be employed to perform a photonic Bell-state measurement—where the Hong-Ou-Mandel effect describes the interference process [121]. Here, we use a quantum mechanical description of a beamsplitter with two input and two output ports for totally mixed polarisation states [102, 106]. For this, we introduce the input creation and annihilation operators $\hat{a}_{i,P}^{\dagger}$ and $\hat{a}_{i,P}$, respectively, for port number $i \in \{1, 2\}$ and polarisation P, as well as, correspondingly, the output port operators $\hat{b}_{i,P}^{\dagger}$ and $\hat{b}_{i,P}$. The input output relations of the beamsplitter are now given by

$$\begin{bmatrix} \hat{b}_{1,P}^{\dagger} \\ \hat{b}_{2,P}^{\dagger} \end{bmatrix} = \hat{B}_P \begin{bmatrix} \hat{a}_{1,P}^{\dagger} \\ \hat{a}_{2,P}^{\dagger} \end{bmatrix} \qquad \leftrightarrow \qquad \begin{bmatrix} \hat{a}_{1,P}^{\dagger} \\ \hat{a}_{2,P}^{\dagger} \end{bmatrix} = \hat{B}_P^{-1} \begin{bmatrix} \hat{b}_{1,P}^{\dagger} \\ \hat{b}_{2,P}^{\dagger} \end{bmatrix}, \qquad (2.15)$$

whereby the general beamsplitter transformation matrix is given by

$$\hat{B}_P = e^{i\phi_0} \begin{bmatrix} \cos(\theta_P)e^{i\phi_\tau} & \sin(\theta_P)e^{i\phi_\rho} \\ -\sin(\theta_P)e^{-i\phi_\rho} & \cos(\theta_P)e^{-i\phi_\tau} \end{bmatrix}, \qquad (2.16)$$

with ϕ_0 denoting a general phase shift, which can be set to zero without loss of generality, ϕ_τ (ϕ_ρ) represent a phase shift for the transmitted (reflected) mode, and the angle θ_P defines the polarisation dependent splitting ratio.

Next is to insert a joint input state of two photons with totally mixed polarisations, which will be expressed in the H/V basis. For this, we use the Fock state notation, where $|n_1, n_2\rangle$ denotes the quantity and polarisation of the photons for port 1 (n_1) and port 2 (n_2). For example, when a H polarised photon and a V polarised photon imping at input port 1 and 2 of a beamsplitter, respectively, this is denoted as $|1_H, 1_V\rangle_{\text{in}} = \hat{a}_{1,H}^{\dagger}\hat{a}_{2,V}^{\dagger}|0, 0\rangle_{\text{in}}$. To describe two unpolarised photons, we need to obtain a complete set of orthonormal basis vectors, for which we can use the four Bell states, denoted as

$$\left|\Phi^{\pm}\right\rangle_{\text{in}} = \frac{1}{\sqrt{2}} \left(\hat{a}_{1,H}^{\dagger} \hat{a}_{2,H}^{\dagger} \pm \hat{a}_{1,V}^{\dagger} \hat{a}_{2,V}^{\dagger} \right) \left|0,0\right\rangle_{\text{in}} \quad \text{and}$$

$$\left|\Psi^{\pm}\right\rangle_{\text{in}} = \frac{1}{\sqrt{2}} \left(\hat{a}_{1,H}^{\dagger} \hat{a}_{2,V}^{\dagger} \pm \hat{a}_{1,V}^{\dagger} \hat{a}_{2,H}^{\dagger} \right) \left|0,0\right\rangle_{\text{in}} .$$

(2.17)

To illustrate the photonic Bell-state measurement, let us consider a perfect, polarisation-independent 50/50 beamsplitter. In that case, all phases in the transformation matrix equal to zero and $\theta_H = \theta_V = \pi/4$, simplifying Eq. (2.16) to

$$\hat{B}_{50/50} = \frac{1}{\sqrt{2}} \begin{bmatrix} 1 & 1 \\ -1 & 1 \end{bmatrix} .$$

(2.18)

Further, assuming perfectly indistinguishable photons impinging on the beamsplitter, the photons are described by identical creation and annihilation operators with bosonic commutation relations $\left[\hat{a}_i, \hat{a}_j^{\dagger} \right] = \left[\hat{b}_i, \hat{b}_j^{\dagger} \right] = \delta_{i,j}$ and $\left[\hat{a}_i^{\dagger}, \hat{a}_j^{\dagger} \right] = \left[\hat{b}_i^{\dagger}, \hat{b}_j^{\dagger} \right] = 0$ with $i,j \in \{1,2\}$. Inserting the input states of Eq. (2.17) and transformation matrix of Eq. (2.18) into the expression of Eq. (2.15), and considering the commutation relations, results in the following output states

$$\left|\Phi^{\pm}\right\rangle_{\text{in}} \rightarrow \frac{1}{\sqrt{2}} \left(\frac{1}{2} \left(\hat{b}_{1,H}^{\dagger} \hat{b}_{1,H}^{\dagger} \pm \hat{b}_{1,V}^{\dagger} \hat{b}_{1,V}^{\dagger} \right) - \frac{1}{2} \left(\hat{b}_{2,H}^{\dagger} \hat{b}_{2,H}^{\dagger} \pm \hat{b}_{2,V}^{\dagger} \hat{b}_{2,V}^{\dagger} \right) \right) \left|0,0\right\rangle_{\text{out}}$$

$$= \frac{1}{\sqrt{2}} \left(\frac{1}{2} \left(\left|2_H, 0\right\rangle_{\text{out}} \pm \left|2_V, 0\right\rangle_{\text{out}} \right) - \frac{1}{2} \left(\left|0, 2_H\right\rangle_{\text{out}} \pm \left|0, 2_V\right\rangle_{\text{out}} \right) \right),$$

$$\left|\Psi^{+}\right\rangle_{\text{in}} \rightarrow \frac{1}{\sqrt{2}} \left(\frac{1}{2} \left(\hat{b}_{1,H}^{\dagger} \hat{b}_{1,V}^{\dagger} + \hat{b}_{1,V}^{\dagger} \hat{b}_{1,H}^{\dagger} \right) - \frac{1}{2} \left(\hat{b}_{2,H}^{\dagger} \hat{b}_{2,V}^{\dagger} + \hat{b}_{2,V}^{\dagger} \hat{b}_{2,H}^{\dagger} \right) \right) \left|0,0\right\rangle_{\text{out}}$$

(2.19)

$$= \frac{1}{\sqrt{2}} \left(\left|1_H 1_V, 0\right\rangle_{\text{out}} - \left|0, 1_H 1_V\right\rangle_{\text{out}} \right),$$

$$\left|\Psi^{-}\right\rangle_{\text{in}} \rightarrow \frac{1}{\sqrt{2}} \left(\frac{1}{2} \left(\hat{b}_{1,H}^{\dagger} \hat{b}_{2,V}^{\dagger} + \hat{b}_{2,V}^{\dagger} \hat{b}_{1,H}^{\dagger} \right) - \frac{1}{2} \left(\hat{b}_{1,V}^{\dagger} \hat{b}_{2,H}^{\dagger} + \hat{b}_{2,H}^{\dagger} \hat{b}_{1,V}^{\dagger} \right) \right) \left|0,0\right\rangle_{\text{out}}$$

$$= \frac{1}{\sqrt{2}} \left(\left|1_H, 1_V\right\rangle_{\text{out}} - \left|1_V, 1_H\right\rangle_{\text{out}} \right).$$

Inspection of Eq. (2.19) allows for the following observations: (i) the two input states $\left|\Phi^{\pm}\right\rangle_{\text{in}}$ lead to similar output conditions (up to a phase) and therefore cannot be distinguished; (ii) the input state $\left|\Psi^{+}\right\rangle_{\text{in}}$ results in two photons leaving the beamsplitter via the same output port while having different polarisations; and (iii) the input state $\left|\Psi^{-}\right\rangle_{\text{in}}$ results in two photons leaving the beamsplitter via different output ports with different polarisations. Hence, single-photon polarisation analysis in each output port of the beamsplitter allows to project the photons in the $\left|\Psi^{+}\right\rangle$ or $\left|\Psi^{-}\right\rangle$ state. Therefore, recalling the entanglement swapping protocol detailed in Section 2.1, if both photons were initially entangled with an atom, such a projection creates an entangled state of the same type between the atoms.

By assuming a perfect beamsplitter it becomes straightforward to solve the equations, which is useful to illustrate the photonic BSM. However, to investigate, e.g., the influence of experimental imperfections on the two-photon interference quality, requires the general beamsplitter
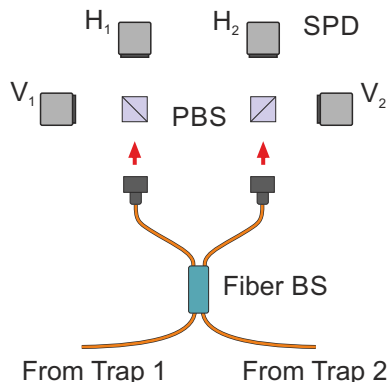
Figure 2.12: **Schematic of the photonic Bell-state measurement set-up.** Bell-state measurement set-up used in the entanglement swapping protocol. A fibre beamsplitter (BS) is used to spatially overlap and interfere the single photons originating from Trap 1 and 2. Polarising beamsplitters (PBS) in the output ports of the fibre BS project the photons in the H/V polarisation basis, after which they are detected using single-photon detectors (SPD). This set-up distinguishes 2 out of 4 Bell-states by analysing which SPD detects a photon.

transformation matrix. For an analysis considering different beamsplitter properties and experimental imperfections we refer to [106].

Photonic BSM set-up

The photonic Bell-state measurement device consist of a fibre beamsplitter (BS), two polarising beamsplitters (PBS), and four single-photon detectors (SPDs), as illustrated in Figure 2.12. Single-mode fibres guide the photons from the single-atom trap set-ups to the BSM device. The photons interfere on a balanced fibre BS which guarantees a unitary spatial overlap. Each output port of the BS contains a PBS and two single-photon detectors to analyse the polarisation of the photons. The detectors, labelled H_1, V_1, H_2, and V_2, are not photon number resolving and hence two-photon coincidence events between six detector combinations can be registered with this set-up, as listed in Table 2.1. For the purpose of a Bell-state measurement, we can categorize these combinations into three groups: D_+, D_-, and $D_\varnothing$. Here, detector combinations in group D_+ and D_- herald the Bell states $|\Psi^+\rangle$ and $|\Psi^-\rangle$, respectively, while combinations in group $D_\varnothing$ should not occur for unpolarised-photons that perfectly interfere and are therefore discarded in the analysis.

2.4.2 Two-node experiment

Implementation of an entanglement swapping protocol, as described in the previous subsection, requires centralised control of two single-atom trap set-ups. Here we detail on the two-node experiment by presenting the methods of operation, the fibre polarisation control, and the experimental sequence.

Table 2.1: **Two-photon coincidences and their probabilities.** The photons are analysed in the H/V basis and hence the detectors are labelled H_1, V_1, H_2, and V_2, where the subscript indicates the beamsplitter output port. For the purpose of a BSM, the detector coincidences are divided in four detection groups. The predicted probabilities of the coincidences are given for not- and perfectly-interfering photons.

detection	coincidence	no interference	perfect interference
	H_1,H_1	1/16	1/8
not detected	H_2,H_2	1/16	1/8
	V_1,V_1	1/16	1/8
	V_2,V_2	1/16	1/8
$D_\varnothing \rightarrow$ discarded	H_1,H_2	1/8	0
	V_1,V_2	1/8	0
$D_+ \rightarrow |\Psi^+\rangle$	H_1,V_1	1/8	1/8
	H_2,V_2	1/8	1/8
$D_- \rightarrow |\Psi^-\rangle$	H_1,V_2	1/8	1/8
	V_1,H_2	1/8	1/8

Operation of the two-node set-up

All communication between Lab 1 and 2 is performed optically at telecom wavelength [8, 104]. Therefore, a 700 m long channel containing 20 optical fibres connects the laboratories and electro-optical (EO) converters transform electrical and optical signals. The experimental control is based on a master (Lab 1/Node 1) and minion (Lab 2/Node 2) configuration. Each trap is controlled locally via (i) a PC for processes at millisecond time-scales, whereby the Master PC sends commands to the Minion PC via a direct optical Ethernet connection, and (ii) a homebuilt control unit (CU) for control at nanosecond time-scales, having a time-resolution of 20 ns and jitter of < 40 ps [8].

Time critical signals are synchronized via a 100 MHz clock located in Lab 2, which is optically distributed to Lab 1. The CUs use the clock signal to synchronise the experimental sequences with a relative jitter of < 150 ps. The CU in Lab 1 is then used to specify the two-photon coincidence time-window and as time reference in the data acquisition process. The synchronization of the experimental sequences is continuously monitored in Lab 1.

A home-built time-to-digital converter (TDC) located in Lab 1 records the data by timestamping logic signals with a resolution of 80 ps for 8 channels. Recorded are the photon detections of the four SPDs employed in the BSM, together with the timings of the excitation pulse and fluorescence readout of Trap 1.

The PCs control the loading of the traps and start the entanglement generation tries as follows. The Master PC begins loading of Trap 1 and, via a command to the Minion PC, Trap 2. Photon counts of the trapping APDs in both nodes are sent to a counter in Lab 1, which is connected to the Master PC. When the number of fluorescence counts integrated over 40 ms exceeds a set threshold for both nodes, the Master PC commands the Minion PC to start the entanglement generation tries. The start signal to the CUs originates from Lab 2 and hence results in similar time difference between the start signal in the two nodes relative to the first excitation try.

Fibre polarisation control

Both single-atom traps require a single mode fibre connection to the BSM set-up, which is located in Lab 1. For Trap 1, this is realised via a 5 m long fibre, for Trap 2, in contrast, a 700 m long fibre channel is installed to facilitate the exchange of photons between the labs, crossing public space including a four-lane road, as can be seen in Figure 2.2. Therefore, unavoidable temperature and stress induced polarisation drifts in the 700 m long fibre require extra attention and should be actively compensated for.

Polarisation drifts in the long fibre are monitored and compensated for using a home-built control system [8, 122]. For this, so-called compensation light at the single photon frequency is overlapped with the complete single-photon path originating from Node 2. A liquid crystal retarder (LCR) alternates the polarisation of the compensation light at the position of the atom between V and D linear polarisation states with 10 Hz. At an output port of the BSM set-up, and hence after propagating through the 700 m long fibre, a flip mirror reflects the compensation light into a polarimeter. The polarisation in the long fibre is controlled by introducing stress with piezo elements.

Based on the set-up described above, a gradient descent algorithm compensates polarisation drifts employing the polarimeter measurements as input and the piezo voltages as output. The piezo voltages are set according to the results of the gradient descent algorithm, which completes in about 5 s. When the algorithm is executed every 5 min polarisation errors are kept below

1%.

Experimental sequence

The experiment starts by trapping an atom in both nodes. For this, a single atom is loaded from a magneto-optical trap (MOT) into a tightly focussed dipole trap, which takes 1–2 s, as described before in Section 2.2. Next, we generate atom-photon entanglement in each node, as discussed in Section 2.3.1. Therefore, the atoms are prepared in the initial state $5^2 S_{1/2} |F = 1, m_F = 0\rangle$ via optical pumping and synchronously excited to the state $5^2 P_{3/2} |F' = 0, m_F = 0\rangle$. During the spontaneous decay back to the ground state the atomic spin state becomes entangled with the polarisation of the respective emitted photon at 780 nm, resulting in the entangled atom-photon state $|\Psi\rangle_{\text{ap}} = 1/\sqrt{2}(|\downarrow\rangle_z |L\rangle + |\uparrow\rangle_z |R\rangle) = 1/\sqrt{2}(|\downarrow\rangle_x |V\rangle + |\uparrow\rangle_x |H\rangle)$. High-NA objectives collect the single photons into single-mode fibres, which guide them to the BSM setup, where the 700 m long fibre to the BSM for Trap 2 introduces a channel loss of a factor $1/2$.

The photons are interfered and analysed in the linear polarisation basis H/V in the BSM and hence a coincidence detection results in the maximally entangled atom-atom states

$$|\Psi^{\pm}\rangle = \frac{1}{\sqrt{2}}(|\uparrow\rangle_x |\downarrow\rangle_x \pm |\downarrow\rangle_x |\uparrow\rangle_x). \qquad (2.20)$$

Two-photon events are accepted in a 208 ns window and trigger a heralding signal back to the trap set-ups, where the atomic states are individually analysed using a state-selective ionisation scheme (see Section 2.3.2). In analogy to the one-node experiments, the entanglement generation tries are executed in bursts of 40 after which the atoms are cooled for 350 μs to minimize atomic motion, resulting in a repetition rate of 52 kHz.

The expected two-photon coincidence success probability equals $\eta_{\text{aa}} = \frac{2}{4}\eta_{\text{ap}_1}\eta_{\text{ap}_2} \approx 8 \times 10^{-6}$. Accounting for the repetition rate mentioned above and the experimental duty cycle of approximately half, this results in an expected event rate of $1/5$ s^{-1}.

2.4.3 Two-photon interference contrast

The two-photon interference necessary for BSM is optimized by different means, first, the photons impinge on a balanced, single-mode fibre beam splitter to guarantee a perfect spatial overlap. Second, the entanglement generation process in the nodes is synchronized to < 300 ps, which is much smaller than the lifetime of the excited state of 26.2 ns. And third, all fields at the atom positions are minimized during the atom-photon entanglement generation process to impose indistinguishable frequencies of photons emitted by the atoms stored in Trap 1 and 2.

Experimental imperfections limit the interference quality; references [102] and [106] give a very detailed overview of many different origins of errors during the atom-photon entanglement generation process, which will not be repeated here. Most significant, however, are double excitation events in one node, as visualised before in Figure 2.8. In particular, after an intended atomic excitation followed by a decay back to the initial state $5^2 \text{S}_{1/2} |F = 1, m_F = 0\rangle$—which occurs in $1/3$ of the atomic decays—a second excitation according to the intended process is likely. While generating the targeted atom-photon state with a high fidelity, the temporal dependence of the emitted photon wave function, however, is influenced, which limits the two-photon interference contrast by introducing which-path information. Since this effect is time dependent, i.e., a second excitation can only occur subsequent to a first emission and the first decay must occur while the excitation pulse is still present, conditioning of the BSM on the
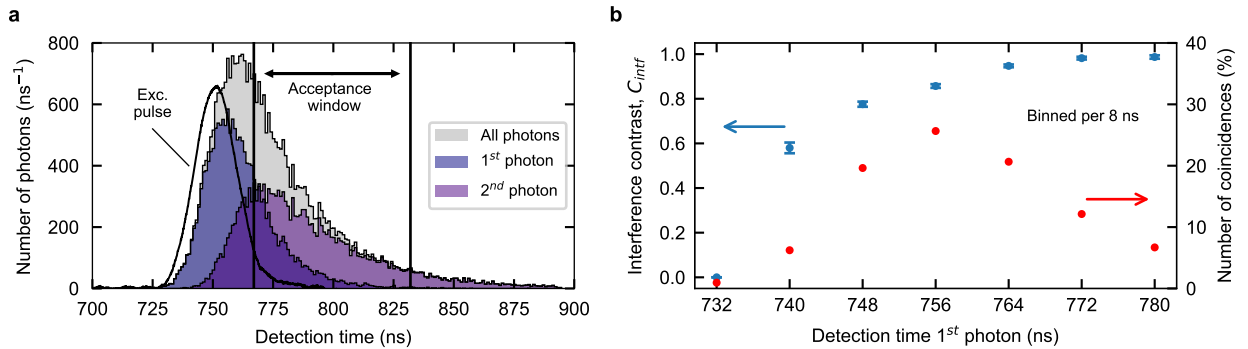
Figure 2.13: **Photon detection time histogram and interference contrast. a**, The detection time histogram of all detected photons, further divided into the 1st and 2nd detected photon. Coincidences where both photons arrive within the chosen acceptance window (767–832 ns) are selected for the atom-atom state analysis, for which the interference contrast equals $C_{\text{intf}} = 0.980(4)$. **b**, Interference contrast and number of coincidences for different 1st photon detection times binned per 8 ns, e.g., the data points at 740 ns includes 1st photon detection times during the interval 736–744 ns.

photon detection times can be used to filter out which-path information, i.e., double excitation events, and potentially increase the two-photon interference contrast.

The entanglement swapping fidelity is evaluated by analysing the relative occurrence of the two-photon coincidence groups [55, 102], as listed before in Table 2.1. For not interfering photons, two-photon events are evenly distributed between the $4 \times 4 = 16$ possible detector combinations, that is, all detector combinations occur with a probability of 1/16 (not considering experimental imperfections, such as different detection efficiencies of the SPDs or an imbalanced beam splitter). Since the order of the detector combination is not of interest in this analysis, e.g., (V_1,H_1) is similar to (H_1,V_1), we end up with 10 distinct coincidences and their probabilities. For perfectly interfering photons the probabilities differ: the probability to detect the $D_\varnothing$ group vanishes and all four Bell states are detected with a probability of 1/4, whereby the $|\Phi^\pm\rangle$ Bell states fall into the group 'not detected' for the employed BSM set-up. Accordingly, the two-photon interference contrast is defined as

$$C_{\text{intf}} = 1 - \frac{2N_{D_\varnothing}}{N_{D_+} + N_{D_-}}, \tag{2.21}$$

where N_k is the number of events in detection group k. With this definition and the theoretical probabilities of the different coincidences, the contrast equals zero for not interfering photons and one for perfectly interfering photons.

The interference contrast is measured as follows. During the experiment all single-photon detection events are recorded, which allows to count the number of occurrences of the coincidence events for all three detection groups. Next, the interference contrast is evaluated using Eq. (2.21). Figure 2.13a shows a photon detection time histogram of two-photon coincidences. The photons originate from atoms stored in Trap 1 and 2 and the registration of a coincidence heralds the entanglement between the atoms. For all coincidences, the photons are shown individually (1st and 2nd photon) and as a sum (all photons), together with the temporal shape of the excitation pulse relative to the time of atomic excitation. Furthermore, the two-photon interference contrast is calculated and visualised for different detection times of the 1st photon,
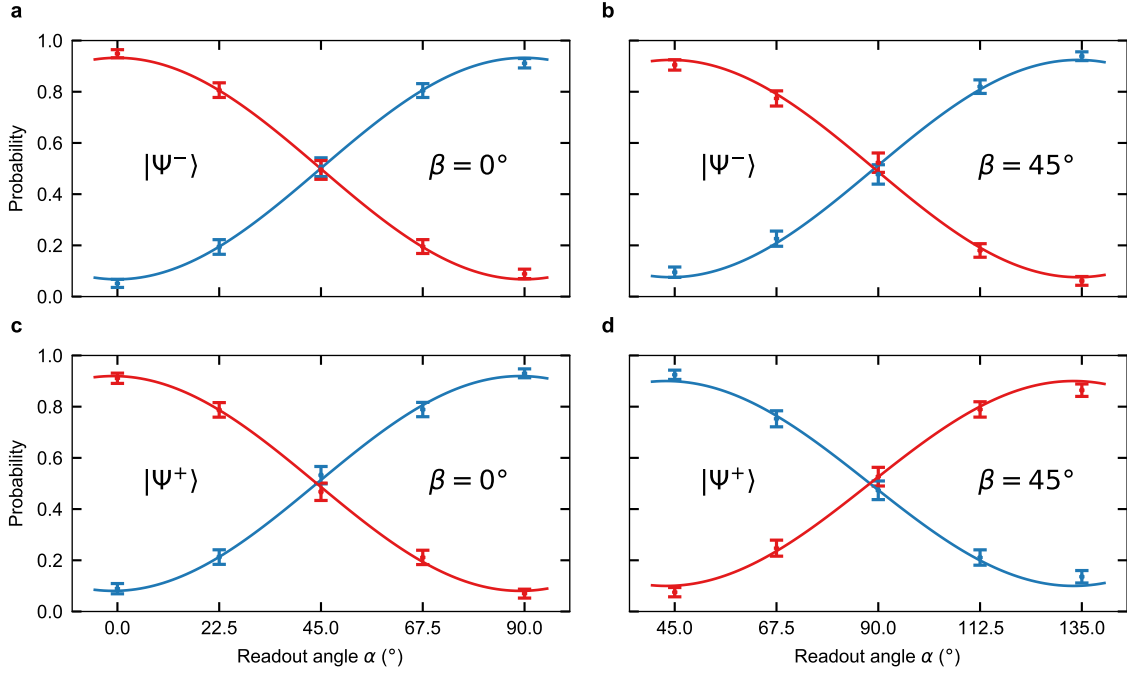
Figure 2.14: **Observed atom-atom state correlations.** The correlation probability (blue) and anti-correlation probability (red) of the measurement results of the atoms for the states $|\Psi^-\rangle$ (**a**, **b**) and $|\Psi^+\rangle$ (**c**, **d**). The atoms are analysed in the H/V basis (**a**, **c**) and the D/A basis (**b**, **d**). The estimated state fidelity equals $0.873(17)$ for the state $|\Psi^-\rangle$ and $0.840(18)$ for the state $|\Psi^+\rangle$. The total number of events in **a**–**d** equals $N = 4\,040$ resulting in an average of 202 events per measurement setting.

as shown in Figure 2.13b—note that the 1st photon can originate from Trap 1 or 2. For 1st photon detection times during the excitation pulse the interference contrast is reduced; discarding these coincidences effectively filters out double excitation events and hence increases the indistinguishably of the photons resulting in high quality entanglement swapping. Accepting coincidences in the window 767–832 ns results in an interference contrast of $C_{\text{intf}} = 0.980(4)$, while selecting $\eta_{\text{tf}} = 0.24$ of the events.

2.4.4   Demonstration of atom-atom entanglement

Atom-atom state correlations and fidelity

Subsequent to a two-photon coincidence, the atom-atom entanglement quality is analysed. For this, we measure the atomic spin states in the two linear bases, H/V and D/A, by setting the polarisation analysis angle in Trap 2 to $\beta = 0°$ or $\beta = 45°$, while varying the analysis angle in Trap 1 over $90°$ in steps of $22.5°$ starting from $\alpha = 0°$ or $\alpha = 45°$, respectively. The atom in Trap 1 (Trap 2) was analysed at $t_1 = 28.5\ \mu s$ ($t_2 = 35.5\ \mu s$) after the respective excitation pulse. The resulting atomic state correlation probabilities $P_{\text{corr}} = (N_{\uparrow\uparrow}^{\alpha,\beta} + N_{\downarrow\downarrow}^{\alpha,\beta})/N^{\alpha,\beta}$ and anti-correlation probabilities $P_{\text{acorr}} = (N_{\uparrow\downarrow}^{\alpha,\beta} + N_{\downarrow\uparrow}^{\alpha,\beta})/N^{\alpha,\beta}$ are shown in Figure 2.14. The data are fitted with sinusoidal curves giving average visibilities of $\bar{V} = 0.857(19)$ for $|\Psi^-\rangle$ and $\bar{V} = 0.820(20)$ for $|\Psi^+\rangle$.

To estimate the entangled state fidelity relative to a maximally entangled state, one needs to consider that a third Zeeman state of the atom can be populated, in analogue to the atom-photon entanglement fidelity estimation described in Section 2.3.2. The atom-atom state effectively occupies a 3×3 state space. When assuming isotropic dephasing towards white noise the density matrix of the atom-atom state is given by

$$\hat{\rho} = \overline{V} \, |\Phi_{\mathsf{aa}}\rangle \, \langle\Phi_{\mathsf{aa}}| + \frac{1}{9}(1 - \overline{V})\hat{\mathbb{1}}, \tag{2.22}$$

where $\bar{V}$ is average visibility in three orthogonal bases. This allows to lower bound the fidelity relative to a maximally entangled state by

$$\mathcal{F}_{\mathsf{aa}} \geq \langle\Phi_{\mathsf{aa}}| \, \hat{\rho} \, |\Phi_{\mathsf{aa}}\rangle = 1/9 + 8/9\overline{V}, \tag{2.23}$$

which equals to 0.873(17) for $|\Psi^-\rangle$ and 0.840(18) for $|\Psi^+\rangle$, relative to a maximally entangled state. The commonly used fidelity estimation from visibilities for an entangled 2-qubit system is $\mathcal{F} \geq 1/4 + 3/4\bar{V}$. For the effective 2-qutrit system, however, this would result in a higher fidelity and would overestimate the fidelity of the generated atom-atom state.

CHSH Bell test

The chosen analysis angles also allow to evaluate the Clauser-Horne-Shimony-Holt (CHSH) S value [123] for the settings $\alpha = 22.5°$, $\beta = 0°$; $\alpha' = 67.5°$, $\beta = 0°$; $\alpha' = 67.5°$, $\beta = 45°$; and $\alpha'' = 112.5°$, $\beta' = 45°$, whereby α'' replaces $\alpha = 22.5°$. This results in an observed value of $S = 2.24(12)$ for $|\Psi^-\rangle$ and $S = 2.41(11)$ for $|\Psi^+\rangle$. Combining the data of the states $|\Psi^\pm\rangle$ gives $S = 2.32(8)$, violating the limit of 2 with 4σ.

2.5   Coherence of the atomic state

The realisation of quantum networks requires to store quantum states in the network nodes. More specifically, to generate heralded entanglement between two nodes, for example following the methods described in the previous section, the employed quantum memories should store the entanglement at least up to the moment the heralding signal arrives back at the nodes. Hence, approximating the speed of light in an optical fibre by $\frac{2}{3}c$, requiring a minimal quantum memory storage time of 5 μs for every 1 km of fibre link length between two nodes. Since the experiments presented in Chapter 4 and 5 aim to increase the reach of the quantum network link, accurate characterisation and optimisation of the memory coherence time becomes relevant.

In this section, we describe the interaction of the atomic state with an effective magnetic field, list the main decoherence sources, and detail on the effect of a magnetic bias field on the atomic state coherence time, for which we follow previous work [100, 104, 106, 107]. Further, we detail on simulation, optimisation, and characterisation of the atomic state coherence.

2.5.1   Evolution of the atomic state

Interaction with an effective magnetic field causes an evolution of the atomic state, as will be described below for the $F = 1$ manifold of the ^{87}Rb ground-state. In general, evolution of the atomic state is unwanted and in particular fluctuating or position-dependent fields cause the atomic state to decohere and hence limit the coherence time. However, evolution in a constant field does not lead to dephasing and when the field is known, careful selection of the readout time and orientation still allows for a high-fidelity state readout.

Interaction with an effective magnetic field

The interaction Hamiltonian $\hat{H}_B$ describes the interaction between the atomic spin state and a magnetic field B. For the quantization axis in z-direction, basis vectors $|1, -1\rangle_z$, $|1, 0\rangle_z$, and $|1, +1\rangle_z$, and a magnetic field

$$\vec{B} = \begin{bmatrix} B_x \\ B_y \\ B_z \end{bmatrix}, \tag{2.24}$$

the interaction Hamiltonian is given by

$$\hat{H}_B = \frac{\mu_B g_F}{\hbar} \vec{B} \vec{F} = \hbar \omega_L \begin{bmatrix} b_z & \frac{1}{\sqrt{2}}(b_x - ib_y) & 0 \\ \frac{1}{\sqrt{2}}(b_x + ib_y) & 0 & \frac{1}{\sqrt{2}}(b_x - ib_y) \\ 0 & \frac{1}{\sqrt{2}}(b_x + ib_y) & -b_z \end{bmatrix}. \tag{2.25}$$

Here, $b_k = B_k/\|B\|$ for $k \in \{x, y, z\}$, g_F denotes the Landé factor of the hyperfine state, μ_B denotes the Bohr magneton, and the Larmor frequency is defined as $\omega_L = g_F \mu_B \|B\|/\hbar$. Moreover, $\vec{F}$ is the operator of the angular momentum of the $F = 1$ space, an effective spin-1 system. Using cylindrical coordinates, i.e., $b_x = \sqrt{1 - b_z^2} \cos(\phi)$ and $b_y = \sqrt{1 - b_z^2} \sin(\phi)$, results in the eigenvalues $\lambda_{\pm 1} = \pm \hbar \omega_L$ and $\lambda_0 = 0$, with eigenvectors

$$|\Phi_{\pm 1}\rangle = \begin{bmatrix} -\frac{1}{2}(b_z \pm 1)e^{-i\phi} \\ -\sqrt{\frac{1-b_z^2}{2}} \\ \frac{1}{2}(b_z \mp 1)e^{i\phi} \end{bmatrix} \quad \text{and} \quad |\Phi_0\rangle = \begin{bmatrix} -\sqrt{\frac{1-b_z^2}{2}}e^{-i\phi} \\ b_z \\ \sqrt{\frac{1-b_z^2}{2}}e^{i\phi} \end{bmatrix}. \tag{2.26}$$

The evolution of an arbitrary state is now described by

$$|\Psi(t)\rangle = c_{-1} |\Phi\rangle_{-1} e^{i\omega_L t} + c_0 |\Phi\rangle_0 + c_{+1} |\Phi\rangle_{+1} e^{-i\omega_L t}, \tag{2.27}$$

with $c_{-1}, c_0, c_{+1} \in \mathbb{C}$ and $\sqrt{\|c_{-1}\|^2 + \|c_0\|^2 + \|c_{+1}\|^2} = 1$.

Decoherence effects

The atomic state decoherence mainly originates from two sources: the first one arises from magnetic fields by the Zeeman effect and, the second one, is optically induced by the dipole trap via the ac-stark shift. Since the ODT light is far red-detuned, scattering of photons on the timescales of < 1 ms can be neglected.

    Magnetic fields lead to an energy shift of the Zeeman states described by Eq. (2.25), for example, along the quantization (z-)axis as

$$\Delta E_{\mathsf{Zeeman}} = \mu_B g_F m_F B_z. \tag{2.28}$$

While a constant field does not lead to dephasing, magnetic field fluctuations do reduce the atomic coherence time. Moreover, since atomic state analysis involves averaging over many atomic state measurements, magnetic field drifts and shot-to-shot noise further decrease the observed visibility since they cause a different state evolution according to Eq 2.27, and hence wash out the contrast. In the set-ups, the magnetic field is stabilised along three directions to < 0.5 mG.
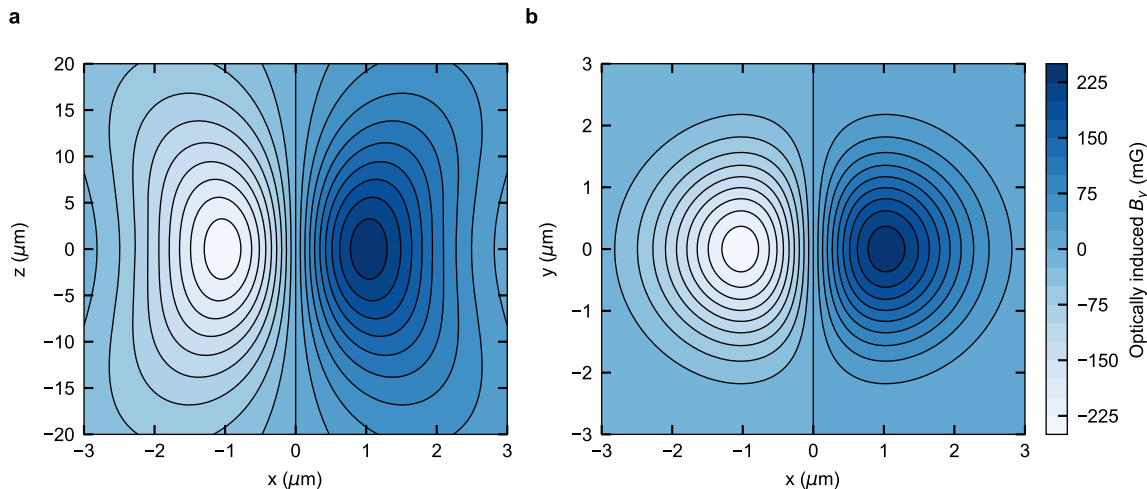
Figure 2.15: **Longitudinal field components of the optical dipole trap.** Optically induced magnetic field components (effective B_y field) for a dipole trap with a waist of $\omega_0 = 2.05$ μm and trap depth of $U_0 = 2.32$ mK. **a**, Position dependent effective magnetic field B_y in the x,z-plane for y=0. **b**, Position dependent effective magnetic field B_y in the x,y-plane for z=0.

Circular polarisation of the ODT introduces an energy shift between the Zeeman states. Eq. (2.6) assumes perfect linear polarisation of the ODT, however, in the experiment, circular polarisation components are present. Defining a measure of circularity as $P = 0$ for π-polarised light and $P = \pm 1$ for $\sigma^{\pm}$-polarised light [106], allows to write the energy difference induced between the m_F states by the dipole trap, i.e., the vector light-shift, as

$$\Delta E_{m_F}(r, z) = -\frac{\pi c^2 \Gamma}{2\omega_0^3} \left(\frac{g_F m_F P}{\Delta_{2,F}} - \frac{g_F m_F P}{\Delta_{1,F}} \right) I(r, z). \tag{2.29}$$

Note that the energy shift is equivalent to a magnetic field in z-direction. Further, it is intensity and therefore position dependent, leading to dephasing of the atomic state due to movement of the atoms in the trap. The circularity of the dipole trap light is minimized by aligning the polariser of the ODT to the polarisation eigenaxis of the trap set-up, reducing the energy shifts to an equivalent of $B_z < 0.1$ mG. Therefore, circular dipole trap light components are not the main limitation of the atomic coherence time. Furthermore, a guiding field of tens of milligauss perpendicular to the z-axis could further suppress this effect, as will be described below.

Strong focussing of the ODT leads to longitudinal field components around the focus, as detailed in [100, 104, 106, 107]. In the presented set-up, this results in effective B_y fields, as illustrated in Figure 2.15. A trapped atom experiences a field strength depending on its confinement, i.e., the atomic temperature. For typical atomic temperatures and trap depths of around 50 μK and $U_0 = 2.32$ mK, respectively, the atoms experience effective B_y fields larger than 100 mG. However, since the absolute field values are symmetric around the z-axis and have opposite sign, the phase accumulated after a full transversal oscillation approximates zero and hence still allows for a high fidelity state readout.
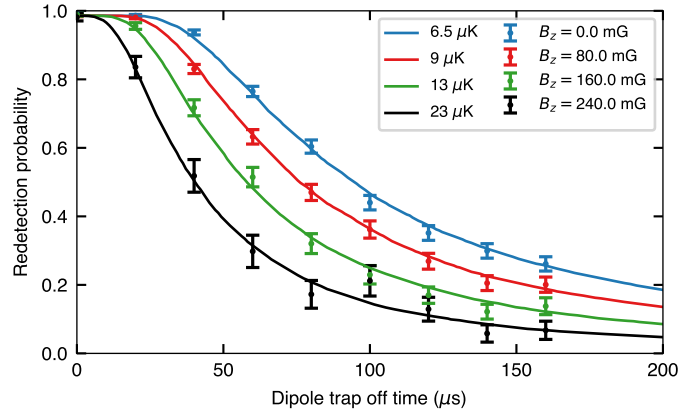
Figure 2.16: **Atomic temperature dependence on a magnetic bias field.** Determining the atomic temperature for different bias fields by the release and recapture technique. The solid lines are simulations for different atomic temperatures T. The ODT is adiabatically ramped down to $U_0 = 0.19$ mK, which results in atomic temperatures below 50 μK.

Function of a magnetic bias field

Applying a magnetic bias field B along a certain direction does not change the sensitivity for fields along that direction ($B_\parallel$). In this case, the absolute field value is simply described by

$$B \rightarrow B + \Delta B_\parallel. \tag{2.30}$$

However, for a field perpendicular to the bias field ($B_\perp$), the absolute value of the field changes according to

$$B \rightarrow \sqrt{B^2 + \Delta B_\perp^2}. \tag{2.31}$$

As a result, when the bias field is strong $B \gg B_\perp$, fields perpendicular to this field are substantially suppressed. This can increase the atomic coherence time in multiple ways. For one, it reduces the number of directions the atomic state is susceptible to magnetic field fluctuations from three to one. Furthermore, unwanted effective magnetic fields, e.g., introduced by the ODT light, could be mitigated.

Besides suppressing perpendicular field components, a bias field influences the efficiency of the polarisation gradient cooling and hence the atomic temperature [116]. We characterised the atomic temperature for different bias field strengths $B_z =$ 0–240 mG using the release and recapture technique [124], as is shown in Figure 2.16. Accordingly, the atom is released from the dipole trap by switching off the trap light for a certain period of time, after which one checks if the atom is still present in the trap, i.e., is recaptured by the dipole trap. The atomic temperature is obtained by matching the data to a simulation where the atomic temperature is modelled as a Boltzmann distribution [104, 124]. To overcome this dependency, fast switching of the magnetic bias field between cooling and entanglement generation periods enables for low atomic temperatures while achieving high bias fields.

2.5.2 Characterisation and simulation of the atomic coherence

Optimising the atomic coherence

To maximise the atomic coherence time and improve stability, a bias field of tens of milligauss along the y-axis was applied in the experiments presented in this thesis. A guiding field simplifies the optimisation process of the magnetic field, which requires setting of the bias field only, instead of optimisation in three directions when operating close to a zero magnetic field—thereby also simplifying a potential implementation of automated magnetic field optimisation [125]. Further, a bias field along the y-axis was chosen since it matches the direction of the longitudinal field components of the ODT, which act as effective B_y fields. Hence the longitudinal field components are not suppressed, however, the effect caused by the vector light shifts introduced by the ODT, which act as effective B_z fields up to 1 mG, and magnetic field fluctuations and drifts along the x- and z-axis of up to 3 mG are suppressed. In contrast, bias fields along the x- or z-axis of tens of milligauss would result in shorter coherence times since they allow for mixing of the atomic states together with the longitudinal field components of the ODT. Higher bias fields (> 100 mG) are avoided since they reduce the efficiency of the initial state preparation and polarisation gradient cooling, as well as requiring faster readout times.

In further experiments, in order to suppress the longitudinal field components of the ODT a magnetic bias field along the z-axis (or x-axis) could be introduced. For this, the strength of the longitudinal fields should be reduced which could be achieved by either introducing a standing wave dipole trap or adiabatically ramping down the trap depth, see [126] for simulations of both approaches. Moreover, suppression of the longitudinal field components enables for the implementation of a robust qubit encoding to lower the sensitivity to magnetic field fluctuations along the z-axis by a factor of > 500, which would further increase atomic coherence times [63, 127].

Simulating the atomic coherence

To model the dephasing of the quantum memories, we simulate the evolution of the spin-1 system while the atom is oscillating in the dipole trap, affected by longitudinal polarisation components and external magnetic fields [100, 104]. For this, first, we randomly draw a starting position and velocity of an atom from a 3D harmonic oscillator distribution in thermal equilibrium. Second, the motion of the atom is simulated in a realistic Gaussian potential resulting in an atomic trajectory for which the evolution of the atomic state is calculated based on the local optically induced and external magnetic fields. Finally, this is repeated for a large number of trajectories, whereby the averaged projection for all trajectories yields the simulation result.

The model takes the following independently measured inputs: (1) the trap geometry specified by the beam waist $\omega_0 = 2.05$ μm, which is obtained from knife-edge measurements of the dipole trap beam focus in two dimensions [107]; (2) the trap depth $U_0 = 2.32$ mK, determined via measurements of the transverse trap frequency using parametric heating [128] and the atomic state rephasing period [104]; and (3) the atomic temperature $T = 50$ μK, modelled as a Boltzmann distribution which is measured via the release and recapture technique [124]. Inputs (1) and (2) define the position, amplitude, and phase of the longitudinal polarisation components, while inputs (1–3) characterize the atomic trajectories. Furthermore, we include a uniform magnetic field along three directions with $B = [0, 75.5, 0]$ mG including additional trajectory-to-trajectory noise following Gaussian distributions of $\Delta B = [0.5, 0.5, 0.5]$ mG.

Figure 2.17 shows the simulation results and measurement data of the state evolution in Node
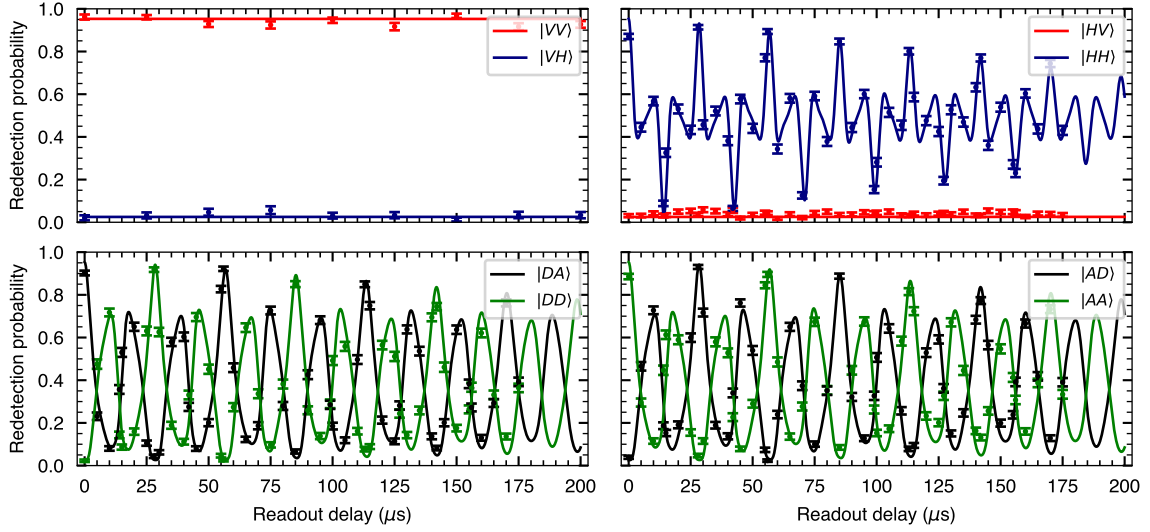
Figure 2.17: **Measurements and simulations of the atomic state evolution.** Atom-photon entanglement simulations (solid lines) and measurements (points) of Node 1. The atomic state readout orientation and time are varied to characterise the memory coherence time $T_2 = 330 \ \mu$s. The labels in the legend indicate the |atom photon⟩ state analysed. Simulation parameters: bias field $B_y = 75.5$ mG, field fluctuations $\Delta B_y = 0.5$ mG Gaussian distributed, atom temperature $T = 50 \ \mu$K, trap waist $\omega_0 = 2.05 \ \mu$m, and trap depth $U_0 = 2.32$ mK.

1 for varying state readout orientation and time for a magnetic bias field of $B_y = 75.5$ mG. In the top two panels, the atom-photon state is analysed and simulated in the H/V basis and in the the bottom two panels in the D/A basis. In each panel, the readout orientation of the photon and atom state is kept fixed, as indicated in the legend, while delaying the atomic readout time up to 200 μs. The model accurately predicts the evolution of the measured atomic states and shows a memory storage time of $T_2 = 330 \ \mu$s, which is limited by magnetic field fluctuations on the order of < 0.5 mG along the bias field direction in addition to the position-dependent dephasing due to the longitudinal field components of the strongly focussed dipole trap. Both decoherence effects contribute to effective magnetic field noise along the y-axis and hence contribute to decoherence of the $|H\rangle$ state. For this reason, a photonic projection on the $|V\rangle$ state has a longer coherence time and the visibility of this state does not significantly decrease up to a storage time of 200 μs (red lines and data-points in Figure 2.17). Note that the observed contrast for longer readout delays in the D/A basis is lower than expected from the simulation. This discrepancy is investigated further in Section 5.4. The simulation results presented in the next chapters of this thesis consider the envelope of the found oscillating state evolution averaged over three bases.

To quantify the impact of the different decoherence effects on the coherence time, we simulated the state evolution when removing these effects from the model. Figure 2.18 shows simulations for the readout orientation $|HH\rangle$ (similar readout orientation as in the top right panel of Figure 2.17) for the complete model (blue solid line), the model but without effects introduced by the ODT ($B_{\text{long}} = 0$, blue dashed line), and the model but without the ODT effects and magnetic field fluctuations ($B_{\text{long}} = 0$ and $\Delta B = 0$, blue dotted line). The last simulation (blue dotted line) shows no reduction of the amplitude of the oscillations up to 200 μs, and

35
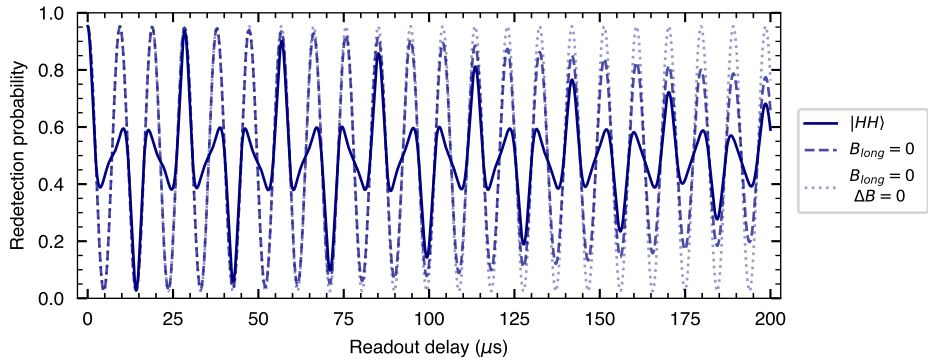
Figure 2.18: **Simulations of the atomic decoherence processes.** Atom-photon entanglement simulations for the readout orientation $|HH\rangle$ using three different models. The solid line represent the complete model, as presented before and shown in the top right panel of Figure 2.17. The dashed line represents the same model, however, without the effective fields introduced by the ODT, i.e., $B_{\mathsf{long}} = 0$. Finally, in the simulation result shown by the dotted line, the magnetic field fluctuations are taken out of the model as well, i.e., $B_{\mathsf{long}} = 0$ and $\Delta B = 0$. In the last, no decoherence is visible up to 200 μs.

hence no decoherence. For the selected readout orientation and a readout delay of 170.2 μs, the simulations show a reduction in contrast by around 9.2% due to longitudinal field components and 13.9% due to magnetic field fluctuations.

Chapter 3

Device-Independent Quantum Key Distribution

This chapter presents a proof-of-concept device-independent quantum key distribution (DI-QKD) experiment. For this, we employ the event-ready entanglement generation setup introduced in Chapter 2 and implemented the protocol proposed by Schwonnek et al. (2020) [113]. In the used protocol, a loophole-free Bell-test using entangled single ^{87}Rb atoms validates the secrecy of a key shared by two users located in laboratories separated by 400 m line-of-sight secure against attacks on the quantum channel, but, for the first time, also against certain attacks and manipulations of the devices that are used for the quantum key exchange. We demonstrate a positive asymptotic secret key fraction—the ratio of achievable secret key length to the total number of protocol rounds—of 0.07 in a fully device independent configuration. Work presented in this chapter resulted in the publications Zhang, Van Leent, *et al. Nature* **607**, 687–691 (2022) and Zapatero, Van Leent, *et al. npj Quantum Information* **9**, 10 (2023), and some parts of the text are based on these publications.

This chapter is organized as follows. In Section 3.1 we give a general introduction to quantum key distribution and stress the advantages of device-independent protocols. Thereafter, in Section 3.2, the scenario and security assumptions for DI-QKD are detailed. Section 3.3 discusses different experimental platforms to implement DI-QKD, distinguishing all-photonic and memory-based implementations. Section 3.4 describes our implementation, detailing on the protocol, quantum network link, and implementation of the protocol. Next, in Section 3.5, the experimental results are presented by reflecting on the performance of the quantum network link independent from, and with respect to, the protocol. Further, in Section 3.6, we detail on two simultaneously conducted proof-of-concept DI-QKD experiments. The chapter concludes with Section 3.7, summarizing the results and describing further improvements to enable finite-key generation in a device-independent setting using single atoms.

3.1 Introduction

Private communication over public infrastructure is of great importance in everyday life. When communicating parties share a common secret key, provably-secure communication over public channels can be realised. The classical generation of such keys, however, relay on the hardness of computational challenges and is not information-theoretically secure. Quantum key distribution (QKD) [129, 130] promises to solve this issue by using the unique features of quantum mechanics to exchange secret keys over an untrusted network. The technology is now well established in a

wide variety of network settings [131–140] and commercial QKD systems are available.

QKD protocols are designed to detect eavesdropping attacks on the quantum channel based on fundamental quantum effects like the no-cloning theorem and the uncertainty principle. However, in order to leverage these effects, QKD protocols require that the underlying quantum devices are well characterised and are accurately described by the mathematical models used in the security analysis. The users of such protocols must therefore trust not only the honesty of the QKD vendors, but also the specifications provided by them. This may be critical: indeed, it has been known for at least a decade that some QKD devices can be readily hacked from the outside by exploiting physical features that had not been deemed relevant in a first analysis, for an overview see [141].

To overcome the above issues, a promising solution is to use device-independent QKD (DI-QKD)—an entanglement-based method which allows the users to exchange secret keys with uncharacterised (or untrustworthy) quantum devices. First introduced by Mayers and Yao [37], DI-QKD [38, 39, 142–146] ensures the proper and secure functioning of the underlying QKD devices via a loophole-free Bell test [2, 147]. More specifically, the users only need to analyse their input-output measurement statistics to put an upper bound on the amount of information leaked to an eavesdropper, hence eliminating the requirement to characterise the devices. DI-QKD at the same time automatically provides security against implementation flaws and especially any form of misalignment. It only requires a few very basic assumptions to be fulfilled.

The experimental realisation of DI-QKD is, however, a major challenge. The main difficulty is to devise a system that enables for a loophole-free Bell test while achieving both a high Bell violation and a low quantum bit error rate (QBER). State-of-the-art loophole-free Bell experiments [5–9] are able to achieve significant Bell violations, but the QBERs were still not good enough for DI-QKD (e.g., see the survey provided by Ref. [40]). To lower these requirements, one approach is to devise DI-QKD protocols which are more robust and efficient. Recently, this yielded two improved variants of the original DI-QKD protocol—one based on noisy-preprocessing [148] and the other based on randomised key setting [113]. Another path is via significant improvements of many parts of existing Bell-test set-ups.

3.2 Scenario and requirements

The scenario

Let us first sketch the general scenario of QKD. Two parties, named Alice and Bob, want to establish a secret key to exchange private messages. Here, a secret key is a string of bits that is known to the two parties, but to no one else—in other words: shared secret randomness, which is used to encode and decode the private messages. QKD allows for the generation of such secret keys in the presence of an adversary, commonly named Eve. This requires the following resources:

1. Secure locations—any cryptographic application is pointless without the availability of secure locations. When this is not the case, the messages are not private to start with. Therefore, we must assume that Alice and Bob operate in a secure location. In practice, this cannot be guaranteed unconditionally, however, this is no problem specific for QKD.

2. Local randomness—a source of randomness to generate inputs that are unknown to the used devices and potential eavesdroppers. Note that the inputs can be known to the user of the device they are used for, however, not to the other party.
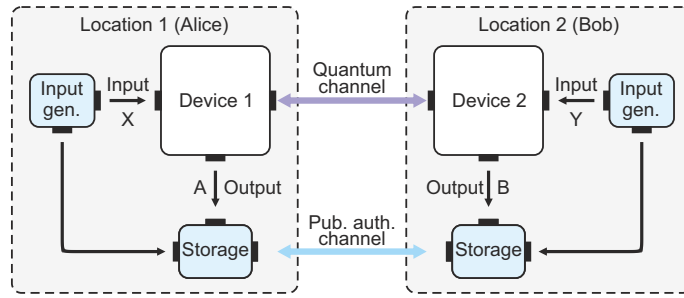
Figure 3.1: **Schematic of the DI-QKD connection.** Each of the two parties, Alice and Bob, holds one of the two QKD devices which are connected via a quantum channel. The devices receive the inputs X and Y, and respond with outputs A and B, respectively. To run the protocol each party needs a trusted supply of inputs and a trusted local storage unit to store both output and inputs. Additionally, a trusted authenticated public channel between the two parties is necessary for exchange of information during post-processing. Adapted from [149].

3. Authenticated public channel—a public communication channel for the post-processing steps of the protocol. To establish this channel, the parties need to share secret randomness prior to the start of the protocol. Accordingly, QKD could be named quantum key expansion.

4. Local storage and processing—a trusted platform to store the measurement results and execute the post-processing steps.

5. Quantum channel and devices—the quantum states are distributed via the quantum channel and the devices measure the states. Note that in the device-independent scenario the devices are assumed to be black boxes, i.e., no assumptions are made about the inner workings.

In the device-independent scenario, as illustrated in Figure 3.1, the secrecy of the key distribution is tested by a loophole-free violation of a Bell inequality. In this way, by simply analysing the input-output measurement statistics of their devices, the users can bound the information possibly known to an eavesdropper. Simultaneously, the Bell-test verifies the proper functioning of the employed devices.

Security assumptions for DI-QKD

Based on the described scenario, we can formulate security assumptions under which the distributed key is secure. For the ease of reference, we list them as follows.

(i) The used system consists of two separated devices, the devices receive an input and respond with a well defined output, and the protocol is split into well defined rounds.

(ii) The devices do not send classical information to a possible eavesdropper.

(iii) Alice and Bob control when the devices communicate with each other.

(iv-a) Quantum theory is correct.

(iv-b) Each device is supplied with trusted inputs independent and unknown to a possible attacker.

(iv-c) Alice and Bob are connected via an authenticated channel, employ trusted local storage units, and use appropriate post processing.

Here, premises (i-iii) are specific for device-independent protocols, while (iv) are assumptions made in every QKD protocol.

3.3 Platforms for DI-QKD

Implementation of DI-QKD requires an experimental platform that distributes and analyses entanglement with high fidelity, detection efficiency, and rate, over distances that are relevant for cryptography. More specifically, a sufficiently entangled state in combination with appropriate measurement settings is required to violate a Bell inequality to test the proper function of the devices and to achieve a low QBER required for key generation. Exploiting detection-loopholes by a potential eavesdropper can be excluded with the high detection efficiency. With current technology it remains a major challenge to simultaneously achieve all conditions required for DI-QKD, however, recently, first proof-of-concept experiments have been reported [149–151].

Photons are the tool of choice to mediate the entanglement distribution, for example, by encoding a quantum state in polarization or time degree of freedom and guiding it to distant locations using optical fibres [152]. The rapid and inevitable loss of photons during propagation, however, results in an exponential decay of channel transmission efficiency over distance and potentially opens up the detection loophole. This sets a limitation on the fibre channel length of around 3.5 km due to attenuation losses as the total detection efficiency has to exceed $\sim$ 70% [153]. However, channel losses become irrelevant to the security of the DI-QKD protocol when the successful transmission of a photon can be signalled independently of the chosen measurement setting. Heralding the photon transmission allows for secure post-selection of the data for further processing while keeping the detection loophole closed. Experimentally, this can be implemented via, e.g., quantum non-demolition measurements for non-destructive detection of photonic qubits [154], photonic qubit amplification [155, 156], or event-ready entanglement generation schemes using quantum memories [157].

In view of DI-QKD, we can classify two main implementation approaches: (i) all-photonic implementation in which the qubits are encoded using photons only or (ii) memory-based implementation employing long-lived matter states to generate heralded entanglement—both approaches are facing distinct implementation challenges, which are discussed below.

All-photonic implementations

Entangled photon pairs enable to distribute entanglement to distant locations with high rate—commonly generated via spontaneous parametric down-conversion (SPDC) by pumping non-linear crystals at MHz rates [158], making them promising for cryptographic applications. Minimizing photon losses together with optimal measurement settings [159] enabled to violate Bell inequalities with entangled photon pairs while closing the detection loophole [160, 161] even over distances sufficient to simultaneously close the locality loophole [6, 7]. However, using SPDC sources and measuring pairs of two-mode squeezed vacuum states, photon emission statistics limit the CHSH value to $S < 2.31$ [162, 163]. Hence, photonic Bell-tests show only minimal Bell inequality violations.

Current experimental efforts aim, on the one hand, to minimize photon losses by increasing efficiencies of SPDC sources and single-photon detectors [151, 164–166]. Together with recent theoretical advances lowering the minimal required detection efficiency [148, 167–169], this could

allow for DI-QKD over up to 10 km of optical fibre ($\sim$ 2 dB attenuation loss), as will be discussed in Section 3.6. On the other hand, heralded photon amplifiers have been realised [170, 171] and non-destructive photonic qubit detection was demonstrated employing cavity-enhanced interactions with a single rubidium atom [154], which can overcome transmission losses and offer a promising road to all-photonic DI-QKD. So far, all-photonic heralding schemes have not been realised. For recent reviews of DI-QKD protocols and implementations we refer to [153] and [172].

Memory-based implementations

Quantum memories with light-matter interfaces enable one to generate heralded entanglement between distant locations and hence allow to close the detection loophole in a Bell-test regardless of photon transmission loss, as is realised in this thesis. For this, the memories first emit a photon to generate entanglement between light and matter or interact with incoming light in a state dependent manner. Two distant memories can then be entangled by using, for example, heralded storage of an entangled photon pair, entanglement swapping from two light-matter pairs, or enhanced light-matter interaction by resonators. Various quantum systems are under active research to facilitate the entanglement distribution, and heralded entanglement was generated for platforms including ions [173], atoms [55], and NV-centers [56]—even over distances and with readout speeds to simultaneously close the locality loophole via space-like separation [5, 8].

The current challenge for implementing memory-based DI-QKD is to distribute high-quality entangled states and, at the same time, to achieve entanglement rates over distances that are relevant for cryptography. Most demonstrations of heralded entanglement between distant quantum memories report fidelities relative to a maximally entangled state of up to 80% [55, 79, 96]—high enough to significantly violate a Bell inequality, but not sufficient for DI-QKD [174]. Recently, entanglement was generated between two distant ions with a fidelity of 96% [70, 150], which is the highest reported fidelity up to date and allows for DI-QKD. These fidelities are not fundamentally limited though, and could be increased by further reducing state generation or readout errors. Generation rates of high quality entangled states up to 100 Hz have been reported [58, 70, 175], while being orders of magnitude higher than first demonstrations, this is still limited for cryptographic applications. Moreover, achieving those rates could come at cost of a lower fidelity [58].

While the memory-based heralding schemes do not have a fundamental distance limitation, photon transmission losses and increasing communication times of the heralding signal do reduce the entanglement generation rate for larger distances, as is modelled for the system used in this work in Section 5.3. To minimize transmission losses and hence maximize entanglement generation rates using optical fibres, operation at telecom is indispensable. Recently, entanglement between quantum memories was distributed at telecom wavelength employing quantum frequency conversion [96, 176] or absorptive quantum memories [97, 177]. Finally, parallelization of the entanglement generation process can overcome these issues and allow for high-rate entanglement distribution over long distances.

3.4   Experimental implementation

A schematic of the system employed in our implementation is shown in Figure 3.2. Alice is located in Lab 1, while Bob is situated in Lab 2—approximately 400 meters apart (see Figure 2.2). Two entangled rubidium atoms form the quantum network link and are entangled using an entanglement swapping protocol, as described in detail in Chapter 2. In the follow-
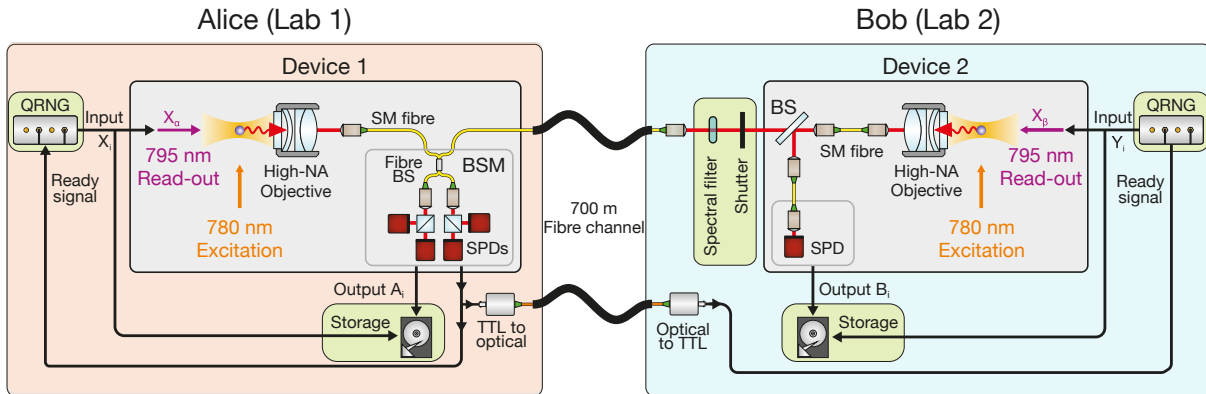
Figure 3.2: **Overview of the DI-QKD system.** Alice's equipment (Device 1 in Lab 1) is formed by a single-atom trap and a Bell-state measurement (BSM) set-up. Bob (Device 2 in Lab 2), uses a second single-atom trap together with a 90:10 (T:R) beamsplitter (BS) and a single photon detector (SPD). Each trap set-up contains of a high-NA objective to optically trap a single atom and collect atomic fluorescence into a single-mode (SM) fibre. The laboratories are 400 m apart and connected via a 700 m fibre channel. The atoms are entangled in an event-ready scheme by synchronously exciting them, after which the spontaneously emitted photons are collected by high-NA objectives and guided to the BSM. Here, a coincidental photon detection on two detectors in the same output arm of the fibre beamsplitter (BS) heralds the entangled atom-atom state $|\Psi^+\rangle$, which is announced to both users via a "ready" signal. After receiving the ready signal, two quantum random number generators (QRNG) select the inputs to the devices determining the polarisation of a readout pulse in a state-selective ionization scheme. Whether or not the atom was ionized yields the binary output of the devices which can be determined by fluorescence collection since ionised atoms are lost from the trap. The in- and outputs of each round are stored locally using a trusted storage. In Lab 2 a spectral filter and shutter are implemented to avoid leakage of the in- and outputs of the device via the quantum channel. Adapted from [149].

ing we discuss the experimental implementation, including the considered protocol based on a random key-basis, the quantum network link, and the implementation of the protocol.

3.4.1 Random key-basis protocol

The protocol considered was proposed by Schwonnek *et al.* (2020) [113]. It is similar to the standard DI-QKD protocol [38, 39], except that two measurement settings are used for key generation instead of one. Importantly, in doing so, the protocol can tolerate significantly more noise—the critical QBER is extended from 7.1% to 8.2%. Intuitively, the improved noise tolerance can be understood as follows. In the original protocols, it is assumed that Eve knows which setting is used for the key generation and adjusts her measurement settings accordingly. In the newly proposed protocol, Eve does not know which key setting is used in a particular round and hence, since the two key settings are orthogonal, she does not obtain maximal information about the key in approximately half of the rounds.

The protocol consists of N measurement rounds, whereby in each ith round both devices receive an input (X_i and Y_i) and respond with an output (A_i and B_i). More specifically, Alice's device accepts four different values $X_i \in \{0, 1, 2, 3\}$, while Bob's device has two inputs $Y_i \in \{0, 1\}$.

The input for each round is provided by a trusted local source of randomness. Both devices output two possible values, $A \in \{\uparrow, \downarrow\}$ at Alice's side and $B \in \{\uparrow, \downarrow\}$ at Bob's side. Additionally, the input and output values are recorded and stored in a local, secured storage.

After N rounds the users stop the measurements and begin with classical post-processing. For this, Alice and Bob reveal their inputs for each round over an authenticated public channel. For the rounds with differing input settings, i.e., $X \in \{2, 3\}$ together with $Y \in \{0, 1\}$, the outputs are shared over the public channel to compute the Clauser-Horne-Shimony-Holt (CHSH) [123] value using

$$S := E_{2,1} - E_{2,0} - E_{3,0} - E_{3,1}, \tag{3.1}$$

where the correlation functions are defined as

$$E_{X,Y} := \frac{N_{X,Y}^{A=B} - N_{X,Y}^{A \neq B}}{N_{X,Y}}. \tag{3.2}$$

Here, $N_{X,Y}$ is the number of rounds with input combination X, Y, while $N_{X,Y}^{A=B}$ ($N_{X,Y}^{A \neq B}$) is the number of rounds with identical (different) outcomes for input combination X, Y. Provided that the devices share a sufficiently entangled state, the Bell inequality can be violated, i.e., $S > 2$.

The raw data are sifted so that only the outputs of measurement rounds with identical input settings are kept for further processing. The QBERs for both key settings can be obtained via some error correction protocol and are denoted by

$$Q_0 := N_{0,0}^{A=B}/N_{0,0} \quad \text{for} \quad X_i = Y_i = 0 \text{ and}$$
$$Q_1 := N_{1,1}^{A=B}/N_{1,1} \quad \text{for} \quad X_i = Y_i = 1. \tag{3.3}$$

Note that the key pairs can be anti-correlated due to the use of anti-correlated entangled states. Both the QBERs (Q_0, Q_1) and the CHSH S-value are used to determine the amount of information about the sifted key that could have been obtained by an eavesdropper [178]. Next, by applying a technique known as leftover hashing, the eavesdroppers (quantum) information about the final key can be reduced to an arbitrary low level, defined by the security error of the protocol [179].

In this proof-of-concept experiment, we aim to estimate the asymptotic security performance of the considered DI-QKD protocol. For this purpose, we note that in the asymptotic limit and in case of a depolarising quantum channel, positive key rates can be achieved when the expected CHSH value satisfies $S > 2.362$ (or equivalently, $Q < 0.082$ with $Q_0 = Q_1 = Q$) [113].

3.4.2 Quantum network link

While the requirements for a DI-QKD implementation are less stringent with the newly proposed protocols, significant improvements of existing loophole-free Bell experiments are still required. To that end, we enhanced the entanglement generation rate, coherence of atomic states, and entanglement swapping fidelity of the loophole-free set-up reported in [8].

Two independently trapped single-atoms form the quantum network link. For this, Alice's equipment (Device 1) consist of a single-atom trap set-up in Lab 1, together with the Bell-state measurement set-up, laser set-up, and driver electronics. And Bob's equipment (Device 2) is formed by a single-atom trap in Lab 2, together with a single photon detector, laser set-up, and driver electronics.

Entanglement generation and analysis

The atoms are entangled in an event-ready scheme. The experimental sequence starts by loading both single-atom traps. Thereafter, the atoms are first prepared in the initial state $5^2\mathrm{S}_{1/2}\,|F=1, m_F=0\rangle$ via optical pumping and synchronously excited to the state $5^2\mathrm{P}_{3/2}\,|F=0, m_F=0\rangle$ to generate two pairs of atom-photon entanglement in the following spontaneous decays (Section 2.3.1). Next, the photons are coupled into single mode fibres which guide them to the BSM device in Lab 1. There, the photons are analysed in the H/V basis and hence a projection of the photons onto a $|\Psi^+\rangle$ state heralds the creation of the maximally entangled atom-atom state (Section 2.4.1)

$$|\Psi^+\rangle_{AB} = \frac{|\uparrow\rangle_{x,A}|\downarrow\rangle_{x,B} + |\downarrow\rangle_{x,A}|\uparrow\rangle_{x,B}}{\sqrt{2}}. \tag{3.4}$$

After a successful photonic projection, the two atomic qubits are independently analysed via state-selective ionisation, as detailed in Section 2.3.2 and illustrated in Figure 2.9. A particular state of the atomic qubit is ionised and leaves the trap depending on the polarisation $\chi = \cos(\gamma)V + e^{-i\phi}\sin(\gamma)H$ of a read-out laser pulse ($\gamma = \alpha$ for Alice's and $\gamma = \beta$ for Bob's device). If the atom is still in the trap, it is thus projected onto the state

$$|D\rangle = e^{i\phi}\cos(\gamma)\,|\uparrow\rangle_x - \sin(\gamma)\,|\downarrow\rangle_x := |\Uparrow\rangle. \tag{3.5}$$

The presence of the atom is then tested using fluorescence collection, which yields the final measurement outcome: $|\Uparrow\rangle$ when the atom is present and $|\Downarrow\rangle$ when there is no atom in the trap. On Alice's side, the single-photon detectors (SPDs) of the BSM detect the fluorescence of the atom, while on Bob's side an unbalanced beam splitter directs a small fraction of the fluorescence light onto a single SPD, as shown in Figure 3.2. Since the results are reported for every entanglement generation try, the detection efficiencies of Alice's and Bob's measurements are effectively one. Any component loss or ionization inefficiency contributes to the noise in the quantum channel, but does not open the detection loophole.

The experimental time sequence after a successful entanglement generation try is illustrated in Figure 3.3. The sequence starts by sending a "ready" signal to the devices after a successful entanglement generation event. In both devices, an electronic time delay allows for a state readout after a complete oscillation period of the trap frequency and Larmor precession (see Section 2.5). After this delay, two and one random bits are generated at Alice's and Bob's side, respectively, to select the measurement setting. Subsequently, the atomic states are analysed by a state-selective ionization scheme. The binary output of the devices is obtained by atomic fluorescence collection. To prevent leakage of the measurement outcome on Bob's side, a free-space shutter is closed to block the light and a 5 ms delay is implemented before the fluorescence readout (see Figure 3.2). Moreover, the trap is always emptied before reopening the shutter.

Improving the entanglement quality

To allow for positive key rates, the system needs to be improved with respect to the loophole-free Bell-test [8]. In particular, advancements were made in the fluorescence collection optics, the coherence and stability of the atomic qubit states, and the two-photon interference contrast, as detailed in Chapter 2.

The quality of the entangled atom-atom state is mainly improved by optimising the two photon interference of the BSM based on a rigorous analysis of the atom-photon entanglement generation process [102, 106], for more details see Section 2.4. Here, the multi-level structure
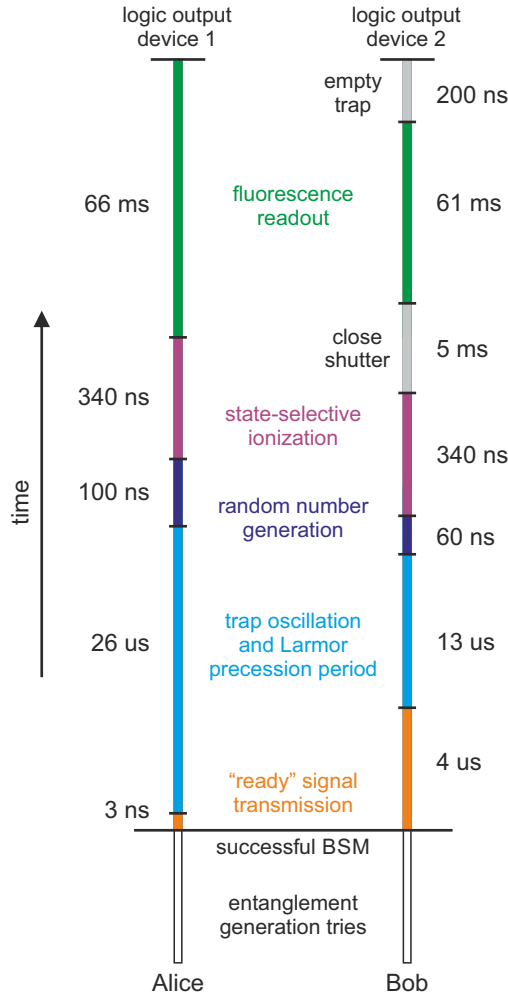
Figure 3.3: **Experimental sequence after a successful entanglement generation event.** The entanglement generation tries are repeated until successful. After a successful BSM the "ready" signal is transmitted to the devices and both atoms are individually analysed. The atoms are analysed at a delay of 26 μs and 17 μs relative to the respective excitation pulses in Alice's and Bob's set-ups, respectively. At Bob's side, a shutter is closed during the readout to prevent fluorescence light leaving the laboratory and the trap is always emptied before reopening the shutter. (Lengths not to scale.)

of ^{87}Rb, the finite duration of the excitation pulse, and experimental imperfections lead to the possibility of two photon emission from one atom. Crucially, these multi-photon events reduce the fidelity of the BSM result. To overcome this, only photons which are emitted after the end of the prior excitation pulse are accepted in the BSM, as shown in Figure 3.4. Accepting events conditioned on the photon detection times (750–845 ns) reduces the entanglement generation rate by a factor of 4. However, it significantly increases the two-photon interference contrast from $C_{\mathsf{intf}} = 0.875(5)$ to $0.991(5)$ and hence increases the fidelity of the generated entangled atom-atom state.

The expected atom-atom state visibility can be estimated as

$$V_{\mathsf{aa}} \geq V_{\mathsf{ap}_1} V_{\mathsf{ap}_2} C_{\mathsf{intf}} = 0.865, \tag{3.6}$$

where $V_{\mathsf{ap}_1} = 0.94$ and $V_{\mathsf{ap}_2} = 0.93$ represent the atom-photon state visibilities for Device 1 and 2, respectively, which are determined in test measurements presented in Section 2.3.2. Hence, we expect to observe $Q_0 = Q_1 = 0.067$ and $S = 2.45$, which lays within the positive key region of the random key-basis protocol and gives an asymptotic key rate of $r_\infty = 0.04$. Furthermore, according to Eq. (2.23), this results in an expected atom-atom state fidelity of $\mathcal{F}_{\mathsf{aa}} \geq 0.888$ relative to a maximally entangled state.

Entanglement generation rate

In the used experimental configuration the probability to generate atom-atom entanglement following an excitation pulse pair equals $\eta_{\mathsf{aa}} = 0.49 \times 10^{-6}$. This efficiency can be deduced from the individual atom-photon entanglement generation success probabilities as follows

$$\eta_{\mathsf{aa}} = \frac{1}{4} \eta_{\mathsf{ap}_1} \eta_{\mathsf{ap}_2} \eta_{\mathsf{tf}}, \tag{3.7}$$

where $\eta_{\mathsf{ap}_1} = 5.98 \times 10^{-3}$ and $\eta_{\mathsf{ap}_2} = 1.44 \times 10^{-3}$ equal the probabilities to detect a photon at the BSM set-up after an excitation attempt in Trap 1 and 2, respectively, and are determined via test measurements. Note that the lower photon detection probability for Bob's device is due to attenuation loss of approximately 50% in the 700 m optical fiber and the loss due to additional optical elements, including the beam splitter (90:10) for the local fluorescence detection and spectral filter shielding the read-out light, by another 50%, see Figure 3.2. The factor 1/4 originates from only accepting the state $|\Psi^+\rangle$, and $\eta_{\mathsf{tf}} = 0.27$ represent the fraction of accepted events in the specified time-window.

The duty cycle of the experiment is approximately half, which is mainly limited by the fraction of time that an atom is present in both traps. Together with a repetition rate of the entanglement generation tries of 52 kHz, limited by the cooling periods of the atoms and the communication times between the single-atom traps and the BSM, this results in an overall event rate of $1/82$ s^{-1}.

Stability system

Due to the relatively low event rate, it is required to run the system for several days to make confident statements about its performance, which makes the stability of the DI-QKD system crucial. Therefore, many parameters in both atom trap set-ups are actively stabilized or automatically optimized. In addition, daily maintenance shifts are required to optimize, among others, laser frequency locks, laser pulse powers, magnetic fields, and polarization drifts in fibres. The measurement run presented in this chapter was paused six times for scheduled maintenance.
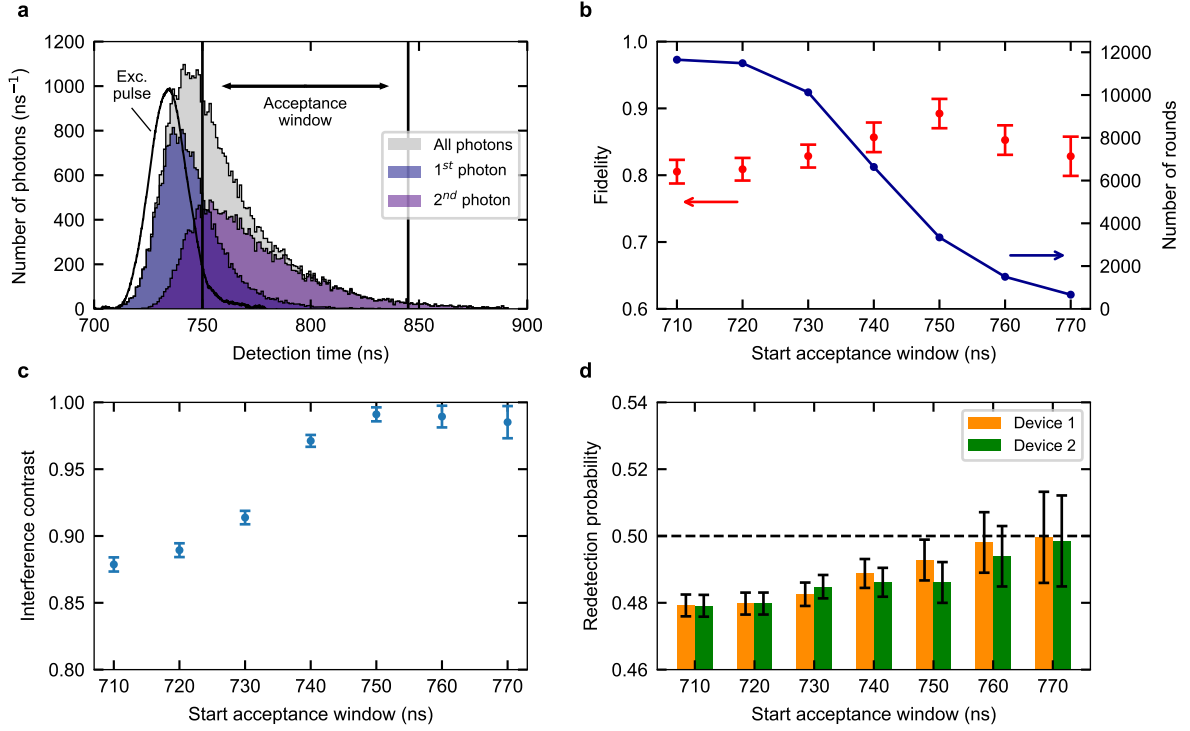
Figure 3.4: **Photon detection times and entanglement quality.** **a**, Histogram of the photon detection times for all recorded two-photon events. The 'All photons' histogram equals to the sum of the 1st and 2nd photon histograms. Note that 1st and 2nd indicate the relative timing of the two photons and do not note the origin of the photons—after all, the photons are indistinguishable. The two-photon acceptance window is set to 750–845 ns, accepting around 27% of the two-photon events. The detection time is relative to a trigger signal provided by the control electronics of the experiment. The position of the excitation pulse compared to the detected photons represents the timing during the emission and not the detection process. **b**, Number of accepted rounds and atom-atom state fidelity for varying start times of the acceptance window; the end time of the window is fixed at 845 ns. **c**, Interference contrast for varying start times of the acceptance window. The interference contrast increases from 0.875(5) to 0.991(5) for the chosen start acceptance window of 750 ns, improving the observed atom-atom state fidelity significantly. **d**, Redetection probability of an atom after a readout attempt for Device 1 and 2. Ideal devices have a redetection probability of 1/2, which is indicated by the dashed horizontal line.

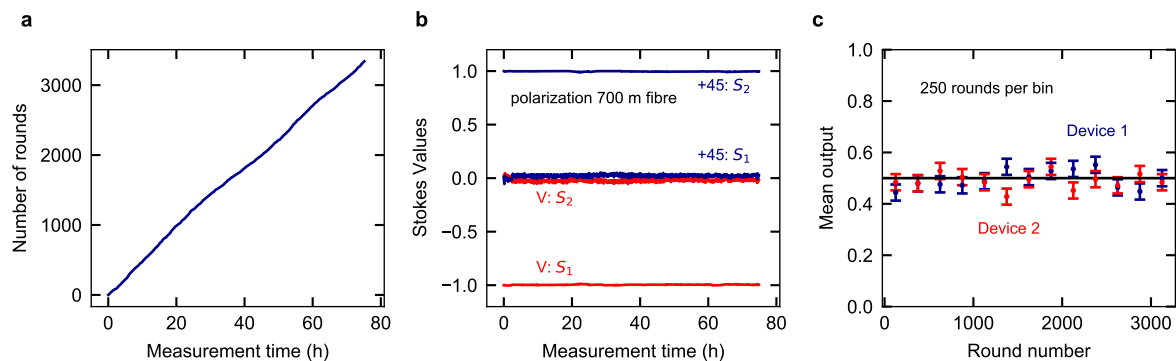Figure 3.5: **Stability DI-QKD system. a**, The number of measurement rounds completed over time. **b**, The polarization drifts in the 700 m long fibre channel. **c**, The mean output of the individual devices binned per 250 rounds.

Here we assess the stability of the system by observing three parameters: the event rate, polarization drifts in the 700 m long fibre, and the individual device outputs, as illustrated in Figure 3.5. First, the event rate of the system over the complete measurement run is analysed by observing the number of completed rounds over time; the almost linear behaviour indicates a stable event rate (see Figure 3.5a). The event rate can fluctuate slightly by changes in ratio of time that an atom is present in both single-atom traps and drifts in efficiency of the entanglement generation process; both influenced by laser pulse power fluctuations. Next, we analyse the polarization changes in the 700 m long fibre, which is automatically compensated for every 3–5 minutes (see Figure 3.5b). For this, we measure, before every optimization run, the Stokes vector of a classical laser beam at the output of the long fibre, where the input to the long fibre was V or $+45$ polarized. We observe polarization drifts in the 700 m long fibre of $< 0.5\%$. The optimization is based on a gradient decent algorithm whereby the polarization is controlled with a fibre polarization controller [122]. Finally, the individual outputs of the devices are analysed over time (see Figure 3.5c). For this, we bin the device outputs per 250 rounds and calculate the mean output where the device output $\uparrow$ ($\downarrow$) corresponds to the value $1(0)$. Following this method, ideal devices have a mean output of 0.5. For our system, a reduced atom-photon entanglement fidelity would result in a lower mean output, which is however not observed.

3.4.3 Implementation protocol

Measurement settings

Based on the generated entangled state (Eq. (3.4)) and the atomic state measurement scheme (Eq. (3.5)), the input values $X \in \{0, 1, 2, 3\}$ convert to measurement angles $\alpha \in \{-22.5°, 22.5°, -45°, 0°\}$ for Alice's device and $Y \in \{0, 1\}$ translate to $\beta \in \{22.5°, -22.5°\}$ for Bob's device, respectively. The capability of fast switching between various read-out settings is achieved by overlapping multiple read-out beams with different polarisation and individually controllable intensities [8].

Realization of secure locations

Unauthorised incoming and outgoing communication of the laboratories can be mitigated with various steps. Especially on Bob's side, extra measures are taken to prevent information leakage from the laboratory: a free-space shutter is closed during the read-out process to prevent fluorescence light from leaking into the optical fibre to prevent leakage of the device output to the outside environment (see Figure 3.2). Furthermore, the trap is always emptied before reopening the shutter. Due to the approximate 5 ms reaction time of the shutter, a spectral filter (10^{-6} transmission at 795 nm) is deployed to block the read-out pulse after interacting with the atom and hence preventing unintentional transmission of the read-out setting. Without spectral filtering, approximately 5% of the few microwatt readout pulse power is coupled into the fibre leaving the laboratory. To prevent leakage up to the single photon level, an additional spectral filter (or two) might prove useful. For Alice's side, such countermeasures are not needed as the BSM set-up already serves as a natural filter [180].

Locality loophole

The readout processes of the atomic quantum states are not space-like separated during this experiment. The security of a DI-QKD protocol is not increased by closing the locality loophole via space-like separation [39]. Instead, by enforcing that the devices do not leak information, which is assumed in the security proof under assumptions (ii) and (iii), the process generating the output in one device is already independent of the input and the process of the other device— which closes the locality loophole for DI-QKD [39, 147]. Hence, imposing that no information leaks out of a closed environment around the users—in our case the two laboratories—assures that the measurement outcomes of both devices cannot influence each other. Therefore, not being space-like separated, does not open up possibilities for Eve to gain more information about the key.

In principle, it is possible to achieve space-like separation of the measurements outcomes with the employed set-up, as was achieved during the loophole-free Bell-test reported in [8]. For this, the atomic readout times in Device 1 and 2 need to be matched by tuning the optical dipole trap depths and magnetic field strengths. Furthermore, to complete the fast ionization based state readout ($< 1\mu$s), channel electron multipliers (CEMs) can directly detect the ion and electron fragments; making the slow (~ 60 ms) fluorescence collection redundant. For stability reasons, we decided not to use the CEMs during the proof-of-concept DI-QKD experiment, but use the simpler fluorescence readout instead.

Random inputs, outputs, and local storage

The independent random inputs to the devices (requirement iv-b) are provided by independent quantum random number generators (QRNG) [8, 181] located in each laboratory. At Alice's side, two random bits are used to select the input, while at Bob's side only one random bit is used, leading to uniformly distributed input combination choices. The outputs $A, B \in \{\uparrow, \downarrow\}$ are derived from the fluorescence counts after the state-selective ionisation. Finally, the users' inputs and outcomes are stored in two independent, trusted secure storages (requirement iv-c).

Table 3.1: **Summary of in- and output measurement correlations.** Number of rounds for each of the eight input setting combinations and the number of rounds the devices responded with (anti-)correlated outputs.

number of rounds per setting $N_{X,Y}$				
	X=0	X=1	X=2	X=3
Y=0	448	425	389	434
Y=1	408	412	403	423
with correlated outputs $N_{X,Y}^{A=B}$				
	X = 0	X = 1	X = 2	X = 3
Y = 0	35	205	78	73
Y = 1	198	32	326	64
with anti-correlated outputs $N_{X,Y}^{A \neq B}$				
	X = 0	X = 1	X = 2	X = 3
Y = 0	413	220	311	361
Y = 1	210	380	77	359

3.5 Results

The inputs and outputs of the devices were recorded for $N = 3\,342$ rounds over a measurement period of 75 h. The results are summarized in Table 3.1, listing the total number of rounds per input setting combination $N_{X,Y}$ and the number of correlated outputs $N_{X,Y}^{A=B}$ and anti-correlated outputs $N_{X,Y}^{A \neq B}$. The resulting output (anti-)correlation probabilities for the eight different input combinations, i.e. $N_{X,Y}^{A=B}/N_{X,Y}$ and $N_{X,Y}^{A \neq B}/N_{X,Y}$, are visualized in Figure 3.6.

3.5.1 Performance quantum network link

It is instructive to first review the performance of the quantum network link independently of the DI-QKD protocol.

Atom-atom state fidelity

The figure of merit to evaluate the performance of the quantum network link is the fidelity of the observed entangled atom-atom state relative to a maximally entangled state, determined according to the methods described in Section 2.4. Fitting the measurement data (Figure 3.6) with sinusoidal functions gives estimated visibilities for input combinations $X = 2, 0, 3, 1$ and $Y = 0$ (respectively $X = 2, 0, 3, 1$ and $Y = 1$) of 0.869(25) (respectively 0.888(45)). Then, averaging the found visibilities and taking into account that a third atomic ground level spin
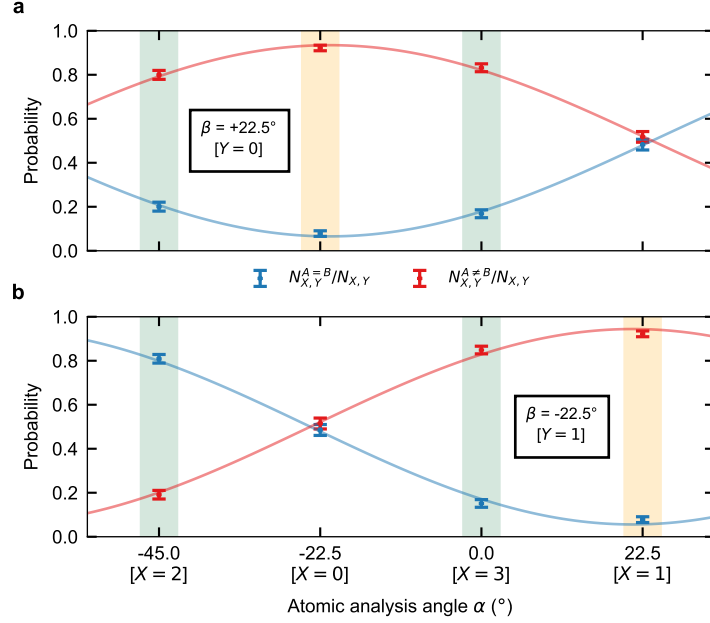
Figure 3.6: **Observed atom-atom state correlations. a,b,** The correlation (blue) and anti-correlation (red) probabilities of the device outputs for the eight input combinations. The settings with the green (yellow) background contribute to the evaluation of the S-value (QBER). The data are fitted with sinusoidal functions estimating visibilities of $0.869(25)$ (**a**) and $0.888(45)$ (**b**).

state can be populated, a lower bound on the fidelity is found using Eq. (2.23) resulting in $\mathcal{F} \geq 0.892(19)$. Note that the observed fidelity agrees with the expected fidelity deduced from the atom-photon entanglement visibilities from the individual devices in combination with the two-photon interference contrast.

3.5.2 Secret key rate

To analyse the performance of the protocol we first concentrate on the achieved asymptotic secret key rate, which is deduced from the observed S-value and QBER, as visualised in Figure 3.7. The CHSH value is found to be $S = 2.578(75)$ using Eq. (3.1) with

$$
\begin{aligned}
E_{2,0} &= -0.599(41), \\
E_{3,0} &= -0.664(36), \\
E_{2,1} &= 0.618(39), \text{ and} \\
E_{3,1} &= -0.697(35).
\end{aligned}
\tag{3.8}
$$

The QBERs are given by the correlation data for $X = Y$, using Eq. (3.3) we find

$$
\begin{aligned}
Q_0 &= 0.078(13) \text{ and} \\
Q_1 &= 0.078(13),
\end{aligned}
\tag{3.9}
$$

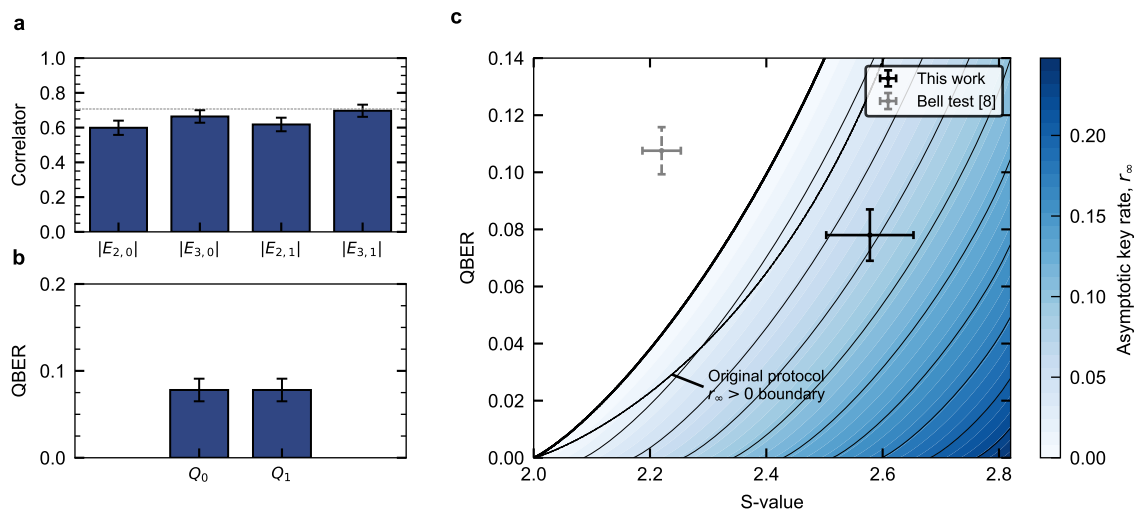Figure 3.7: **Achieved asymptotic key rate. a,** Observed CHSH correlators (Eq. (3.1)). The correlator values for an ideal system are indicated with the dashed line. **b,** Observed QBERs for the two key-bases. **c,** Asymptotic secret key rate for varying CHSH S-value and QBER for the robust DIKQD protocol [113]. This work shows an expected secret key rate of 0.07 and lies well inside the positive region. For comparison, the result of the loophole-free Bell test [8], where the QBER was not measured but estimated assuming depolarizing channel noise. The $r_\infty > 0$ boundary of the original protocol [38, 39] is indicated with the black dotted line.

which gives an average error rate of $Q_{avg} = 0.078(9)$. For the considered DI-QKD protocol, the observed S value and QBER result in a secret key rate of $r_\infty = 0.07$ in the asymptotic limit (Figure 3.7). Note that the maximal achievable key rate for the implemented protocol with uniformly distributed measurement settings, as used here, equals 0.25. For the generation of finite keys, the key rate can be improved by adjusting the input setting distributions. For example, by increasing the relative probabilities of measuring the QBER settings or measuring just one key-basis when the entanglement quality is high enough.

For comparison, the original DI-QKD protocol zero-key boundary is shown in Figure 3.7. The observed S and Q_0 (or Q_1) also result in positive key rates for this protocol—even with a higher asymptotic key rate. However, taking into account the statistical errors of the observed parameters, a less significant claim of achieving positive asymptotic key rates can be made for the original protocol.

To investigate the possibility to distribute finite keys with the system, we employ state-of-the-art finite-key analysis for the protocol [179]. In the simulation, we consider collective attacks, an error correction efficiency of 1.15, and uniformly distributed measurement settings for Alice and Bob. We find that, given the observed S and Q, $\epsilon_{\text{DI}} = 10^{-5}$ security can be obtained with a minimal block length of 1.75×10^5, as shown in Figure 3.8. Here, ϵ_{DI} is the security error of the protocol and can be seen as the probability that the protocol fails in its task, e.g., that the key pair is not secret.
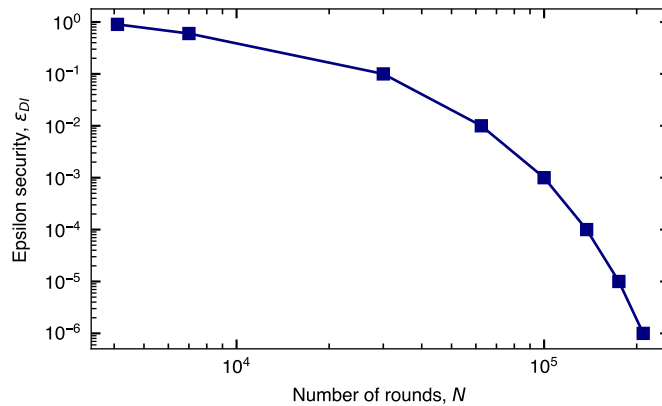
Figure 3.8: **Finite-key simulation for the robust DI-QKD protocol.** Shown is the minimum number of rounds required to distribute a finite-key with a certain epsilon security, considering collective attacks and uniformly distributed measurement settings. The channel parameters S, Q_0, and Q_1, are set to the observed values in the experiment. A non-asymptotic security of $\epsilon_{\mathrm{DI}} = 10^{-5}$ is considered to be realistic for cryptography applications. Taken from [149], employing the methods presented in [179].
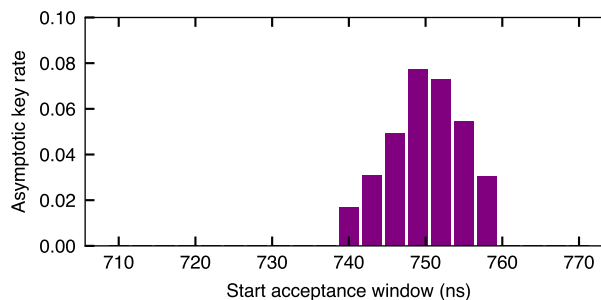
Figure 3.9: **Asymptotic key rate for different detection time conditioning of the BSM.** The start of the acceptance window is varied resulting in different asymptotic key rates for the random key-bases protocol.

Influence of time-filtering on key rate

It is insightful to evaluate the achieved asymptotic key rate for varying two-photon coincidence acceptance windows. Figure 3.9 shows the asymptotic key rate for different start times of the acceptance window, while keeping the end of the acceptance window fixed at 845 ns. The analysis shows that timefiltering is necessary to reach the positive key region. For future finite-key implementations, filter conditions should optimize the achieved key distribution rate—and not the asymptotic key rate, i.e., taking into account both the percentage of accepted events and the key rate per event.

3.5.3 Statistical analysis

A rigorous security analysis of practical DI-QKD requires a finite-key analysis that takes into account the resources consumed and block-length considerations [179]. However, the presented system has an intrinsic limitation on the event rate based on state-of-the-art technology; collect-

ing sufficient data for such a security analysis would take months. Consequently, to evaluate the reliability of the achieved positive key rate claim, we analyse the collected data using standard Bayesian methods and confidence intervals.

Bayesian analysis

We estimate the expected secret key rate of the DI-QKD experiment using standard Bayesian analysis; while we acknowledge that this is not the usual approach for QKD, it nevertheless gives a reliable estimate based on available data. In this analysis, we assume that underlying input-output probability distributions are independent and identically distributed and use standard Bayesian methods to determine the uncertainties of the estimated parameters.

Starting from the data summary listed in Table 3.1, we model the random behaviour of S (its winning probability), Q_0, Q_1, and Q_{avg} using Beta random variables, β_{win}, β_{Q_0}, β_{Q_1}, and $\beta_{Q_{\mathsf{avg}}}$, respectively, which is in line with the self-testing statistical analysis reported in [182]. In particular, starting with a uniform prior, the (updated) posterior distributions are

$$
\begin{aligned}
\beta_{\mathsf{win}} &= \mathrm{Beta}(N_{2,0}^{A\neq B} + N_{3,0}^{A\neq B} + N_{2,1}^{A=B} + N_{3,1}^{A\neq B} + 1, N_{2,0}^{A=B} + N_{3,0}^{A=B} + N_{2,1}^{A\neq B} + N_{3,1}^{A=B} + 1) \\
&= \mathrm{Beta}(1357 + 1, 292 + 1), \\
\beta_{Q_0} &= \mathrm{Beta}(N_{0,0}^{A=B} + 1, N_{0,0}^{A\neq B} + 1) \\
&= \mathrm{Beta}(35 + 1, 413 + 1), \\
\beta_{Q_1} &= \mathrm{Beta}(N_{1,1}^{A=B} + 1, N_{1,1}^{A\neq B} + 1) \\
&= \mathrm{Beta}(32 + 1, 380 + 1), \text{ and} \\
\beta_{Q_{\mathsf{avg}}} &= \mathrm{Beta}(N_{0,0}^{A=B} + N_{1,1}^{A=B} + 1, N_{0,0}^{A\neq B} + N_{1,1}^{A\neq B} + 1) \\
&= \mathrm{Beta}(67 + 1, 793 + 1)
\end{aligned}
$$

(3.10)

where $\mathrm{Beta}(a, b)$ is the standard Beta distribution, and the winning probability is related to the CHSH value by $P_{\mathsf{win}} = (S + 4)/8$. The probability density functions (PDF) are visualised in Figure 3.10a and b.

To calculate the worst-case estimate of the expected secret key rate, we fix the tail errors of the updated Beta distributions to $\alpha = 0.03$; corresponding to a 97% probability that each of the individual parameters is higher (or lower) than a certain critical threshold. More specifically, we find $S \geq 2.4256$ and $Q_0 = Q_1 \leq 0.107$. Finally, using uniform settings (as was done in our experiment), we find that these critical values still provide a positive key rate.

Two dimensional confidence level intervals

Fixing the tail errors of the individual parameters, as used above, results in conservative parameter estimation. Since the measurements contributing to the S-value and QBERs originate from independent data sets, the statistical errors in the measurements are uncorrelated. Therefore, the probability that simultaneously $S < 2.4256$, $Q_0 > 0.107$, and $Q_1 > 0.107$ is of the order of α^3. Note that all parameters depend on the entanglement quality, and hence a drift of the
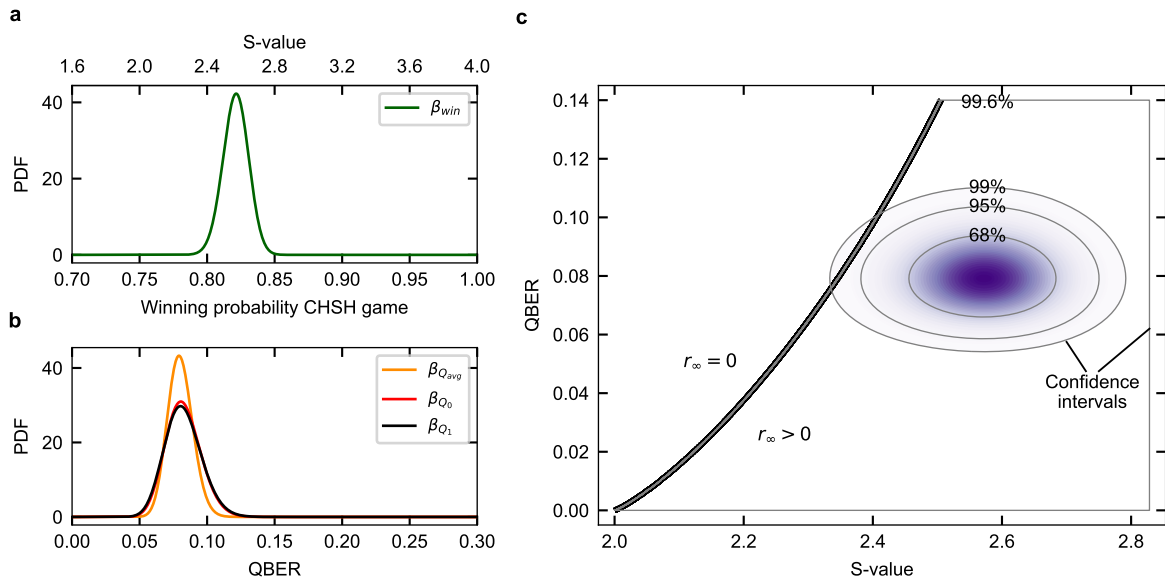
Figure 3.10: **Probability density functions of the Beta random variables. a,b,** One dimensional probability density functions (PDF) of the winning probability of the CHSH game β_{win} and the QBERs Q_0, Q_1, and Q_{avg} modelled as Beta distribution in one dimension according to Eq. (3.10). **c,** Two dimensional PDF for β_{win} and $\beta_{Q_{\mathsf{avg}}}$, assuming that the statistical errors of these parameters are uncorrelated. The gray lines indicate confidence level intervals. The black line indicates the zero-key boundary, only on the right side of the line the asymptotic key rate is positive ($r_\infty > 0$). A confidence interval of 99.6% covers the complete positive key rate region.

entanglement quality would cause a correlated change of all parameters. However, for this analysis, we are interested in the statistical errors of the measurements, which must be uncorrelated for independent measurement sets of quantum states.

A more accurate estimation of a positive asymptotic key rate certainty is made by using two dimensional PDFs, as shown in Figure 3.10c. Shown is the two dimensional PDF for β_{win} and $\beta_{Q_{\text{avg}}}$, including elliptical confidence intervals of 68%, 95%, and 99%, and a confidence interval that spans the complete positive key rate region of 99.6%. In analogy to the one dimensional tail errors, now parameters obtained from a two dimensional tail error of 0.4% would still result in positive asymptotic key rates. Hence, also for the limited number of events, we can claim with 99.6% confidence that the presented system allows for quantum key distribution between two users 400 m apart in a fully device-independent setting.

3.6 Other DI-QKD experiments

In this section, we discuss the results presented in this work with respect to two simultaneously conducted proof-of-concept DI-QKD experiments, one based on entangled photons in Hefei [151] and another based on trapped ions in Oxford [150].

All-photonic experiment

In the Hefei experiment, entanglement is distributed using polarisation-entangled photon pairs at 1560 nm created in a periodically poled potassium titanyl phosphate (PPKTP) crystal. The photons are sent to Alice and Bob in free-space where their polarisation is projected using a pre-set measurement angle by a HWP and QWP together with a PBS. After projection, the photons are coupled into optical fibres with a total length of 220 m. Finally, the photons are detected using SNSPDs with a total detection efficiency of 87.5%.

A total of 2.4×10^8 entanglement generation rounds were executed, while achieving an expected asymptotic key rate of $r_\infty = 2.33 \times 10^{-4}$. The positive asymptotic key rate was enabled by (i) employing the post-selection technique of [169] and (ii) various experimental simplifications. The former, surprisingly, lowers the minimum detection efficiency required for positive key rates to 68.5% only. However, this technique relies on the collective attack model in a fundamental way [183] and hence might not be secure in the fully DI setting against general adversaries. Regarding the experimental simplifications, the measurement settings were not randomly changed from round to round in the experiment, but rather waveplates were set manually to determine all the correlators for evaluating S. In addition, aiming to simulate longer distances, optical fibres on spools were placed behind the state analysis to avoid the otherwise required stabilisation of the polarization. Furthermore, there was no fibre connection between the entanglement source and the users.

In summary, despite the progress in this experiment, an all-photonic implementation delivering a positive finite key length may still require further technological improvements. Moreover, realisation of all-photonic heralding schemes is also a must to overcome the distance limitation due to attenuation in optical fibres.

Ion-based experiment

In the Oxford experiment, entanglement is generated between single $^{88}\text{Sr}^+$ ions, which are trapped in individual ion traps positioned at opposite sides of an optical table at a distance of 2 m. Other than the trapping techniques, the concepts used to distribute entanglement are very

Table 3.2: **Performance of the quantum links.** Key parameters that characterize the quantum link performance employed in the proof-of-concept DI-QKD experiments.

	Oxford [150]	Munich
Fidelity	0.960(1)	0.892(23)
Rate (s^{-1})	100	1/82
Fibre length (m)	3.5	700
Line-of-sight separation (m)	2	400

similar to the methods presented in this work. First, each of the ion spin states is entangled in a spontaneous decay with the polarization of the emitted photon. The two photons are guided with 1.75 m long single-mode fibres to a Bell-state measurement device where a joint measurement on the photons heralds the entanglement between the ions. The quantum state of the ions is measured after every heralding signal, i.e., with unit detection efficiency, thereby closing the detection loophole for the Bell-test.

Performance parameters of the Oxford quantum link are listed in Table 3.2, together with the parameters achieved in this work. The rate at which the links generate entanglement critically depends on the success probability of the entanglement generation tries and their repetition rate. The former is mainly limited by the efficiency to collect photons emitted by the memories, which are typically up to a few percent using free-space optics, as is used in both experiments. Together with photon transmission and detection losses, the heralding probability for ion-ion entanglement equals 1.6×10^{-4}. This is a factor 320 higher than the success probability achieved in our experiment, which is explained by various aspects of the Munich experiment, including the time filtering requirement (factor 4), attenuation in the 700 m long fibre (factor 2), acceptance of one Bell-state (factor 2), additional measures to prevent leakage at Bob's side (factor 2), and lower fluorescence collection efficiency (factor 10)[1]. The repetition rate, on the other hand, is limited by the two-way communication time between the trap set-ups and Bell-state measurement device, since, in event-ready schemes, the entanglement attempts can only be repeated after receiving the result of the previous try—thus introducing a trade-off between distance and rate. In the Oxford experiment an attempt rate of 1 MHz is achieved. The observed ion-ion state fidelity of 0.960(1) is the highest reported so far for distant quantum memories and allows for positive key rates in DI-QKD protocols.

Closing the locality loophole in context of DI-QKD can be realised by securing the user locations, in particular, by enforcing that no information about the in- and outputs of the devices leaks to the outside environment. The generation of entanglement, on the other hand, requires the photonic channel, i.e., a connection between the quantum memories, and hence opens a back door to the outside environment. Therefore, after distributing the entanglement, this link should be disconnected—as is described for the Munich experiment in Section 3.4.3. In the Oxford experiment, the ions are moved out of the focus of the optics and hence prevent fluorescence from coupling into the fibre leaving the laboratory. Moreover, before repositioning

---

[1]The probability to detect a spontaneously decayed photon including a short fibre (< 5 m) is about 2% and 0.6% for the Oxford and Munich experiment, respectively.

the ions, the internal states are scrambled to avoid information leakage to the environment when reconnecting the quantum link.

The performance of the ion-based DI-QKD system was evaluated by generating a secret key shared by Alice and Bob. For this, a protocol was implemented including error correction, authentication, key activation, and privacy amplification. A total of 1.5×10^6 entanglement generation and analysis rounds were executed during a period of 7.9 h, achieving a CHSH value of $S = 2.677(6)$ and QBER of $Q = 0.0144(2)$. The protocol generated 95 884 secret shared bits, resulting in a key rate of 0.064. Other steps in the protocol consumed 256 secret bits, hence the number of secret bits shared by Alice and Bob was extended by 95 628.

The single photons used for the entanglement distribution process have a wavelength of 422 nm, resulting in attenuation loss of a factor two for every 100 m optical fibre, and hence limits the maximum achievable fibre link length. To achieve entanglement distribution over longer distances in future experiments, it is required to convert the frequency of the photons. Recently, conversion of light at 422 nm to the telecom regime was achieved in a first demonstration set-up [184]. For photons emitted by rubidium atoms at 780 nm, on the other hand, full polarization-preserving quantum frequency conversion to telecom wavelength was demonstrated, as will be presented in Chapter 4 and 5 of this thesis.

3.7 Discussion and outlook

In this chapter we presented a proof-of-concept DI-QKD system by demonstrating a quantum network link that achieves positive asymptotic secret key rates between users separated by 400 m line-of-sight (700 m fibre length) in a fully device-independent setting. While the current system improves upon existing loophole-free Bell set-ups, there are still several areas that require enhancements before a DI-QKD experiment with finite-key security and longer reach can be achieved. For one, a significantly higher event rate is required to obtain finite-key security within a practical time-frame; based on the current set-up and over the current distance, one would need months of measurement time to achieve finite-key security. For a practical demonstration of DI-QKD, the employed apparatus should:

1. Show an entanglement quality enabling for a positive key rate.

2. Realise entanglement distribution over distances relevant for cryptography.

3. Achieve entanglement rates allowing for key distribution on practical timescales.

Currently, the system generates a high-quality atom-atom entanglement event every 82 s over a distance of 400 m. Hence, requirement (1.) could be improved and requirement (3.) is not yet fulfilled. Therefore, next steps involve improving the entanglement generation rate and reach of the quantum network link.

Towards finite-key security

Achieving finite-key security requires a significantly higher event rate—critically depending on the entanglement generation efficiency and the repetition rate. Three realistic improvements on the current set-up can increase the former by an order of magnitude. First, preparing more than one entangled state in the swapping process, here the $|\Psi^-\rangle$ state. This is already possible with the current set-up, but its quality needs to be improved. Second, using superconducting

nanowire single-photon detectors with quantum detection efficiencies of $> 90\%$, which could quadruple the entanglement generation rate. Finally, improving the atom-photon entanglement generation quality and hence reducing the requirement of temporal filtering in the BSM, for more details see Section 2.4 and [106].

Event-ready schemes, as employed in the experiment presented here, have an intrinsic limitation on the achievable entanglement generation rate: a repetition of the entanglement generation process is only possible after waiting for a feedback signal from the BSM. Therefore, the repetition rate is limited by the communication times between the two devices and the BSM. Consequently, there is a trade-off between the event rate and distance—see Section 5.3 for a detailed analysis—and one would have to prioritise distance over finite-key security (or vice versa). Parallelizing the entanglement generation process can overcome this issue. Neutral optically trapped atoms are an ideal candidate to scale up the number of individually controllable atom traps and hence enable for temporal multiplexing of the entanglement generation process. We further detail on parallelization of the entanglement generation process and single-atom based quantum networks in the outlook of this thesis in Chapter 6.

Towards longer distances

Another direction of improvement is the reach of the quantum network link. Here, one of the limiting factors is attenuation loss of the 780 nm wavelength photons in long optical fibres, which equals 50% for a 700 m long link only. To overcome losses in longer fibre links, one can convert the entangled single photons to the low-loss telecom band via polarisation-preserving quantum frequency conversion, which is subject to Chapters 4 and 5 of this thesis.

Conclusion

In summary, our results represent a major step towards the goal of ultimate secure communication based solely on quantum physics. Importantly, they indicate that state-of-the-art quantum network links are capable of harnessing the ultimate quantum advantage for secure communications. Even if it is still a long way to go; when the future quantum repeater based quantum networks provide the key resource, i.e., shared entanglement, DI-QKD–as realized in this proof-of-concept experiment–will become the standard for secure key exchange.

Chapter 4

Atom-Photon Entanglement Distribution at Telecom Wavelength

In this chapter we report on the generation and observation of entanglement between a single ^{87}Rb atom and a photon at telecom wavelength after propagation through long fibre links. The experimental scheme starts by entangling the spin state of an atom with the polarisation state of a single photon emitted at 780 nm. Subsequently, the wavelength of the photon is transferred to the telecom S-band at 1522 nm by difference frequency generation (DFG) in a waveguide crystal through mixing of the photons with a pump field at 1600 nm. After conversion, the photons propagate through fibres on spools with lengths up to 20 km. Finally, the entangled atom-photon state is analysed by measuring correlations in two bases. Furthermore, we analyse the applicability of this scheme for atom-photon and atom-atom entanglement distribution over fibre link lengths up to 100 km. Work presented in this chapter resulted in the publication Van Leent *et al. Physical Review Letters* **124**, 010510 (2020), and some parts of the text are based on this publication.

The experiments presented here were performed in collaboration with researchers from the University of Saarland—most notably by designing and constructing the quantum frequency conversion (QFC) system. For a detailed description of the QFC system, we refer to Chapter 6 of [185].

This chapter is organised as follows. We start by introducing the topic of long-distance entanglement distribution with the emphasis on the role of QFC in Section 4.1. Section 4.2 describes the physical model of the conversion process and the design criteria for the realization of high-efficient, low-noise, and polarisation-preserving QFC devices. Next, in Section 4.3, the employed QFC system is described, after which, in Section 4.4, we detail the used experimental set-up and sequence. Section 4.5 presents the experimental results of atom-photon entanglement distribution over up to 20 km telecom fibre, which are extrapolated to distances up to 100 km for atom-photon and atom-atom entanglement distribution. The chapter concludes with a discussion and outlook in Section 4.6.

4.1   Introduction

For long-distance optical communication over fibres, it is indispensable to operate at telecom wavelengths. At these wavelengths, attenuation losses in the fibre links are minimized and signals can be efficiently distributed over hundreds of kilometres. Equivalently, for photon mediated entanglement distribution via long optical fibres, it is thus crucial to employ telecom
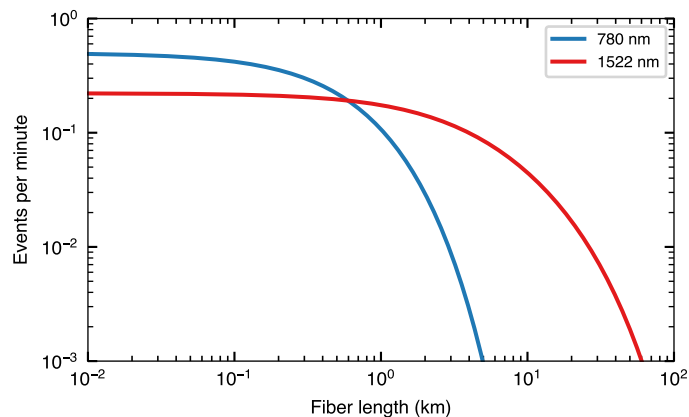
Figure 4.1: **Expected atom-atom entanglement generation rate.** Atom-atom entanglement generation rate for photons at a wavelength of 780 nm (blue) and 1522 nm (red) for varying fibre length. The event rate decreases for increasing fibre lengths due to the longer communication times and the higher attenuation losses in the fibres. In the analysis we assume a middle station with equal fibre lengths to the two nodes.

wavelength photons. Most physical candidates to serve in quantum nodes, however, operate in the visible or near infrared regime, which would limit distribution lengths via optical fibres to a few kilometres[1].

By coherently transferring the photons to telecom wavelengths via QFC devices [90–93], attenuation in fibres is minimized and existing telecommunication infrastructure can be used to cost-effectively realize quantum network links. To serve as efficient telecom quantum interface, however, the demands on the QFC devices are high. They should: (i) allow for high conversion efficiency, (ii) introduce minimal noise around the target wavelength, and, for polarisation encoded qubits, (iii) preserve the polarisation state of the photons. Individually, these properties were demonstrated in the last decades, e.g., for polarisation-preserving QFC [188–190], but only recently devices were constructed that fulfilled all the requirements [94, 95]; achieving polarisation-preserving conversion with low noise and external-device efficiencies of around 30%.

In the last years these concepts were used to demonstrate entanglement between various quantum emitters and photons at telecom wavelength, including atomic ensembles [94, 96, 191, 192], trapped ions [95, 193], NV centers [194]. However, for neutral single-atoms, distribution of entanglement at telecom wavelengths was so far not yet demonstrated.

The atom-photon entanglement generation process employed in this work creates photons at a wavelength of 780 nm (see Section 2.3). At this wavelength—suffering an attenuation of about 4 dB/km—the photon loss equals a factor 100 for propagation through every 5 km of optical fibre. Figure 4.1 shows the expected atom-atom entanglement generation rate using photons at a wavelength of 780 nm and 1522 nm as function of fibre length. Employing QFC to telecom wavelength for both single-atom traps can increase the reach of the quantum network link presented in Chapter 2 by more than one order of magnitude. This makes quantum frequency conversion to telecom wavelengths crucial to realise fibre based city-to-city scale quantum network links.

---

[1]Note that there are a few quantum systems with transitions in the telecom, such as Erbium doped crystals [186], or proposals to exploit higher excited states in ^{87}Rb [187].

4.2 Polarisation-preserving quantum frequency conversion

Nonlinear optical processes can transform the frequency of light [195]. This section gives a basic description of these processes with a focus on the conversion efficiency and introduced background, which are most important for QFC in a quantum networking setting, for which we follow the derivations in [185] and [195]. Furthermore, we see that the processes are polarisation dependent. In our experiments, however, quantum information is encoded in the polarisation state of the single photons, which makes it essential to preserve the polarisation during conversion.

4.2.1 Three-wave mixing in waveguides

Three-wave mixing

Optical nonlinearities are described by the dependence of the dipole moment per unit volume of a material, i.e., polarisation $P(t)$, on an applied optical field $E(t)$. To find the nonlinear dependencies, the polarisation can be expressed as a power series in the field strength as

$$P(t) = \epsilon_0[\chi^{(1)}E(t) + \chi^{(2)}E^2(t) + \chi^{(3)}E^3(t) + \ldots], \tag{4.1}$$

where ϵ_0 is the permittivity of free space and $\chi^{(1)}$, $\chi^{(2)}$, and $\chi^{(3)}$ are known as the linear, second-order nonlinear, and third-order nonlinear optical susceptibilities, respectively, which are material dependent. Laser light can reach intensities that make the higher order terms relevant. For the purpose of QFC, we are interested in the three-wave mixing processes, which are second-order nonlinear processes, and hence we will neglect higher-order terms.

Let us consider an optical field incident upon a second-order non-linear optical medium that consist of two distinct frequency components (ω_1 and ω_2) represented as $E(t) = E_1 e^{-i\omega_1 t} + E_2 e^{-i\omega_2 t} +$ c.c.. Based on Eq. (4.1), we find a second-order nonlinear polarisation of

$$
\begin{aligned}
P^{(2)}(t) = \epsilon_0 \chi^{(2)}[&E_1^2 e^{-i2\omega_1 t} + \text{c.c.} && \text{(SHG)} \\
+&E_2^2 e^{-i2\omega_2 t} + \text{c.c.} && \text{(SHG)} \\
+&2E_1 E_2 e^{-i(\omega_1+\omega_2)t} + \text{c.c.} && \text{(SFG)} \\
+&2E_1 E_2 e^{-i(\omega_1-\omega_2)t} + \text{c.c.} && \text{(DFG)} \\
+& \ldots .
\end{aligned}
\tag{4.2}
$$

Here the different physical processes are labelled, namely, second harmonic generation (SHG), sum frequency generation (SFG), and difference frequency generation (DFG), which are visualized in Figure 4.2.

Maxwell's equations describe the generation of the new frequency components for light propagating through a nonlinear optical medium and couple the frequency components of the field by the nonlinear interaction. When we assume a second-order nonlinear and non-magnetic dielectric medium, this results in the following wave equation

$$\triangledown^2 E - \frac{n^2}{c^2}\frac{\delta^2 E}{\delta t^2} = \frac{1}{\epsilon_0 c^2}\frac{\delta^2 P^{\mathsf{NL}}}{\delta t^2}. \tag{4.3}$$
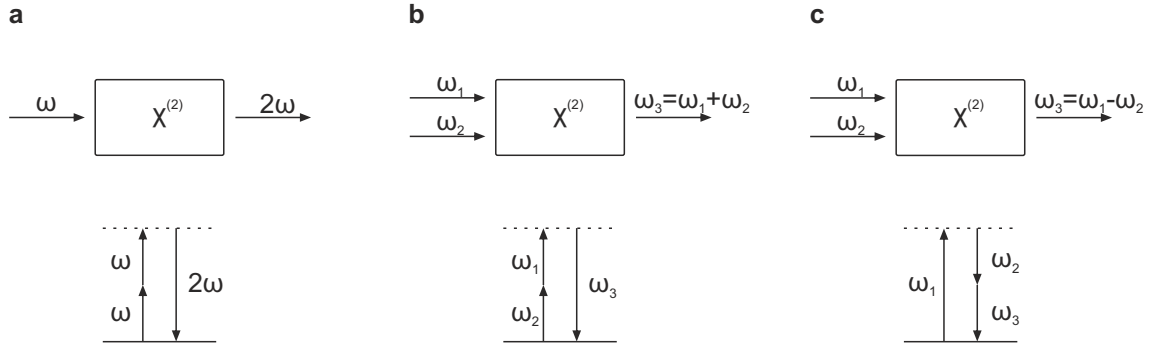
Figure 4.2: **Three-wave mixing in a nonlinear medium.** Geometry (top) and energy-level description (bottom) of the incident light fields interaction with a nonlinear medium. **a**, Second-harmonic generation (SHG) leading to the generation of radiation at twice the original frequency. **b**, Sum frequency generation (SFG) for up-conversion of light for frequency components of the input (ω_1), pump (ω_2), and target (ω_3) fields. **c**, Difference frequency generation (DFG) down-converting the frequency of the input light by mixing with a pump field, as employed in this work. Adapted from [195].

Now we solve these equations exemplarily for the DFG process with incident fields propagating along the z-axis. For this, we represent the frequency components of the input, pump, and target electric fields ($i = 1$, 2, and 3, respectively) as

$$E_i(z,t) = A_i e^{i(k_i z - \omega_i t)} + \text{c.c.}, \tag{4.4}$$

where the dispersion relation is denoted as $k_i = \frac{n_i \omega_i}{c}$ and the frequency dependent linear refractive index is given by $n_i = n(\omega_i)$. Inserting Eq. (4.4) into Eq. (4.3), while setting P^{NL} equal to the DFG component of $P^{(2)}(t)$, results in the following coupled amplitude equations

$$\frac{\delta A_1(z)}{\delta z} = i\kappa_1 A_2 A_3 e^{-i\Delta k z},$$

$$\frac{\delta A_2(z)}{\delta z} = i\kappa_2 A_1 A_3^* e^{i\Delta k z}, \text{ and} \tag{4.5}$$

$$\frac{\delta A_3(z)}{\delta z} = i\kappa_3 A_1 A_2^* e^{i\Delta k z},$$

where $\kappa_i = 2\omega_i d_{\mathsf{eff}}/n_i c$ and d_{eff} is the effective nonlinear interaction strength. Moreover, the parameter Δk is introduced as the phase (or wavevector) mismatch, defined as

$$\Delta k = k_1 - k_2 - k_3. \tag{4.6}$$

The coupled amplitude equations can be solved analytically for specific initial conditions and assumptions about the experimental system.

To illustrate the phase-matching considerations, let us first consider the limit of low conversion efficiencies where the amplitudes A_1 and A_2 remain constant $\delta A_1(z)/\delta z = \delta A_2(z)/\delta z = 0$. We obtain an intensity of the target field behind a crystal with length L of

$$I_3(L) \propto |A_3(z)|^2 = \kappa_3^2 |A_1|^2 |A_2|^2 L^2 \text{sinc}^2\left(\frac{\Delta k L}{2}\right). \tag{4.7}$$

We observe that the target intensity $I_3(L)$ is maximal when $\Delta k = 0$ for which it increases quadratically with z. On the other hand, when the phase mismatch does not equal zero it reduces rapidly. In general, the phase matching condition cannot be satisfied for dispersive media where $n_1 \neq n_2 \neq n_3$, since energy and momentum cannot be conserved simultaneously. Hence, the target intensity oscillates over z with a period of $2L_c = 2\pi/\delta k$ (and does not increase) since wavelets created at different positions of the crystal are out of phase and destructively interfere.

Quasi-phasematching (QPM) solves this problem by periodically poling the ferroelectric domains in the crystal. This results in a π phase shift of the target electric field at the periodic sign changes. For a poling period of Λ, QPM introduces an additional term to the phase mismatch parameters as

$$\Delta k' = k_1 - k_2 - k_3 - \frac{2\pi}{\Lambda}. \tag{4.8}$$

When $\Lambda = 2L_c$, the wavelets created at different positions of z interfere constructively, thus realising an increase of the target intensity over z. Note that poling the crystal reduces d_{eff} by a factor of $2/\pi$ and hence is less efficient than ideal phase matching [185, 195].

For the experiments presented here, we are interested in the solution of the coupled amplitude equations in the limit of high conversion efficiencies. Therefore, we consider a weak input field $A_1(z) \ll A_2(z)$ together with the initial condition $A_1(z = 0) = A_{\text{in}}$, a not depleting pump field $\delta A_2(z)/\delta z = 0$, a weak and initially absent target field $A_3(z = 0) = 0$, and perfect phase matching of the fields $\Delta k = 0$. This results in the following solution for the coupled amplitude equations:

$$\begin{aligned} A_1(z) &= A_{\text{in}} \cos\left(\sqrt{\kappa_1 \kappa_3 |A_2|^2} z\right) \\ A_3(z) &= A_{\text{out}} \sin\left(\sqrt{\kappa_1 \kappa_3 |A_2|^2} z\right). \end{aligned} \tag{4.9}$$

Given an input power before the crystal of $P_{\text{in}} = |A_1(0)|^2 = |A_{\text{in}}|^2$, a pump power of $P_{\text{pump}} = |A_2|^2$, and an target power after the crystal of length L of $P_{\text{out}} = |A_3(L)|^2$, we define the power conversion efficiency

$$\eta_{\text{con}} = \frac{I_{\text{out}}}{I_{\text{in}}} = \frac{P_{\text{out}}}{P_{\text{in}}} \sin^2\left(\sqrt{\eta_{\text{nor}} P_{\text{pump}}} L\right) \tag{4.10}$$

where $\eta_{\text{nor}} = \kappa_1 \kappa_3$. For QFC, however, the figure of merit is the photon-to-photon conversion efficiency, which is calculated as $\eta_{\text{qfc}} = \eta_{\text{con}} \times \omega_1/\omega_3$. Furthermore, to model inefficiencies in an experimental set-up due to, e.g., imperfect mode overlap or photon loss, we introduce the parameter η_{max} and obtain the photon-to-photon quantum frequency conversion efficiency

$$\eta_{\text{qfc}}(P_{\text{pump}}) = \frac{\omega_{\text{input}}}{\omega_{\text{target}}} \eta_{\text{max}} \sin^2\left(\sqrt{\eta_{\text{nor}} P_{\text{pump}}} L\right). \tag{4.11}$$

Lithium niobate waveguides

Waveguide structures increase the efficiency of the conversion process by transversely confining the light fields allowing for a good mode overlap of the three fields over the complete length of the waveguide, which is in sharp contrast to focussed beams in bulk crystals. We selected lithium niobate ($LiNbO_3$) to aid the three-wave mixing process since it has one of the highest

non-linear coefficients among solid-state materials [196]. Moreover, it is transparent over a wide spectral range and, over the years, manufacturing methods have matured making high-quality periodically poled waveguide structures commercially available.

In general, the material dependent second-order susceptibility $\chi^{(2)}$ is a third-rank tensor with a total of 27 elements, which is reduced to 10 independent elements by symmetries. Lithium niobate has three non-zero elements, in the contracted notation d_{il}, approximated by $d_{33} = \frac{1}{2}\chi^{(2)}_{333} \approx 25$ pm/V, $d_{22} = \frac{1}{2}\chi^{(2)}_{222} \approx 2.1$ pm/V, and $d_{31} = \frac{1}{2}\chi^{(2)}_{311} = \frac{1}{2}\chi^{(2)}_{131} = \frac{1}{2}\chi^{(2)}_{113} \approx 4.3$ pm/V. Note that the exact values depend on the specific material properties and the wavelength combination.

We are interested in $d_{33} = d_{\text{eff}}$, which crucially exceeds the other elements by an order of magnitude. This element is accessed when $E(t)$ and $P(t)$ are orientated along the z-axis. Hence, for incident fields along the z-axis, Eq. (4.1) simplifies to

$$P_z^{(2)}(t) = 2\epsilon_0 d_{33} E_z^2(t). \tag{4.12}$$

Note that the different interaction strengths of d_{22} and d_{33} lay at the origin of the polarisation selectivity of the three-wave mixing process. Furthermore, although both interaction strengths are non-zero, it is improbable that they are addressed simultaneously due to different phase matching conditions. In particular, since lithium niobate is birefringent and hence has different refractive indices for the two orthogonal linear polarisations, phase matching would require different poling periods of the crystal for the two polarisations.

Background processes

Background at the single photon level can already reduce the observed atom-photon and atom-atom entanglement fidelities. Since the pump field power is 16 orders of magnitude larger than the target field, very inefficient could already introduce some background. Here we discuss the relevant processes for this work, for a more thorough analysis we refer to [185].

The main sources of background are two fold: the first is Raman scattering of the pump laser which can create (annihilate) a phonon in the crystal while scattering a photon with reduced (increased) energy, which is termed (anti-)Stokes Raman scattering. The Raman scattering spectrum observed in waveguides are in agreement with spectra in bulk [197] and involve multiple Lorentzian shaped peaks around the pump wavelength (~ 50 nm). For low temperatures, the anti-Stokes Raman noise is suppressed due to the absence of phonons, in contrast to the Stokes Raman noise. Even at room temperatures, this effect is still present and results in a significantly lower anti-Stokes Raman noise compared to Stokes Raman noise. The second source of background is a series of nonlinear, weakly phasematched processes introduced by fabrication inaccuracies of the waveguide poling period [198]. The amplitude of this background is about 4 orders of magnitude lower than the peaks of the Raman scattering, however, it introduces background at the complete spectrum and hence can become dominant for larger spectral separations of the pump and target fields [185].

The conversion induced background noise can be reduced by careful selection of the pump–target wavelength combination, narrow-band spectral filtering, and minimizing photon acceptance interval, as will be discussed for the presented set-up in Section 4.2.3. Choosing $\lambda_{\text{pump}} > \lambda_{\text{target}}$, i.e., long-wavelength pumping, overcomes Stokes Raman noise in the proximity of the target wavelength. Especially in combination with (narrow-band) spectral filtering around the target wavelength this can greatly reduce the amount of background. Finally, since the detection time of the converted photons is known and background does not have any time dependence,

gating the detectors for a short time interval around the expected detection time reduces the noise even further.

4.2.2 Polarisation-preserving schemes

For polarisation encoded qubits it is essential to preserve the polarisation during conversion. Various approaches exist to circumvent the polarisation selectivity of the three-wave mixing process, categorised in two- or one-crystal and two- or one-path schemes. In arguably the most straightforward implementation the input beam is split by a PBS of which each output port contains a waveguide crystal for conversion, afterwards the beams are combined with a second PBS, i.e., a Mach-Zehnder configuration employing two crystals and two paths—one for each polarisation component [199]. Disadvantages are the necessity of two crystals together with the additional optics and the requirement to stabilize the path length difference in the two arms to achieve polarisation-preserving conversion for an arbitrary polarisation input. The latter is avoided when the two crystals are placed in series along one path, e.g., with a relative rotation of 90° around the optical axis [189]. However, in this so-called crossed-crystal configuration, each polarisation component propagates through two crystals, introducing additional losses.

The Sagnac configuration overcomes these issues by employing a single crystal and, although counter-propagating, having one path for the polarisation components [94], see, e.g., the schematic in Figure 4.5. In this work we use the Sagnac configuration, which has the following advantages above others.

- Each polarisation has a single pass though the waveguide, hence minimizing coupling losses.

- All modes in the waveguide have the same polarisation, thus preventing losses by different spatial modes.

- The configuration is highly symmetric, therefore achieving similar efficiencies for both polarisations.

- The number of optical elements is minimized, thus increasing the stability and simplicity of the set-up.

- The different polarisation components propagate along the same path, in this way making the output intrinsically phase-stable.

The first three points increase the efficiency of the device while the last two increase the stability and simplicity of the set-up, and thereby the ease of operation.

4.2.3 Design criteria and wavelength selection

The employed QFC system coherently transfers the 780 nm photons to the S-band at 1522 nm by mixing them with a 1600 nm pump field. The wavelength selection for the conversion process is based on several criteria, which can be summarized as follows.

- Target wavelength lies within the low-loss telecom band.

- Low background around the target wavelength.

- Availability of stable, narrow-linewidth, high-power lasers ($<$ 1MHz, $\sim$2 W) at the mixing wavelength.

- Photons converted by different QFC devices can be spectrally indistinguishable.

To minimize fibre attenuation losses, the target wavelength should be within the range of 1260–1675 nm; preferably avoiding the HO absorption peak at 1383 nm and being close to 1550 nm—which has the lowest attenuation loss of around 0.2 dB/km. For our initial wavelength, this limits the mixing wavelength to the range of 1460–2050 nm.

Background at the single-photon level can negatively effect the observed state fidelities after conversion. Hence, to avoid the largest noise source, i.e., Stokes Raman noise, the mixing wavelength should be $>$1560 nm. Moreover, anti-Stokes Raman noise is minimized by maximizing the signal to pump difference—favouring longer mixing wavelengths.

The availability of single-mode, high power mixing lasers divides the wavelength range into two windows: 1560–1610 nm covered by Erbium-doped fibre amplifiers (EDFA) and 1900–2050 nm where Thulium-doped fibre lasers (TDFA) operate. In the latter window, one expects superior noise properties due to the large pump to target wavelength separation. However, the target photons are located in the telecom O-band and will face slightly higher attenuation losses in optical fibres of around 0.35 dB/km.

To facilitate high contrast two-photon interference for photons converted by two different QFC devices, the mixing light requires a common frequency reference more accurate than the single-photon linewidth, here 5.1 MHz. This favours the EDFA window, as the seed light can be conveniently distributed to the nodes via telecom fibres, which guarantees spectral indistinguishability of the photons after conversion.

Based on this, we selected a mixing wavelength in the high-end of the EDFA gain spectrum; requiring a more involved spectral filtering system to suppress the anti-Stokes Raman noise, however, experiencing a favourable fibre attenuation at the target wavelength and simplifying the set-up needed to enable for high-quality two-photon interference. This is a similar wavelength combination as implemented in [94].

Operation wavelength

For the experiments presented in this chapter the mixing wavelength is set to 1600 nm, resulting in a target wavelength of 1522 nm. During the experiments presented in Chapter 5 a more favourable wavelength combination with respect to the anti-Stokes Raman is selected: mixing with 1607 nm, which sets the target wavelength to 1517 nm. This reduces the background introduced by the QFC device by a factor of 8 (see Figure 4.4b). For future experiments, in which the mixing light might need to be distributed over long fibres using standardized multiplexing techniques, the mixing wavelength could be adjusted accordingly. For example, using coarse wavelength division multiplexing (CWDM), mixing with 1610 nm would allow for distribution of the pump seed light via a standardized CWDM channel.

4.3   QFC system

4.3.1   Experimental realisation

Frequency converter

QFC to the telecom S-band is realized by difference-frequency generation (DFG) in a periodically poled lithium niobate (PPLN) waveguide. The waveguide chips (NTT Electronics) contain 6 waveguides with a length of 40 mm, 8-10 μm width and height, and poling period of around 18.25 μm. Active temperature stabilization allows to phase match a given wavelength combination. The waveguides enable conversion to a target wavelength range of 1360–1550 nm and are stabilized to a temperature in the range 40–55°C for conversion to 1522 nm. For a complete characterisation of the waveguides see [185].

Polarisation preservation is achieved by the realization of a Sagnac-type set-up [94]—favourable to the other configurations because of its intrinsic phase stability. Accordingly, the single photons at 780 nm are overlapped with the strong cw pump field at 1600 nm using a dichroic mirror and the beams are split into two arms with a polarizing beam-splitter (PBS). An achromatic half-wave plate (HWP) is introduced in one of the arms such that the two counterpropagating beams have the same polarisation when entering the waveguide. Both beams are coupled to the PPLN waveguide with aspheric lenses. The two arms are recombined at the PBS, after which the converted light, i.e., the single photons at 1522 nm, is separated from the pump light with another dichroic mirror and coupled into a telecom fibre. The conversion efficiency of both arms is set equal by fine tuning the pump field powers in the arms individually, see Figure 4.3.

Pump field set-up

The mixing light originates from an external cavity diode laser (DL pro, Toptica Photonics) which is amplified by an Erbium-doped fibre amplifier (EDFA) (CEFA-L-PB-HP-PM-33, Keopsys). Due to the absence of narrow-linewidth absolute frequency references, the diode laser is frequency stabilized via a transfer cavity lock, in analogue to [200]. To obtain long-term locking stability, the transfer cavity is placed in a vacuum set-up; the laser system frequently stays locked for more than a week.

Spectral filtering set-up

Various spectral filtering stages efficiently separate the single telecom photon from the strong pump field and the anti-Stokes Raman noise induced by the pump field in the waveguide. The first filtering stage contains a dichroic mirror separating the target and pump frequencies. The narrow-band filtering system relies on a Fabry-Perot filter cavity (FC) with a bandwidth of 27 MHz and a free spectral range of 19.3 GHz in combination with a volume Bragg grating (VBG) with a 25 GHz FWHM bandwidth; note that the bandwidth of the VBG is smaller than two free spectral ranges of the FC, allowing to select a single resonance mode of the FC. However, neighbouring modes are not perfectly suppressed, resulting in an effective filter bandwidth of 36.5 MHz. The FC length is actively stabilised to the pump laser at 1600 nm while having a further resonance at the telecom single photon frequency. The pump light is further suppressed by two shortpass filters (SPF) with a cut-off at 1560 nm and a bandpass filter (BPF) at 1535 nm with a bandwidth of 30 nm FWHM.
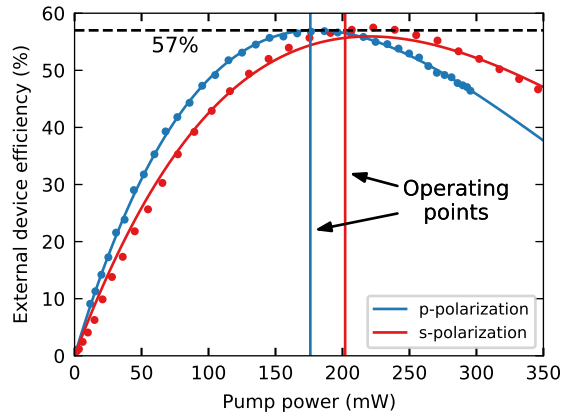
Figure 4.3: **External device efficiency of the frequency converter.** The external device efficiency (η_{qfc}) of the two polarisation components depends on the pump power (P) in the respective arm. The data are fitted with Eq. (4.11) [201]. The power in each arm is set to the operating point such that both conversion efficiencies are equal and one efficiency is maximized. At this point, the external device efficiency is $\eta_{\mathsf{qfc}} = 57\%$.

The spectral filtering system is located right before the polarisation analysis set-up to allow for a simple extension of the filtering system for atom-atom entanglement experiments at telecom wavelength, requiring two filtering systems. In this way, both filtering systems share the same location and hence simplify the FC locking realization and operation.

4.3.2 Characterization QFC device

External device efficiency

The external device efficiency of the frequency converter, defined from the input fibre of the converter until the first waveplate of the polarisation analyser, equals 57%; this includes a 50 m optical fibre, the complete spectral filtering system, and is measured with cw-light. This is, to the best of our knowledge, the highest external device efficiency reported so far. The efficiency is limited by the transmission through optical elements (82.6%), fibre coupling (87.8%), waveguide coupling (90.0%), and spectral filtering (90.7%), which reduce the high internal conversion efficiency of 96.2%.

Background analysis

To get an estimate of the signal-to-noise ratio (SNR) and quantify the demands on the spectral filtering system, we analyse the spectral properties of the converter induced noise. Figure 4.4a shows a background spectrum of the QFC device in Lab 1 observed with an optical spectrum analyser (AQ6370B, Yokogawa) [185]. For this measurement, the mixing wavelength is set to 1600 nm and the spectral filtering system is removed, except for one shortpass filter at 1538 nm to suppress the pump light. Around the target wavelength (1522 nm) we observe a converter induced background of 41.1 photons per second per MHz. Figure 4.4b shows a noise spectrum for mixing wavelengths of 1600 nm and 1607 nm. This time employing a programmable spectral filter (WaveShaper 4000A/S-band) and low darkcount single-photon detectors achieving an almost zero noise floor.
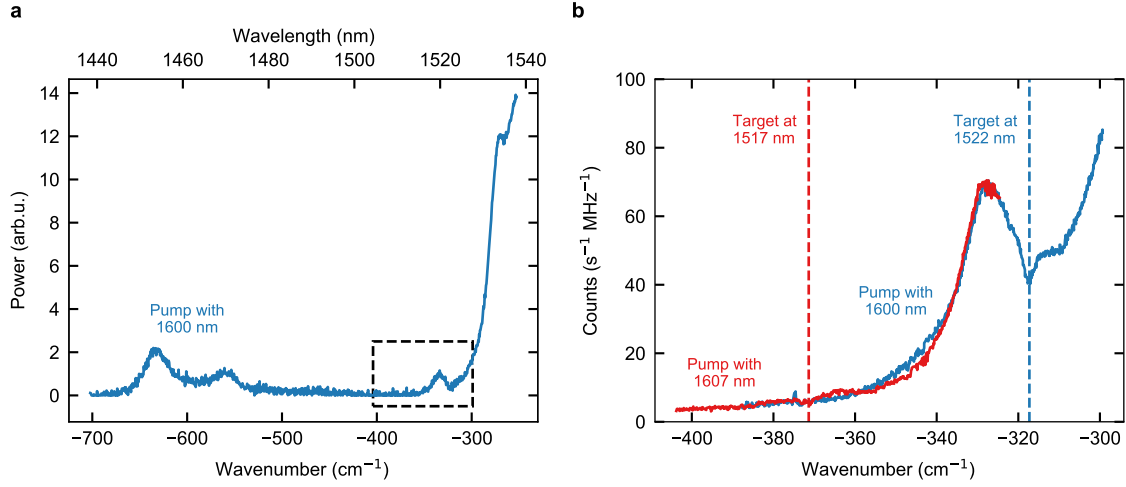
Figure 4.4: **Background spectrum of the QFC device. a**, Broad spectrum of the converter induced background for a mixing wavelength of 1600.14 nm (0 cm^{-1}) taken from [185]. For various spectral intervals the measured background approaches the noise level of the optical spectrum analyser. **b**, Narrow background spectrum (dashed rectangle in **a**) with mixing wavelengths of 1600.14 nm (blue) and 1607.11 nm (red). The background at the target wavelengths, 1522 nm and 1517 nm, respectively, show a factor 8 discrepancy. The vertical axis is scaled such that the background for a target wavelength of 1522 nm equals 41.1 counts (s^{-1} MHz^{-1}) [185].

The noise level that can be tolerated during the experiment depends on the amplitude of the signal, i.e., the efficiency to couple a single photon in the fluorescence fibre after an atomic excitation attempt. For the single-atom traps used here, typical efficiencies are $\eta_{\mathsf{photon}} = 1.0 \times 10^{-2}$ within a time interval of $\delta t = 208$ ns (see Section 2.3.2). This means that the background introduced by the converters should be well below $R_{\mathsf{qfc}} \ll R_{\mathsf{signal}} = \eta_{\mathsf{photon}}/\delta t = 4.8 \times 10^4$ counts per second. Taking into account the background measurement of 41.1 photons per second per MHz, this indicates that narrow-band filtering down to a few tens of MHz is necessary to achieve a SNR≫1 and minimize influence of the QFC induced noise on the observed state fidelities.

The expected SNR is estimated as follows. Assuming an effective filter bandwidth of 36.5 MHz and a background of 41.1 counts s^{-1} MHz^{-1} results in a background of $R_{\mathsf{qfc}} = 1500$ counts s^{-1}. The expected signal-to-noise ratio therefore approximates

$$\mathrm{SNR}_{1522} \approx \eta_{\mathsf{qfc}}\eta_{\mathsf{filter}} \frac{R_{\mathsf{signal}}}{R_{\mathsf{qfc}} + R_{\mathsf{darkcounts}}} = 14.4 \qquad (4.13)$$

where $\eta_{\mathsf{qfc}} = 0.57$ is the QFC external device efficiency for cw-light, $\eta_{\mathsf{filter}} = 0.8$ is the transmission of a single photon through the filter cavity, and $R_{\mathsf{darkcounts}} = 18$ cps equals the detector darkcounts. Taking into account that approximately 2/3 of the single photons are detected within a 50 ns time window, timefiltering can thus improve the SNR by a factor of $2/3 \times 208\mathrm{ns}/50\mathrm{ns} = 2.8$ to

$$\mathrm{SNR}_{1522} \approx 40.1, \qquad (4.14)$$

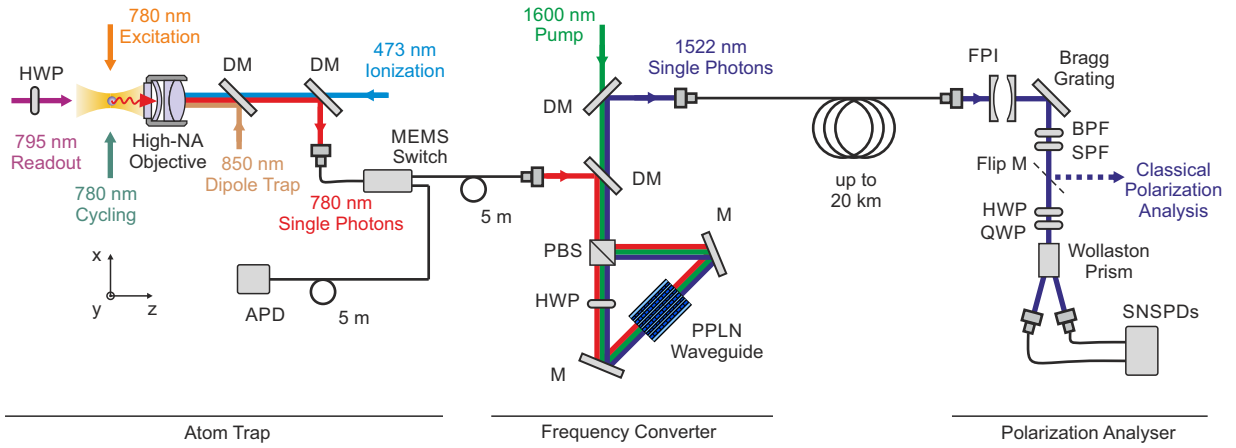evidently, at the cost of event rate.

Figure 4.5: **Schematic of the experimental set-up.** A single ^{87}Rb atom (upper left side), serving as quantum memory, is stored in the focus of a dipole trap (850 nm wavelength, 2.05 μm waist, and 42 mW power)—where a high-NA objective collects the atomic fluorescence. The MEMS switch guides the emitted photons towards the frequency converter where the 780 nm single photons are overlapped with 1600 nm pump light within a PPLN waveguide in a Sagnac-type interferometer to transfer the entanglement to 1522 nm photons. In the polarisation analyser the single photons are first spectrally filtered by a Fabry-Perot filter cavity (FC), volume Bragg grating, bandpass filter (BPF), and shortpass filter (SPF). Next, after setting the analysis basis with a half-wave plate (HWP) and a quarter-wave plate (QWP) and splitting the polarisation components by a Wollaston prism, the single photons are detected with two SNSPDs. Classical reference light, inserted along the readout path, can be coupled out with a flip mirror to analyse and compensate for polarisation drifts. Further abbreviations used: mirror (M) and dichroic mirror (DM). Adapted from [202].

4.4 Overview set-up and experimental sequence

Here we detail on the experimental set-up, methods, and sequence employed to observe and analyse long-distance atom-photon entanglement distribution at telecom wavelength. For more details about the single-atom trap and methods to generate and analyse the initial atom-photon entanglement, i.e., excluding quantum frequency conversion, we refer to Sections 2.2 and 2.3, respectively.

The experimental set-up consists of three parts: the single-atom trap located in Lab 1, a polarisation-preserving quantum frequency converter in Sagnac configuration, and a polarisation analyser which is connected via a single mode fibre of different lengths, as illustrated in Figure 4.5.

Fluorescence detection

The presence of an atom in the trap is verified by detection of atomic fluorescence light with a silicon avalanche photodiode (APD) located next to the single-atom trap. For this, a micro-electromechanical systems (MEMS) fibre switch is implemented in the single-mode fluorescence collection fibre. The switch either guides the atomic fluorescence to the APD while loading the trap or to the frequency converter during the state preparation and excitation cycles. The switching time of < 1 ms is fast compared to the atomic fluorescence integration time of around
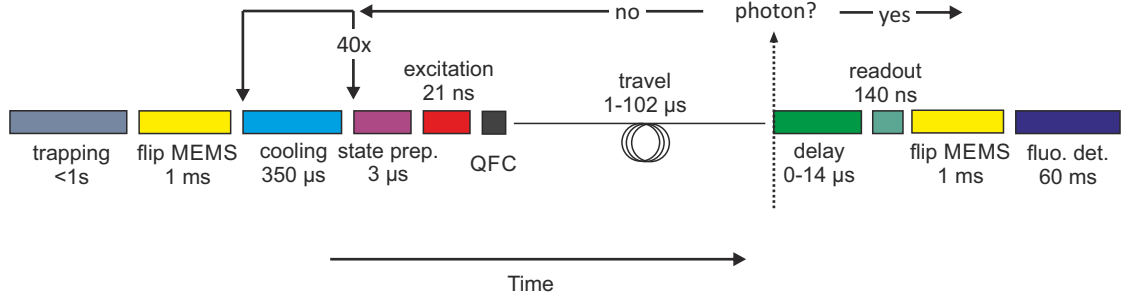
Figure 4.6: **Experimental sequence for long-distance distribution of atom-photon entanglement.** The travel time of the photons depends on the fibre length.

40 ms. The single photon detectors of the polarisation analyser cannot be used to check the presence of an atom in the trap since they are behind narrow-band (27 MHz FWHM) spectral filters resonant to the single-photon transition $5^2S_{1/2}|F = 1\rangle \leftrightarrow 5^2P_{3/2}|F' = 0\rangle$. Hence, these detectors do not observe atomic fluorescence at the transition used for fluorescence collection $5^2S_{1/2}|F = 2\rangle \leftrightarrow 5^2P_{3/2}|F' = 3\rangle$.

Polarisation analyser and single-photon detectors

The polarisation analyser consists of a motorized half-wave plate (HWP) and quarter-wave plate (QWP), a Wollaston prism, and two superconducting nanowire single-photon detectors (SNSPDs). The Wollaston prism projects the photon polarisation into two paths of which the photonic analysis basis is set by the waveplates. The single-photon detectors are located in the output ports of the prisms and have single-photon detection efficiencies of 16% and 18% at 1522 nm. Polarisation rotations in the complete single photon beam path—including the long fibres—are analysed and compensated for by using classical reference light and a fibre polarisation controller [122].

Experimental sequence

The experimental sequence is similar to the one discussed in Section 2.3.2 and is visualised for long-distance atom-photon entanglement distribution in Figure 4.6. A notable difference is that the MEMS switch is flipped to guide the atomic fluorescence either to the QFC device during the entanglement generation tries start or to the trapping APD. The excitation rate is mainly limited by the travel time of the photon through the optical fibre, resulting in an excitation rate of 7.3 kHz for the 20 km long fibre.

The polarisation state of the telecom photons is analysed after propagating through up to 20 km optical fibre. Photon detection events are accepted within an interval of 50 ns, which results in accepting approximately 2/3 of the converted single photons detection events (see left side panels of Figure 4.7). Following a successful detection event, the atomic spin state is analysed using a state-selective ionization scheme. The state selectivity is controlled by the polarisation of the readout pulse, see Section 2.3 for more details.

Table 4.1: **Overview of experimental configurations and measurement results.** The experimental configurations A, B, C, and D differ in optical fibre length, detection wavelength, and/or atomic state detection delay. The fidelity is obtained via Eq. (2.14), whereby the visibilities are fitted from the measured correlation probabilities. The S parameter (CHSH) is obtained directly from the measured correlations.

	A	B	C	D
Fibre length	20 km	10 km	50 m	5 m
Wavelength	1522 nm	1522 nm	1522 nm	780 nm
Readout delay	102 μs	51 μs	51 μs	51 μs
Fidelity ($\mathcal{F}$)	0.785(9)	0.843(9)	0.880(8)	0.897(7)
S (CHSH)	2.12(5)	2.37(4)	2.41(3)	2.49(3)
SNR	25	23	32	934

4.5 Results

4.5.1 Atom-photon entanglement over up to 20 km fibre

We analysed the entanglement between the atom and photon at telecom wavelength after propagation through 20 km (A), 10 km (B), and 50 m (C) optical fibre. Furthermore, to investigate possible noise induced by the QFC, a reference measurement was performed without frequency conversion (D). For measurements C and D we additionally applied an atomic state detection delay of 51 μs to make the loss in fidelity due to atomic state decoherence comparable to measurement B. Discussion of the results is focused on configuration A since it involves the longest fibre length. Figure 4.7 shows the photon detection time histogram and corresponding atom-photon state correlations for the measurement configurations. Furthermore, all experimental configurations and the obtained results are summarized in Table 4.1.

For configuration A, 11 335 events were observed within 360 minutes with an overall efficiency of detecting a telecom photon after an atomic excitation pulse of 1.7×10^{-4}. When optimizing the experiment for efficiency, e.g., by employing efficient single photon detectors (>85%) and replacing the lossy MEMS switch (25% loss), we expect an improvement of the overall efficiency by about one order of magnitude. The event rate in all measurements is ~35 per minute, mainly limited by the atom loading time of about 1 s since the atom is lost during the state readout process in approximately half of the cases.

Signal-to-noise ratio

The observed signal-to-noise ratio (SNR) for all configurations are listed in Table 4.1. The SNR is mainly limited by the QFC pump-laser induced noise and detector dark-counts. For measurement A these contributions amounted to 128 and 18 cps summed over both detectors, respectively. The observed SNR of 25 approximates our expectation, taking into account the 50 ns photon acceptance interval and the overall efficiency mentioned before.
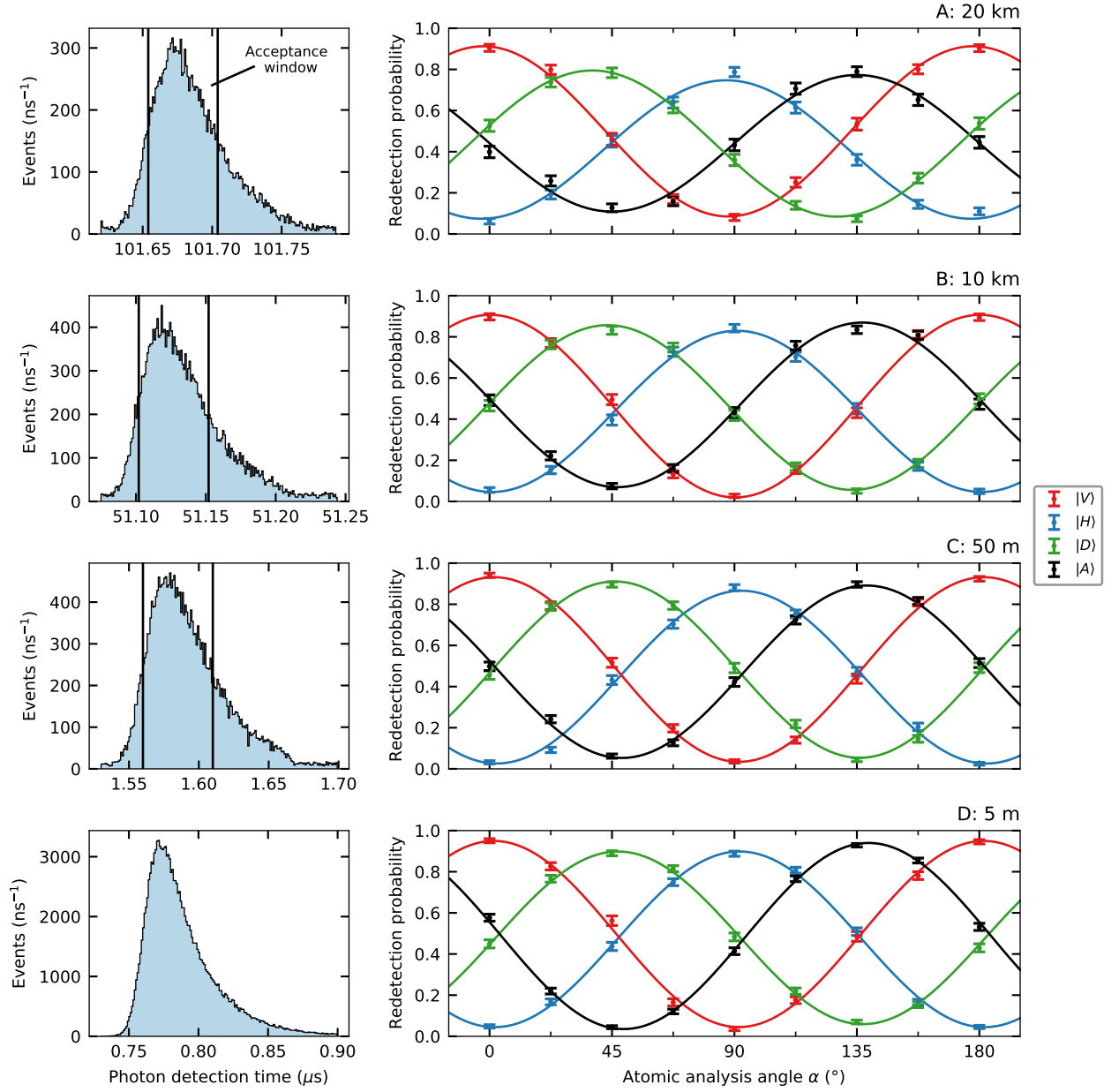
Figure 4.7: **Observation of atom-photon entanglement distributed via optical fibres.** Detection time histogram of the photons (left) and corresponding atom-photon state correlations (right) for fibre lengths of 20 km (A), 10 km (B), 50 m (C), and 5 m (D) (top to bottom). The photons in measurements A–C are frequency converted to 1522 nm, while measurement D is a reference measurement without conversion. The converted photons are accepted within a hard-wired time window of 50 ns, accepting approximately 2/3 of the single photons. Note that the QFC does not influence the photon shape [90]. In measurement D all photon clicks visible in the plot are accepted for further analysis. The atom-photon state correlations are measured in two bases (H/V and D/A) for varying atomic analysis angle (i.e. readout polarisation, whereby 0° corresponds to vertical polarisation). The observed average visibilities are 0.742(10), 0.812(11), 0.856(9), and 0.874(6), for measurement A, B, C, and D, respectively. The errorbars indicate statistical errors of one standard deviation.

For configurations A–C, however, one expects a similar SNR—changing the fibre length influences the signal and QFC noise in an equal manner as the QFC is the main noise contribution being much larger than the detector dark-counts. The lower SNR for configurations A and B is explained by an implementation detail causing a lower frequency of checking the presence of an atom in the trap. During these measurements, the presence of an atom in the trap was checked every 500 ms, which is relatively long compared to the lifetime of the atom of around 4 s. This results in excitation attempts while no atom is trapped, increasing the relative probability to observe background counts and hence lowering the SNR. Further variations in the SNR can originate from slight laser power fluctuations in the atomic state preparation and excitation cycles.

The SNR ratio lowers the observed visibility (V) of the atom-photon (and atom-atom) state as

$$V = V_0 \frac{SNR}{SNR + 1}, \tag{4.15}$$

where V_0 is the visibility without noise in the photon detection. Here we assume that the QFC devices introduce unpolarised noise and the detector darkcounts are comparable for the employed detectors. The influence on the fidelity is then estimated via Eq. (2.14) and (2.23), again assuming dephasing towards white noise.

Atom-photon entanglement fidelity

The entanglement between the single-atoms and single-photons was analysed following the methods presented in Section 2.3. Accordingly, we measured the photonic polarisation state in the H/V (horizontal/vertical) and D/A (diagonal/anti-diagonal) basis, while varying the atomic analysis angle (i.e. readout polarisation). The visibilities of the measured states are obtained by fitting the data with sinusoidal curves, as shown in Figure 4.7. The average visibility ($\bar{V}$) of the entangled state is estimated by averaging the visibilities of the three bases and assuming that the visibility in the third (unmeasured) basis is equal to the D/A basis. This results in estimated average visibilities of 0.742(10), 0.812(11), 0.856(9), and 0.874(6) for measurement A, B, C, and D, respectively. Note that the visibilities of the photon states $|V\rangle$ (red curves in Figure 4.7) are significantly higher than the other states since the resulting atomic state is insensitive to the position-dependent dephasing of the atomic state, which is the dominant decoherence effect for all other states. See Section 2.5 for more details and a simulation of the atomic state coherence.

The fidelity relative to a maximally entangled state is estimated using Eq. (2.14), resulting in a lower bound on the fidelity of $\mathcal{F} \geqslant$ 0.785(9), 0.843(9), 0.880(8), and 0.897(7) for measurement A, B, C, and D, respectively. For measurement A, contributions to the loss in fidelity are the imperfect atomic state readout (3%), atomic state decoherence (11%), SNR in the photon detection (4%), and experimental drifts (3%).

The influence of the QFC on the state fidelity is best studied by comparing measurement C ($\mathcal{F} \geqslant 0.880(8)$) and D ($\mathcal{F} \geqslant 0.895(5)$), since the experimental configurations are most similar, i.e., these configurations have relatively short fibre lengths, equal atomic readout times, and similar experimental sequences. For these measurements, the difference in fidelity can be solely explained by their difference in SNR (3%). When comparing measurement B ($\mathcal{F} \geqslant 0.843(9)$) and C ($\mathcal{F} \geqslant 0.880(8)$), the difference in fidelity is more than what can be expected from the lower SNR alone (1%). We attribute the additional fidelity loss (3%) in measurement B to instabilities in the experiment, such as fibre polarisation, magnetic field, and laser power drifts. The difference

in fidelity between measurement A ($\mathcal{F} \geqslant 0.785(9)$) and B ($\mathcal{F} \geqslant 0.843(9)$) originates primarily from atomic state decoherence (5%).

CHSH Bell test

All four measurements also include two setting combinations to conduct a CHSH Bell test [123]. The CHSH inequality requires two measurement settings for the photonic state (H/V & D/A) and two measurement settings for the atomic state α (22.5° or 157.5° & 67.5° or 112.5°). Table 4.1 lists the observed S parameters for the different experimental configurations—all violating the CHSH Bell inequality ($S > 2$) by several standard deviations.

4.5.2   Extrapolation to longer distances

To extrapolate the obtained results to longer fibre lengths, we modelled the physical processes that critically influence the atom-photon and atom-atom state fidelity. Increasing the fibre length effects the fidelities mainly in two ways: first, by decoherence of the atomic state during the longer travel times of the photons through the fibres, and, secondly, by detector dark-counts becoming the prominent source of noise due to attenuation of single-photons and QFC induced noise in the fibres.

The atomic state decoherence is simulated according to the model presented in Section 2.5. Furthermore, we include detector dark counts and attenuation in the long fibres. The expected atom-atom entanglement fidelity for varying distance is estimated by $\mathcal{F}_{\mathsf{aa}} \geqslant 1/9 + 8/9\bar{V}$, where the average atom-atom visibility $\bar{V}$ is estimated by squaring the corresponding atom-photon visibility and multiplying it with a 94% two-photon interference contrast [55]. In the presented simulations, we assume that the entanglement swapping required for the generation of atom-atom entanglement is performed at a middle station such that the atomic coherence time required to distribute atom-photon and atom-atom entanglement over the same distance evens up.

Figure 4.8 shows the simulations results of the expected atom-photon and atom-atom entanglement fidelities for a range of fibre lengths (1–400 km). Below 1 km the performance is limited by imperfections in the initial atomic state preparation and analysis. For longer distances, the atomic state decoherence will significantly reduce the fidelity due to the position-dependent dephasing [100] and magnetic field fluctuations, as detailed in Section 2.5.

In a future trap set-up, the decoherence effects introduced by the trap light could be mitigated by the applying a new trap geometry based on a standing wave dipole trap or by adiabatically ramping down the dipole trap power. The latter, in combination with a new qubit encoding approximately a factor 500 sensitive to magnetic fields [63], increased the coherence time of the atomic quantum memory to more than 7 ms and allowed for atom-photon entanglement distribution over 101 km optical fiber [127], as will be detailed in consecutive theses. The observed fidelities for this new set-up are for large distances limited by detector dark-counts.

4.6   Discussion and outlook

Towards long-distance atom-atom entanglement

The next milestone towards a large-scale quantum network is to distribute heralded entanglement at telecom wavelength between two distant atomic memories via the entanglement swapping protocol, which is subject to Chapter 5 of this thesis. For this purpose, it is necessary to introduce frequency conversion for a second atom trap and install a set of SNSPDs with higher
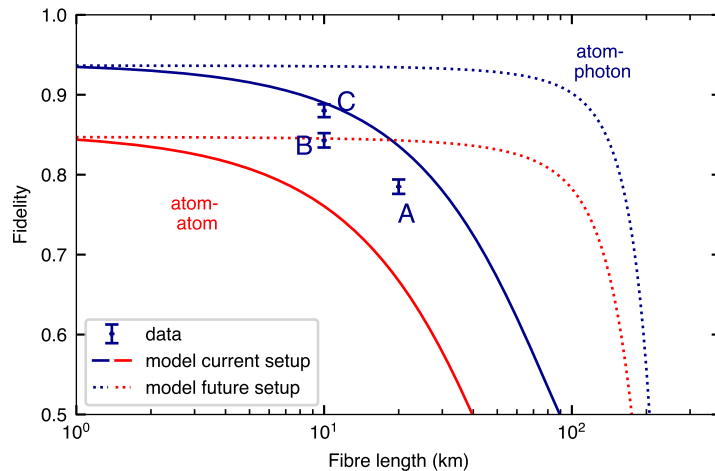
Figure 4.8: **Expected atom-photon and atom-atom entanglement fidelities.** Points marked as A, B, and C correspond to the atom-photon measurements presented in the text and summarized in Table 4.1. Simulations of the expected fidelity for the current (solid lines) and future (dotted lines) set-up based on an atomic state decoherence model including detector darkcounts. The expected fidelity for short distances (<1 km) is mainly limited by the imperfect atomic state preparation and readout. For distances <100 km, the fidelity is also reduced by atomic state decoherence due to position-dependent dephasing and magnetic field fluctuations, which could be strongly suppressed in a future set-up. Detector dark-counts eventually limit the state fidelity for distances >100 km.

detection efficiencies. Using the current trap geometry, we expect an atom-atom entanglement fidelity of 65% over 20 km with an event rate of $1/60$ s^{-1} and by improving the trap geometry, we expect a fidelity of 81% over a 20 km fibre link (see Figure 4.8). Together with entanglement distillation [71], this will allow for efficient distribution of quantum states over long distances in the future.

QFC to match operation frequencies

Besides increasing the span of fibre-based quantum network links, QFC also provides accurate control of the single-photon wavelength by adjusting the frequency of the mixing field. This enables to match frequencies of quantum memories which initially operate at different frequencies, hence allowing to generate entanglement between the memories via, e.g., entanglement swapping protocols. Especially for photon sources that do not have a reproducible emission spectrum, this is a valuable tool. For us, this allows to realize entanglement between a single-atom trap presented in this work with single ^{87}Rb atoms in optical cavities operating at different transitions [60]. For more details about this proposal see the general outlook of this thesis in Chapter 6.

Conclusion

Thanks to the record high external device efficiency of 57% for the polarisation-preserving QFC and improved collection optics for the atomic fluorescence, atom-photon entanglement was distributed and observed at high rate with a fidelity of at least 0.785(9) over 20 km optical fibre.

Implementing realistic improvements and extrapolating to even longer distances shows that entanglement distribution between atomic memories is feasible with a fidelity of more than 0.8 over up to 100 km, thereby forming a valuable component for future quantum repeater based quantum networks.

Chapter 5

Entangling Atoms over Long Telecom Fibres

Long-distance entanglement distribution between stationary quantum memories is the key ingredient for future quantum networks, which will enable for secure quantum communication and distributed quantum computing. Here we report on the entanglement between two remote quantum nodes—^{87}Rb atoms trapped and manipulated independently at locations 400 m apart—generated over fibre links with a length of up to 33 km. The scheme begins with in each node entangling the spin state of an atom with the polarization state of a photon. Subsequently, the photons, initially emitted by the atoms at 780 nm, are converted to telecom S-band at 1517 nm and transferred over several kilometres of fibre to a middle station, where a Bell-state measurement swaps the entanglement to the atoms. We analyse the heralded atom-atom entanglement along three bases after a delay allowing for two-way communication from the nodes to the middle station over the full fibre link length; this realistically evaluates the performance of a separation of the nodes. Work presented in this chapter resulted in the publication Van Leent, *et al. Nature* **607**, 69–73 (2022), and some parts of the text are based on this publication.

This chapter is organized as follows. It starts by discussing state-of-the-art quantum network experiments in Section 5.1, with a focus on multi-node experiments and long-distance entanglement distribution at telecom wavelength. Section 5.2 describes the additional experimental methods required for the single-atom based quantum network link with telecom interfaces. Next, in Section 5.3, we elaborate on the entanglement generation rate of the presented apparatus— which is a crucial parameter for the realization of quantum networks—with respect to the quantum network link length. Thereafter, in Section 5.4, the atom-photon entanglement distribution of both nodes is characterized in the two-node experimental configurations. Section 5.5 presents the main results of this chapter in two steps; first, it details on atom-atom entanglement over 6 km fibre, after which links up to 33 km are realised and analysed. The conclusion based on the results presented in this chapter is incorporated in the overall conclusion of the thesis in the next chapter.

5.1   Introduction

Sharing entanglement between distant quantum systems is a crucial ingredient for the realization of quantum networks [26, 31]. Photons are the tool of choice to mediate the entanglement distribution, typically either via controlled light-matter interaction with the local memories [60, 79], or, as it also will be used here, via entanglement swapping from photon-memory states [55,

72, 177]. Groundbreaking applications of such networks include distributed quantum computing [203] and device-independent quantum key distribution [38]. Since attenuation losses in the distribution process are inevitable, quantum repeaters will be essential to efficiently distribute entanglement via intermediate nodes. Moreover, since entanglement distribution is a probabilistic process, it essential to signal the successful generation of entanglement between nodes.

To minimize absorption and thus to maximize the distance between neighbouring nodes in future quantum networks employing the readily available fibre infrastructure, it is necessary to operate at telecom wavelength. Employing quantum frequency conversion (QFC) [90–93, 204], as introduced in the previous chapter, light-matter entanglement distributed at the low loss telecom band has recently been demonstrated for various types of quantum memories, including NV-centers, ions, atoms, and atomic ensembles [94, 95, 191, 194], even over tens of kilometres of fibre [193, 202]. This was mainly enabled by novel quantum frequency converters, which, while preserving the photonic polarization, have reached external device conversion efficiencies up to 57% [202].

For future quantum communication and repeater scenarios, it is vital that the nodes are independent and distant, employ long-lived quantum memories, and, at the same time, provide the availability of heralded entanglement. So far, heralded entanglement distribution between two independent nodes has been limited to fibre lengths up to 1.7 km [5, 8, 205]. Recently, great progress was made by demonstrating entanglement distribution at telecom wavelength between atomic ensembles [96, 206] and multimode solid-state quantum memories [97, 177]. However, to fully use the entanglement over long-distance quantum network links it is mandatory to know it is available at the nodes before the entanglement decays.

5.2 Experimental methods

In this section we detail on the realization of a symmetric two-node setup that generates entanglement using telecom wavelength photons. The nodes are formed by a single-atom trap setup, as described in Chapter 2, equipped with a QFC devices, as reported in Chapter 4. The Bell-state measurement for the entanglement swapping is performed with the converted photons at telecom wavelength. Here we discuss the setup, experimental control, and implemented sequence.

5.2.1 Set-up

The experimental setup consists of two similar, independent nodes and a middle station, as illustrated in Figure 5.1. The nodes and middle station are all located in different laboratories. In particular, Node 1 is located in Lab 1 and Node 2 in Lab 2, which are 400 m line-of-sight apart (see Figure 2.2), and the middle station is based in a Lab 3 approximately 20 m away from Lab 1. The shortest possible fibre connection from Node 1 (Node 2) to the middle station equals 50 m (750 m), where the fibre length to the middle station is denoted as L_1 (L_2), with the total link length $L = L_1 + L_2$. Fibre links with a length of $L = 6, 11, 23,$ and 33 km are realized by inserting additional fibres on spools (Corning, SMF-28e+), for an overview of the fibre configurations see Table 5.1.
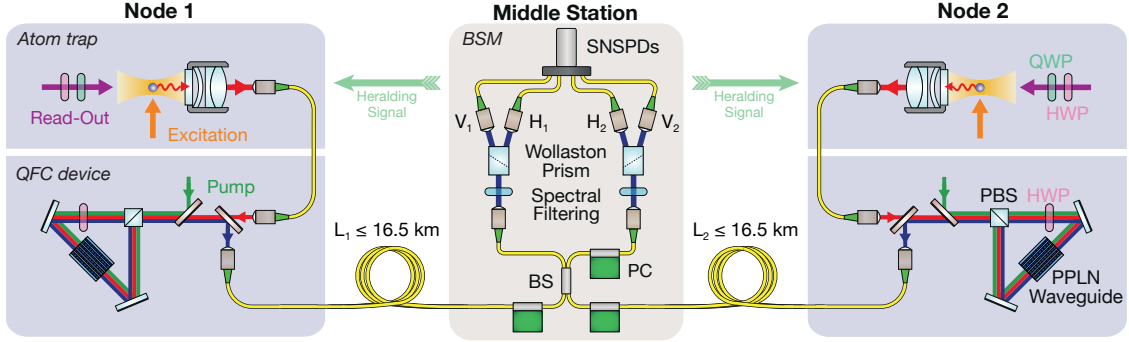
Figure 5.1: **Schematic of the experimental setup.** In each node, physically separated by 400 m, a single ^{87}Rb atom is loaded in an optical dipole trap. Both atoms are synchronously excited to the state $5^2P_{3/2}|F' = 0, m_F = 0\rangle$ with an excitation pulse (780 nm) to generate atom-photon entanglement in the subsequent spontaneous decay. The single photons are collected using high-NA objectives and coupled into single mode fibres leading to the QFC devices. There, they are converted to telecom wavelength at 1517 nm via difference frequency generation (DFG) in a PPLN waveguide located in a Sagnac interferometer type setup. This configuration preserves the polarization state of the photons during conversion. The converted photons are guided to a middle station via fibre links with lengths up to 16.5 km, where the entanglement is swapped to the atoms via a Bell state measurement (BSM). After successfully generating atom-atom entanglement, the atoms are independently analysed by a read-out pulse (795 nm) of which the polarization, set by a half-wave plate (HWP) and quarter-wave plate (QWP), defines the measurement setting. Adapted from [176].

Table 5.1: **Long fibre configurations and corresponding atomic readout times.** L_1 (L_2) equals the fibre length between Node 1 (Node 2) and the middle station, whereby A_1 (A_2) equal the attenuation over the fibre links. The atomic readout time after excitation in de nodes is give by t_1 (t_2).

L (km)	L_1 (km)	L_2 (km)	A_1 (dB)	A_2 (dB)	t_1 (μs)	t_2 (μs)
6	2.6	3.3	-0.7	-0.8	28.5	35.5
11	5.4	5.5	-1.5	-1.3	57.1	71.0
23	11.3	11.4	-3.3	-2.8	114.2	124.3
33	16.5	16.6	-4.5	-4.1	171.2	177.5

Single-atom traps

In both nodes, a single, optically trapped ^{87}Rb atom acts as quantum memory, where a qubit is encoded in the Zeeman-substates of the $5^2\mathrm{S}_{1/2}\,|F=1, m_F=\pm 1\rangle$ ground state, with $m_F=+1$ and $m_F=-1$ further denoted as $|\uparrow\rangle_z$ and $|\downarrow\rangle_z$, respectively (see Section 2.3). The traps are equipped with a local set of single-photon detectors to verify the presence of an atom in the trap. For this, a microelectromechanical systems (MEMS) fibre-optic switch is installed in each node at the fluorescence fibre. The switches guide the atomic fluorescence either to the local APD to check atom presence or to the QFC devices during the entanglement generation tries.

Both quantum memories have a coherence time T_2 of approximately 330 μs, which is achieved by active stabilization of magnetic fields (<0.5 mG) and applying a bias field of tens of milli-gauss along the y-axis (see Section 2.5). During the experiments presented in this chapter, an additional and unknown source of decoherence was present in Node 2, introducing noise on the order of 6 mG, which was effectively suppressed by the bias field. Surprisingly, when optimizing the experimental settings for configurations with longer fibre lengths in Node 2, i.e., later atomic readout times, we observed that smaller bias fields ($B_y = 10$–20 mG) resulted in better state fidelities than higher bias fields ($B_y = 50$–150 mG).

Quantum frequency conversion system

Both nodes are equipped with a QFC system, as described in Section 4.3. The narrow linewidth (< 1 MHz) pump light originates from a single laser source located in Lab 1 and is conveniently distributed to the nodes using the telecom fibre network, as illustrated in Figure 5.2. At the nodes, an Erbium-doped fibre amplifier (EDFA) amplifies the pump light to ~ 0.5 W for efficient DFG. Given that the photons emitted by the atoms trapped in Node 1 and 2 have indistinguishable frequencies before conversion, this ensures indistinguishable frequencies of the single photons after conversion.

In contrast to the experiments presented in Chapter 4, the pump wavelength is set to 1607 nm, resulting in a wavelength after conversion of 1517 nm and a factor 8 reduction of the anti-Stokes Raman noise around the target wavelength. Therefore, allowing to install a QFC device in both nodes without being limited by the converter induced noise.

Bell-state measurement setup

The converted single photons are analysed with a telecom BSM device consisting of a fibre beamsplitter (BS), two polarizing beamsplitters (PBS) (Wollaston prisms), and four single-photon detectors (SPDs), as illustrated in Figure 5.1. In this setup, the fibre BS guarantees a unitary spatial overlap of the photons originating from the nodes, while the PBSs and SPDs allow for polarization analysis in both output ports. A motorized QWP and HWP per output port set the photonic analysis angles.

Four superconducting nanowire single-photon detectors (SNSPD, Scontel) detect the converted photons, which all have an efficiency of $> 85\%$ at the converted photon wavelength and a darkcount rate of < 65 cps. The detectors can be operated in a low-noise mode by reducing the superconducting bias-currents: resulting in efficiencies of $> 65\%$ for darkcount rates of < 15 cps. While not used in the experiments presented here, this mode could improve the observed state fidelity when detector darkcounts are the main noise source, i.e, over fibre links of > 50 km (see Figure 5.7).

The installation of the detectors required special care. Equipment electronically connected to the detectors reduced their performance by increasing the darkcount rate via electronic ground
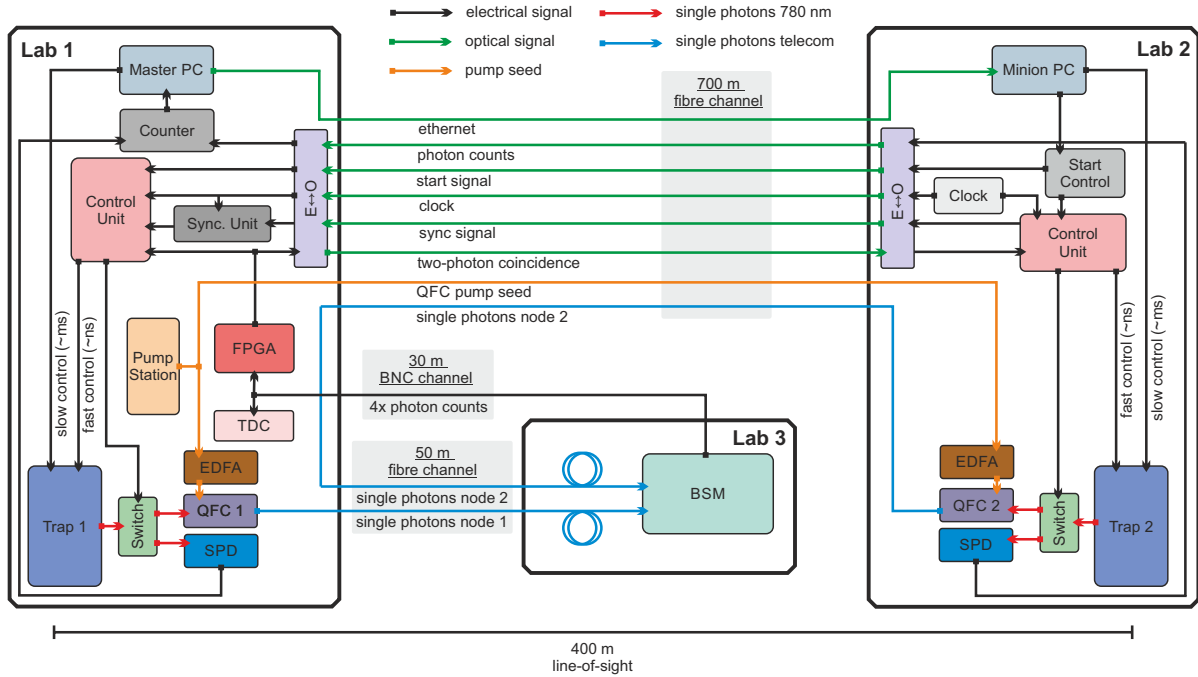
Figure 5.2: **Experimental control of the two-node telecom setup.** The arrow colors indicate the signal type (see legend); some signals are left out for simplicity. An optical fibre channel (700 m) connects Lab 1 and 2, while Lab 1 and 3 are connected via an electrical (30 m) and optical (50 m) channel. The Master PC initiates and monitors the atom loading process in both traps. Control units in each lab execute a synchronized experimental sequence to generate entanglement between the atoms. Successful generation of entanglement is registered by an FPGA, which sends a signal back to the CUs to start the atomic readout sequence in each trap. The seed light of the fibre amplifiers originates from a single laser in Lab 1. The single-photon paths from Trap 1 and 2 to the BSM are shown for completeness and long fibres can be inserted before the BSM setup.

loops. To integrate the detectors in the experimental setup, all electrical connections to other devices are digitally isolated (ADN4654, Analog Devices).

Communication between nodes

The communication between Lab 1 and 2 is performed at telecom wavelength [8, 104], as detailed in Section 2.4.2. For the experiments described here, Lab 3 is connected to Lab 1 via four 30 m long BNC cables and a 50 m long 20-fibre channel. Figure 5.2 visualises most communication between the three laboratories.

Fibre polarization control

Since the photonic qubit is encoded in the polarization state of the single photons, it is required to compensate for stress or temperature induced polarization drifts in the long optical fibres. Therefore, an automated polarization control system is installed, which is based on the set-up presented in Section 2.4.2, however, extended to compensate for polarisation drifts in the fibres from both nodes. For this purpose, laser light at the single photon frequency is overlapped with
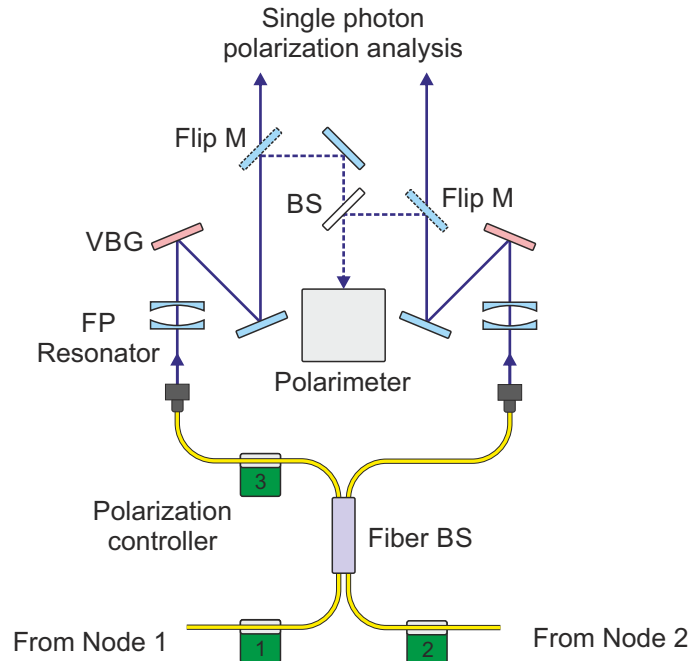
Figure 5.3: **Schematic of the spectral filtering and polarization control setup.** Detailed schematic of a part of the middle station. Each output arm of the fibre beamsplitter (BS) contains a filtering setup consisting of a Fabry-Pérot (FP) resonator and a volume Bragg grating (VBG). The polarimeter analyses the light polarization in the two linear bases [122].

the complete single photon path originating from Node 1 and 2, which includes the QFC stages. The laser light has sufficient optical power to be detected at telecom wavelength by conventional photodiodes used in a homebuilt polarimeter located at the BSM (see Figure 5.3). Two input polarization directions are used, vertical and diagonal, which are alternated at 10 Hz with a liquid crystal retarder (LCR). In both output arms of the fibre BS a flip-mirror reflects the classical light into a polarimeter during the optimization. Three fibre polarization controllers (PC) are connected to the fibre BS of the BSM: at both input ports and at one output port. The polarization controllers are set accordingly to the result of the gradient descent optimization algorithm in three steps. First, PC 1 is set according to the results of the optimization using light originating from Node 1 and analysing the right output port of the fibre BS with the polarimeter. Next, PC 3 is set using light originating from Node 1 and analysing the left output arm. Finally, PC 2 is set using light originating from Node 2 optimising the left output port of the fibre BS (it is also possible to optimise using the right output port). The polarization control is performed every 7 minutes and takes on average 20 seconds. In this way, polarization errors are kept below 1% for all fibre length configurations.

The employed link includes a 700 m field fibre crossing public space and a four lane street. Recently, polarization drifts over a 10 km field deployed fibre were characterized and compensated [207]. In our setup, including a 32.4 km spooled fibre in addition to the field fibre, we observe similar polarization drifts. This indicates that a setup including longer field deployed fibres should not introduce significantly more drifts than observed now and that the currently used system can compensate for polarization drifts with longer field deployed fibres.
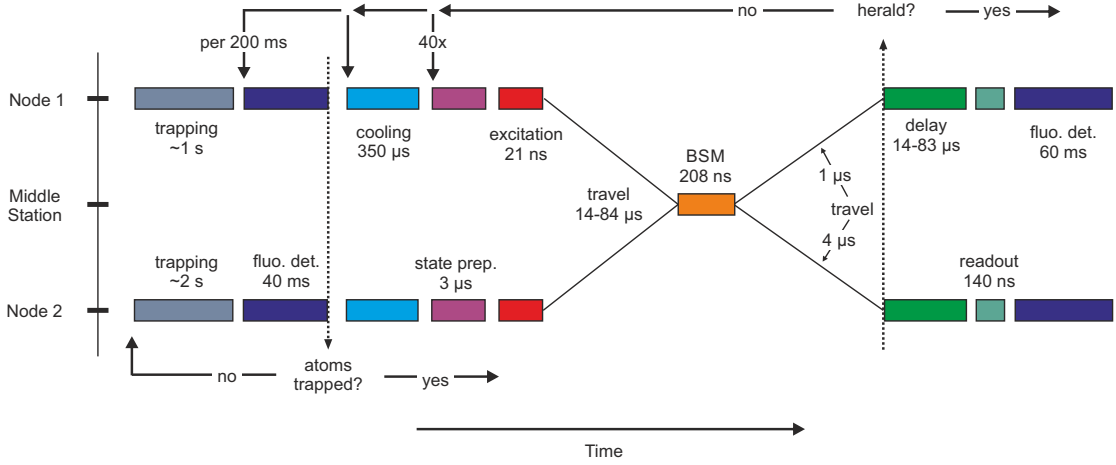
Figure 5.4: **Experimental sequence of the atom-atom entanglement generation.** In both nodes a single atom is trapped and cooled using polarization gradient cooling. Next, the entanglement generation tries start including state preparation and synchronous excitation of the atoms. The atoms are re-cooled after 40 unsuccessful entanglement generation tries. The travel time of the photons to the middle station equals 14–84 μs, depending on the fibre length. An additional delay, to account for the communication time from the middle station back to the nodes, is implemented only when receiving the heralding signal. After a 200 ms interval of entanglement generation tries the presence of the atoms in the traps is checked using fluorescence collection on an APD (see text). The QFC takes place subsequent to the atomic excitation.

Data acquisition

A home-built time-to-digital converter (TDC) located in Lab 1 is used as main data acquisition device in the experiment. It records logic signals with a resolution of 80 ps for 8 channels [8, 104]: namely, the counts of the four SNSPDs of the BSM, the trapping APD counts of each node, together with the timings of the excitation process and atomic readout times of Node 1.

5.2.2 Sequence

The atom-atom entanglement generation and analysis sequence is similar to the one presented in Section 2.4 and is visualised in Figure 5.4. The sequence starts by trapping an atom in both nodes, after which the entanglement generation tries start. Subsequent to each try, a waiting time is implemented to cover both the propagation time of the photons in the long fibres to the BSM and the heralding signal back to the nodes.

The employed BSM setup is aligned to analyse the photons in the H/V basis and hence heralds the following two Bell states

$$\left|\Psi^{\pm}\right\rangle = \frac{1}{\sqrt{2}}(\left|\uparrow\right\rangle_x \left|\downarrow\right\rangle_x \pm \left|\downarrow\right\rangle_x \left|\uparrow\right\rangle_x). \tag{5.1}$$

Two-photon coincidences are triggered within a hard-wired 208 ns long window which sends a herald signal back to the nodes. This signal is delayed electronically by $t \geq \ell/\frac{2}{3}c$ to simulate the signalling time back to the nodes, where $\frac{2}{3}c$ approximates the speed of light in an optical fibre and ℓ equals L_1 or L_2 for Node 1 or 2, respectively. Although lowering the observed final
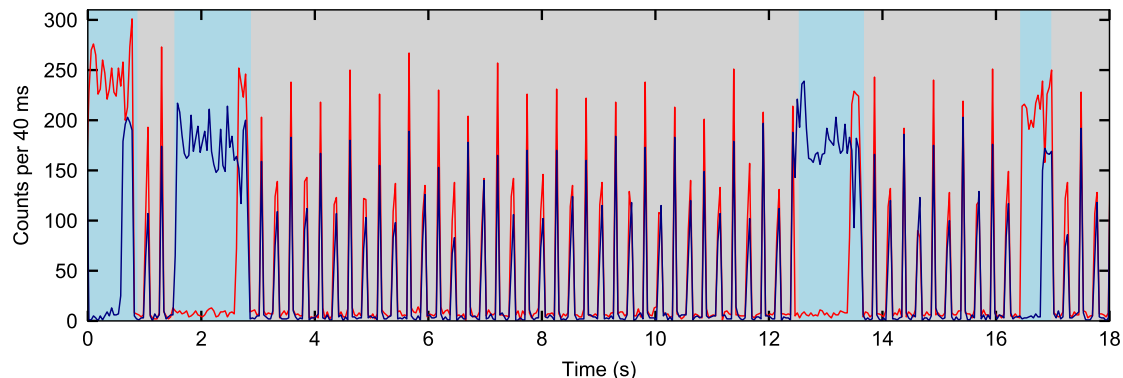
Figure 5.5: **Typical fluorescence trace in a two-node experiment.** Fluorescence counts integrated over 40 ms for Trap 1 (darkblue) and Trap 2 (red) recorded by the local single-photon detectors. The grey background indicates alternating periods of entanglement generation tries (200 ms, low number of counts) and fluorescence detection to check atom presence in both traps (40 ms, high number of counts if an atom is trapped). The lightblue background indicates loading periods of (one of) the single-atom traps.

fidelity, this delay is essential to study the performance of the quantum network link in a realistic scenario. Finally, the quantum state of the atomic memories is analysed with a state-selective ionisation scheme, whereby the state selectivity is controlled by the polarization of a readout laser pulse, for more details see Section 2.3 and [103].

The average lifetime of an atom in the trap during the entanglement generation process is 4 s (6 s) for Node 1 (Node 2). To verify if the traps still store a single atom during the entanglement generation tries, the process is interrupted after 200 ms to check for the presence of the atoms during 40 ms fluorescence collection recorded on the local single-photon detectors. Figure 5.5 shows a typical fluorescence trace observed with the local detectors during the experiment. Showing, for both traps, < 25 counts during the entanglement tries and > 50 during the fluorescence collection when an atom is present. Note that the SNSPDs of the BSM cannot be used to check atom presence since they are behind narrowband spectral filters (27 MHz) and the frequency of the fluorescence collection light and single photons differ by more than 6 GHz since they employ different atomic transitions.

Regular maintenance tasks lower the duty cycle of the experiment to approximately half, which is independent of the fibre configuration. The duty cycle is mainly reduced by the fraction of time required to simultaneously load an atom in the traps (0.40(5)), the fraction of time used to verify if both traps still store a single atom during the entanglement generation tries (0.18), and the fraction of time used to compensate polarization drifts of the long fibres (0.05).

5.3 Entanglement generation rate

The atom-atom entanglement generation rate r depends on the success probability for each entanglement generation try η_{aa}, which is predominantly reduced by the single photon collection efficiency in the nodes, and the repetition rate of the entanglement generation tries R, mainly limited by the communication time between the nodes. The entanglement generation rate is

given by

$$r = \eta_{\mathsf{aa}} R. \tag{5.2}$$

Here, both η_{aa} and R depend on the total link length L. In the following, we assume a two-node setup with a middle station halfway between the nodes, i.e., $L_1 = L_2 = L/2$.

The success probability of an entanglement generation try is given by

$$\eta_{\mathsf{aa}}(L) = \eta_{\mathsf{aa},L=0} 10^{-\alpha/10 \, L} = \mathcal{O}(e^{-L}), \tag{5.3}$$

where $\eta_{\mathsf{aa},L=0}$ denotes the success probability for a setup with a zero length link and approximates $5.0 \cdot 10^{-6}$ for the presented apparatus. This includes the photon collection efficiencies in both nodes after an excitation attempt (1.0% and 1.1%), the transmission of the MEMS switches (85%*), the efficiency of the frequency conversion devices (57%*), the single photon transmission efficiencies of the spectral filtering cavities (81%*), the fibre coupling to the single photon detectors (90%*), the single photon detector efficiencies (85%*), and the fraction of distinguishable Bell states of 2/4 (*these efficiencies should be included twice, thus quadratically). The attenuation rate in optical fibres is denoted by α in units of dB/km, which is significantly reduced using polarization-preserving quantum frequency conversion to telecom wavelength from 4.0 dB/km at 780 nm to 0.2 dB/km at 1517 nm.

The repetition rate of the entanglement generation tries equals

$$R(L) = \frac{1}{T} = \frac{1}{T_{L=0} + \frac{1}{2}L/(\frac{2}{3}c)} = \mathcal{O}(L^{-1}), \tag{5.4}$$

where T is the period of an entanglement generation try. The period of an entanglement generation try for a link with $L = 0$ is denoted by $T_{L=0}$ and equals 12 μs for the presented apparatus ($R(0) = 83.7$ kHz). This includes the duration of the initial state preparation (3 μs), the entanglement generation (200 ns), and the polarization gradient cooling per try to counteract the introduced heating during state preparation and entanglement generation (350 μs/40). The second term in the denominator corresponds to the communication times between the nodes and the middle station over optical fibres, where $\frac{2}{3}c$ approximates the speed of light in an optical fibre. The factor $\frac{1}{2}$ appears since in the implemented experimental sequences the electronic delay for the atomic readout is only applied after a successful heralding event (see Figure 5.4). This is *not* feasible when the two nodes are physically separated by a distance L and, effectively, reduces the entanglement generation rate by a factor up to 2 for a physical separation L compared to the rates presented in this work.

The observed entanglement generation rate, success probability, and repetition rate are listed for the different fibre length configurations in Table 5.2. Further, Figure 5.6 shows the modelled entanglement generation rate according to Eq. (5.2–5.4) and extrapolated to distances up to 100 km, together with the observed values of the entanglement generation rate. For $L < 54$ km the entanglement generation rate is mainly reduced by the rapidly decreasing repetition rate R, e.g., for $L = 0$ to 33 km, $R(L)$ drops by a factor of 8, while the success probability reduces by a factor 4.5. Only for distances $L > 54$ km the exponential dependence of the success probability outweighs the dependence of the repetition rate.

Note that the duty cycle of the experiment, approximately 1/2 for all fibre lengths, is not included in the entanglement generation rates presented in this section.

Table 5.2: **Observed entanglement generation rate for different fibre configurations.** Listed are the observed atom-atom entanglement generation rate r, success probability η_{aa}, and repetition rates R, for the different fibre link lengths L. The success probabilities include two-photon events in the full 208 ns hard-wired acceptance window, i.e., not conditioned on photon arrival time.

L (km)	r (s^{-1})	$\eta_{\mathsf{aa}} \cdot 10^6$	R (kHz)
6	1/8.9	3.7	30.8
11	1/15.0	3.1	21.6
23	1/39.1	1.9	13.3
33	1/84.5	1.2	9.7
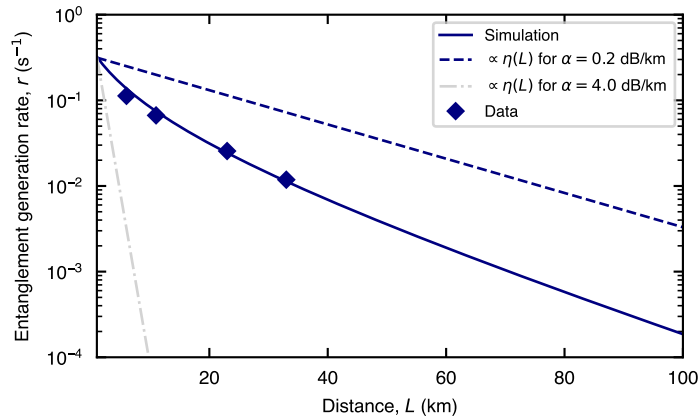
Figure 5.6: **Entanglement generation rate for varying link lengths.** The diamonds show the observed entanglement generation rates ($r = \eta_{\mathsf{aa}} \cdot R$) for $L = 6$, 11, 23, and 33 km. The blue solid line represents a calculation of the entanglement generation rate based on Eq. (5.2–5.4) and extrapolated up to $L = 100$ km. The dashed lines are proportional to the decay in success probability ($\propto \eta_{\mathsf{aa}}(L)$) for an attenuation rate in optical fibres of 0.2 dB/km at 1517 nm (blue dashed line) and 4.0 dB/km at 780 nm (gray dashed line) and hence indicate the reduced event rate originating solely from attenuation losses. The difference between the blue solid and dashed line originates from the reduced repetition rate $R(L)$ due to the longer communication times between the nodes and the middle station. For $L < 54$ km, the reduced repetition rate is the main contributor to the lower entanglement generation rate.

Figure 5.7: **Background characterization of the single-photon detection setup.** Counts per second (cps) registered by the four SNSPDs of the BSM setup for different fibre lengths L. Background introduced by the QFC devices is attenuated in the optical fibres (as are the signal pho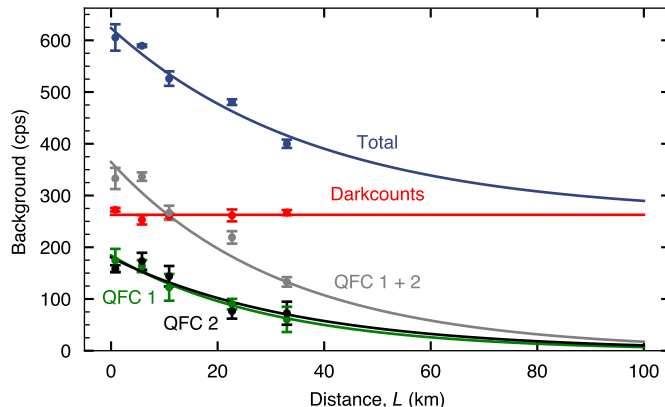tons). Detector darkcounts—which are not depending on the fibre length—are the dominant noise source for $L > 11$ km. The data are fitted with exponential decay functions to estimate the background counts for fibre lengths up to $L = 100$ km.

5.4   Characterization of atom-photon entanglement

Since the entanglement quality shared between the two nodes directly depends on the fidelity of the two entangled atom-photon pairs, we first individually characterize the atom-photon entanglement distribution between the nodes and the middle station. Here, the same fibre configurations and atomic readout times are used as during the atom-atom entanglement measurements that will be presented in Section 5.5, which are summarized in Table 5.1. Note that an high fidelity atomic state readout can only be made after an integer number of oscillation periods of the atom in the dipole trap (see Figure 2.17), which equals 14.3 and 17.8 μs for Node 1 and 2, respectively.

Characterization of photon detection noise

Background in the photon detection process reduces the fidelity of the observed entangled atom-photon and atom-atom states, as discussed in Section 4.5.1. QFC induced background and detector darkcounts are the main noise sources—Figure 5.7 shows a noise characterization for the different fibre configurations L. The QFC induced noise is, similarly to the signal, attenuated in the long fibres. In the shortest fibre configuration, the QFC devices in Node 1 and 2 introduce a background of around 160 and 170 cps, respectively. The four detectors introduce a total background of 270 cps, which becomes the dominant source of background for fibre lengths of $L > 11$ km.

Atom-photon entanglement fidelities

The atom-photon entanglement distribution from Node 1 and 2 to the middle station was analysed in the different fibre configurations following the methods presented in Section 2.3. Therefore, the photon polarization was observed in two bases, H/V (horizontal/vertical) and D/A (diagonal/anti-diagonal), i.e., X and Y, while the atomic analysis angle was rotated in steps

91

Table 5.3: **Observed atom-photon entanglement fidelities for different fibre lengths.** Listed are the measured atom-photon entanglement fidelities $\mathcal{F}_{ap_1}$ and $\mathcal{F}_{ap_2}$ for different fibre lengths for Node 1 and 2, respectively.

L_1 (km)	$\mathcal{F}_{ap_1}$	L_2 (km)	$\mathcal{F}_{ap_2}$
2.6	0.941(5)	3.3	0.911(6)
5.4	0.915(7)		
11.3	0.858(6)	11.4	0.821(8)
16.5	0.817(8)	16.6	0.767(8)

of 22.5° over angles including these bases. The atomic readout time was delayed to allow for two-way communication to the middle station for each node over the respective fibre length. Figure 5.8 shows the atom-photon state correlations for different fibre lengths L_1 and L_2. For short fibre links, the visibility is limited by the atomic state readout and entanglement generation fidelity. For longer fibre lengths, the observed visibility drops due to decoherence of the atomic state originating from magnetic field fluctuations along the guiding field and the position-dependent dephasing.

The atom-photon characterization measurements revealed a phase shift between the atomic states $|H\rangle$ and $|V\rangle$ states for both nodes. The phase shift is zero for immediate atomic readout after atom-photon entanglement generation and increased linearly with the atomic readout time by approximately 36 and 32 degrees per 100 μs for Node 1 and 2, see Figure 5.9. The origin of the shift could not be determined. Effectively, for the chosen measurement angles, the phase shift reduces the observed atom-photon state visibility in the D/A basis. Introducing a similar phase shift to the atomic readout light, however, cancels the shift and increases the observed visibilities. The readout light phase shift was set with an accuracy of ± 10 degrees only for the atom-photon state correlation measurements for the measurements shown in Figure 5.8. During the atom-atom entanglement measurements presented in the next section, the atomic readout light phase was not corrected. The phase cancels for the atom-atom state since the linear time dependence of the shift and readout times of the two atoms were comparable.

The observed atom-photon state fidelities are estimated from the visibilities following Eq. (2.14) and listed in Table 5.3. To avoid underestimation of the atom-photon entanglement fidelity due to the phase shift, the fidelities are estimated based on the observed average visibilities of the states $|H\rangle$ and $|V\rangle$ only.

5.5 Results

The performance of the atom-atom entanglement generation is evaluated in two steps. First, by analysing the atom-atom entanglement generation over a relatively short fibre link length of $L = 6$ km, as described in Section 5.5.1. This configuration has a higher entanglement generation rate and hence allows for a detailed analysis of the two-photon interference quality and a more thorough analysis of the generated entangled state. Thereafter, in Section 5.5.2, we
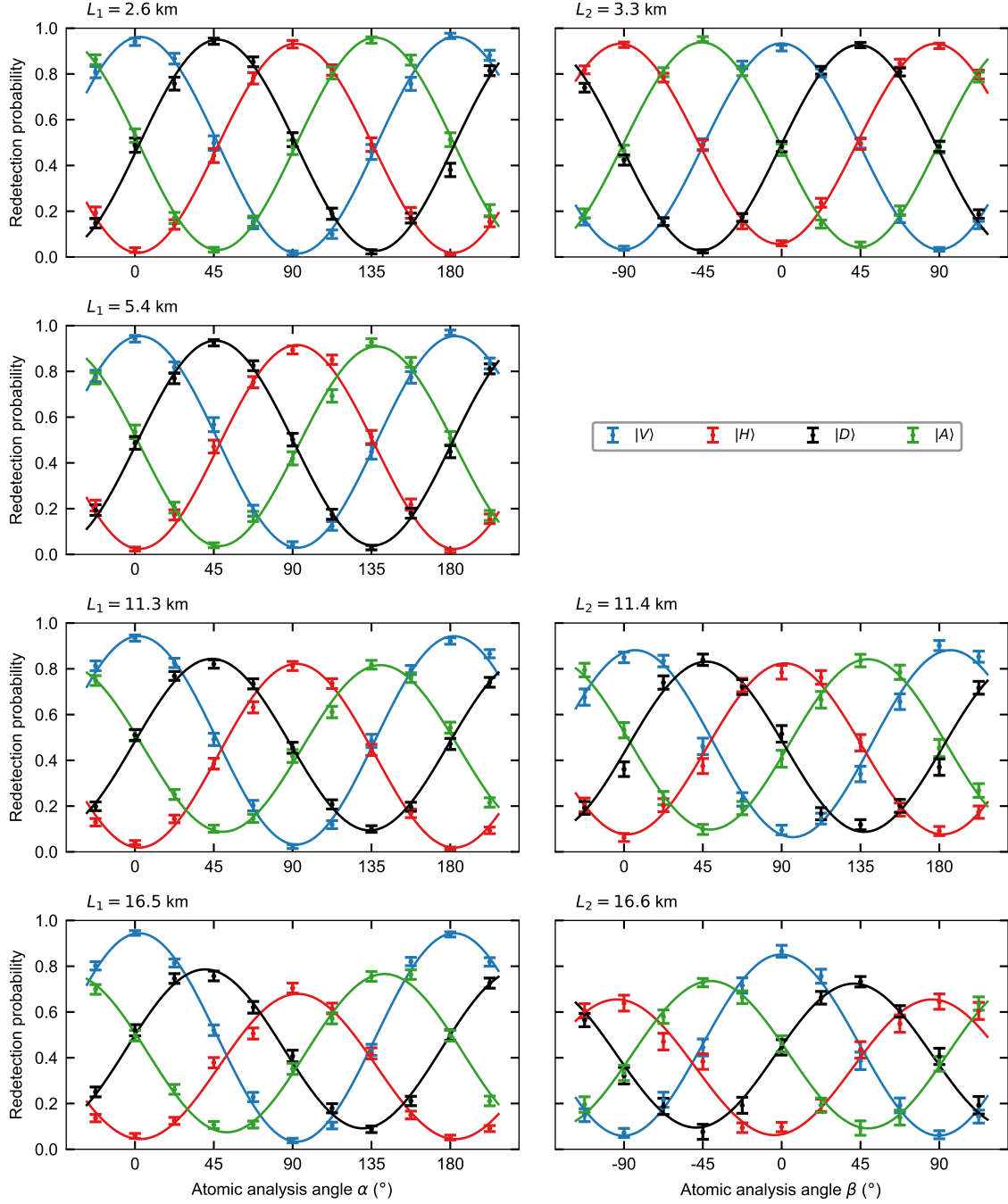
Figure 5.8: **Atom-photon entanglement distribution at telecom wavelength.** Characterization of atom-photon entanglement distribution to the middle station from Node 1 (left side panels) and Node 2 (right side panels). The observed atom-photon state fidelities are listed in Table 5.3 and plotted over distance in Figure 5.14. The fibre lengths and atomic readout times are equal to the atom-atom entanglement generation and analysis measurements presented in Section 5.5, including an atomic readout delay to allow for two-way communication with the middle station.
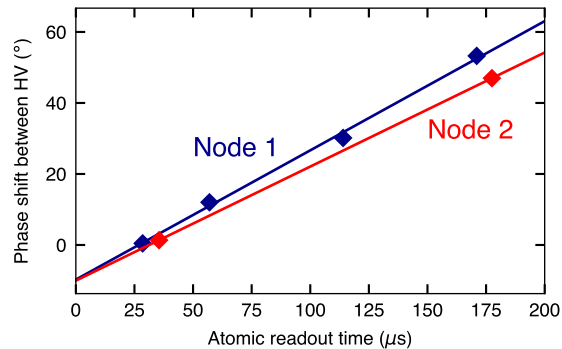
Figure 5.9: **Accumulation of an atomic phase shift over time.** Observation of a linearly increasing phase shift between the states $|H\rangle$ and $|V\rangle$ when delaying the atomic readout time. The phase shift can be compensated for by introducing a similar shift to the atomic readout light. Since the phase shifts in the nodes are similar, they cancel out for the atom-atom state.

study the influence of longer fibre links on the observed atom-atom state fidelity by measuring state correlations in three bases for fibre link lengths up to $L = 33$ km.

5.5.1 Entangling atoms using telecom photons

The entanglement distribution process is first evaluated in a fibre configuration of $L = 6$ km. This configurations has a relatively high entanglement generation rate of $r = 1/8.9$ s^{-1} for detection events in the full hard-wired coincidence window. Hence, considering an experimental duty cycle of approximately half, we observed $N = 10\,290$ entanglement generation events within 54 h.

Signal-to-noise ratio

Detector dark-counts and anti-Stokes Raman noise originating from the two QFC devices introduce background, where the latter depends on the fibre length. For the $L = 6$ km configuration, the QFC induced noise is approximately 160 and 170 cps registered at the middle station for light from Node 1 and 2, respectively (see Figure 5.7). To reduce the influence of the background on the observed state fidelity, a 70 ns acceptance window is applied during the data evaluation, as shown in Figure 5.10. This results in a signal-to-noise ratio (SNR) of 58 (65) for detecting a single photon after an entanglement generation try in Node 1 (Node 2), which is significantly higher than SNR reported in Chapter 4 by selecting a more favourable pump-signal frequency combination with respect to the Raman background (see Figure 4.4). For the coincidence detections, this leads to a SNR of 48 while accepting $N = 6\,660$ events (65% of the recorded events). Note that the two-node setup suffers background from two QFC devices, in contrast to one QFC device for the experiments presented in the previous chapter.

Two-photon interference contrast

The temporal overlap of the photons originating from the nodes is optimized by tuning the excitation pulse shapes and timings. More specifically, the pulse shapes are matched by using identical experimental equipment for the excitation pulse generation and the timings are optimized by introducing electronic delay lines. Finally, the overlap of the photons exceeds 0.98,
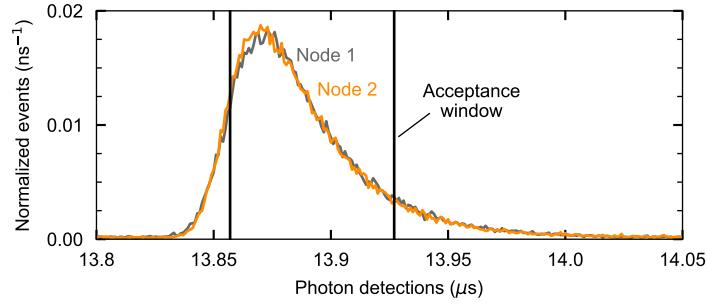
Figure 5.10: **Temporal shape of telecom photons for $L = 6$ km.** Detection time histogram of the photons originating from Node 1 and 2 relative to the time of excitation in Node 1. For the indicated 70 ns long acceptance window, we observe a SNR of 58 and 65 for Node 1 and 2, respectively. The temporal overlap of the two photons is crucial for high contrast two-photon interference and exceeds 0.98.

which is determined by individual measurements of the photon detection time histograms for photons originating from Node 1 and 2, as shown in Figure 5.10. Moreover, a unity spatial overlap is guaranteed by using a fibre beamsplitter and spectral indistinguishability is achieved by using the same transition in rubidium for the atom-photon entanglement generation process.

The relative occurrence of wrong detector coincidences quantifies the two-photon interference contrast of the converted photons, as described before in Section 2.4.3. Therefore, the detector combinations are grouped in D_+ and D_-, which herald the Bell states $|\Psi^+\rangle$ and $|\Psi^-\rangle$, respectively, and the group $D_\varnothing$, containing coincidences that should not occur for perfectly interfering, fully-unpolarised photons. The latter are discarded in the state fidelity analysis, however, the relative occurrence of these events is used to quantify the two-photon interference contrast via Eq. (2.21). For temporally well overlapping photons, but without background correction, this results in an interference contrast of $C_{\mathsf{intf}} = 0.955(7)$. Correcting for photonic background counts taking into account a SNR of 48 results in $C_{\mathsf{intf-bg}} = C_{\mathsf{intf}}(\mathrm{SNR} + 1)/\mathrm{SNR} = 0.975(7)$.

To verify this method, we additionally evaluate the contrast of not interfering photons, as visualized in Figure 5.11. This is done by analysing coincidence detections of two photons originating from distinct entanglement generation tries. In this way, the photons did not interfere due to temporally not overlapping photon wave-packets; where the time difference between two photon wave-packets is defined as $\Delta\tau$. We find that not interfering photons ($\Delta\tau \neq 0$) have an interference contrast of 0.001(5). Note that the horizontal spacing of the measurement times in Figure 5.11 equal the repetition rate of the entanglement generation tries during an excitation burst. The number of coincidences for times $\Delta\tau \neq 0$ is higher since they also include events where both detected photons originated from one trap, which has a very low probability for $\Delta\tau = 0$.

Atom-atom entanglement fidelity

The atom-atom entanglement is evaluated following the methods presented in Section 2.4.4. Accordingly, we measured the atomic spin states in the two linear bases, X and Y. For this, the polarization analysis angle in Node 2 was set to $\beta = 0° = X$ and $\beta = 45° = Y$, while the analysis angle in Node 1 was varied over $90°$ in steps of $22.5°$ starting from $\alpha = 0° = X$ and $\alpha = 45° = Y$, respectively. The atom in Node 1 (Node 2) was analysed at $t_1 = 28.5$ μs ($t_2 =$
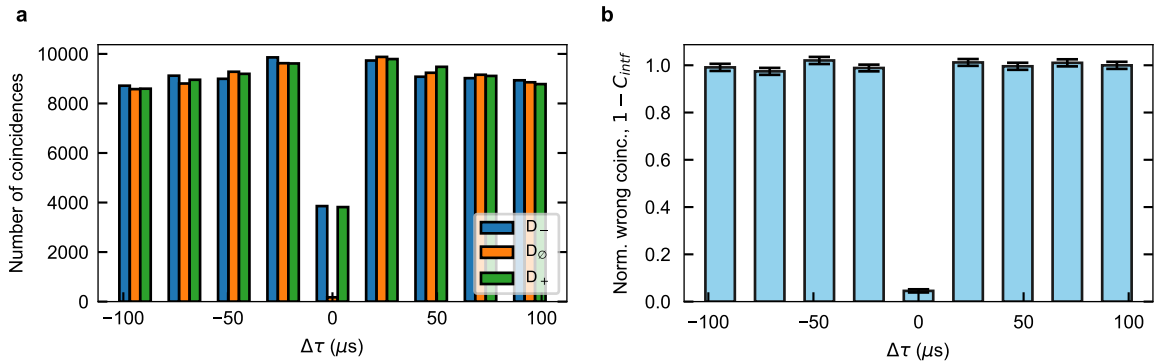
Figure 5.11: **Characterization of the two-photon interference contrast for $L = 6$ km.**
Two-photon interference based on the Hong-Ou-Mandel effect for various time difference between
the two photon wave-packets ($\Delta\tau$). **a**, The number of coincidences per detection group. **b**,
Normalized number of wrong coincidences ($1-C_{\mathsf{intf}}$).

35.5 μs) after the respective excitation pulse. The resulting atomic state correlation probabilities
$P_{\mathsf{corr}} = (N_{\uparrow\uparrow}^{\alpha,\beta} + N_{\downarrow\downarrow}^{\alpha,\beta})/N^{\alpha,\beta}$ and anti-correlation probabilities $P_{\mathsf{acorr}} = (N_{\uparrow\downarrow}^{\alpha,\beta} + N_{\downarrow\uparrow}^{\alpha,\beta})/N^{\alpha,\beta}$ are
shown in Figure 5.12. The data are fitted with sinusoidal curves resulting in average visibilities
of $\bar{V} = 0.804(20)$ for $|\Psi^-\rangle$ and $\bar{V} = 0.784(23)$ for $|\Psi^+\rangle$.

We estimate the atom-atom state fidelity using Eq. (2.23), considering that the third ground
state ($5^2\mathrm{S}_{1/2}|\mathrm{F} = 1, m_F = 0\rangle$) can be populated. Hence, a lower bound on the fidelity is given
by $\mathcal{F} \geq \frac{1}{9} + \frac{8}{9}\bar{V} = 0.826(18)$ for $|\Psi^-\rangle$ and $0.806(20)$ for $|\Psi^+\rangle$, relative to a maximally entangled
state.

CHSH Bell test

The chosen analysis angles also allow to evaluate the Clauser-Horne-Shimony-Holt (CHSH) S
value [123] for the settings $\alpha = 22.5°$, $\beta = 0°$; $\alpha' = 67.5°$, $\beta = 0°$; $\alpha' = 67.5°$, $\beta = 45°$; and
$\alpha'' = 112.5°$, $\beta' = 45°$, whereby α'' replaces $\alpha = 22.5°$. This results in an observed value of
$S = 2.244(63)$, violating the limit of 2 with 3.9σ.

Influence filtering photon arrival times

Introducing a 70 ns long photon acceptance window during the data evaluation increased the
quality of the observed atom-atom state in two ways. First, by reducing the relative number of
recorded background counts, i.e., increasing the SNR, which favours a short acceptance window
around the peak of the photon detection time. Second, by rejecting early detection events that
have a higher probability of carrying which-path information (see Section 2.4.3).

To quantify the influence of the time-filtering, we evaluated the systems performance when
accepting all recorded events in the 208 ns long hard-wired detection window. This leads to a
SNR and interference contrast of 22 and 0.895(8), respectively. For the atom-atom entanglement
fidelity, resulting in an average observed fidelity for the states $|\Psi^\pm\rangle$ of 0.772(10). Time-filtering
thus lifts the fidelity of the observed atom-atom state by 4.4 percent points.
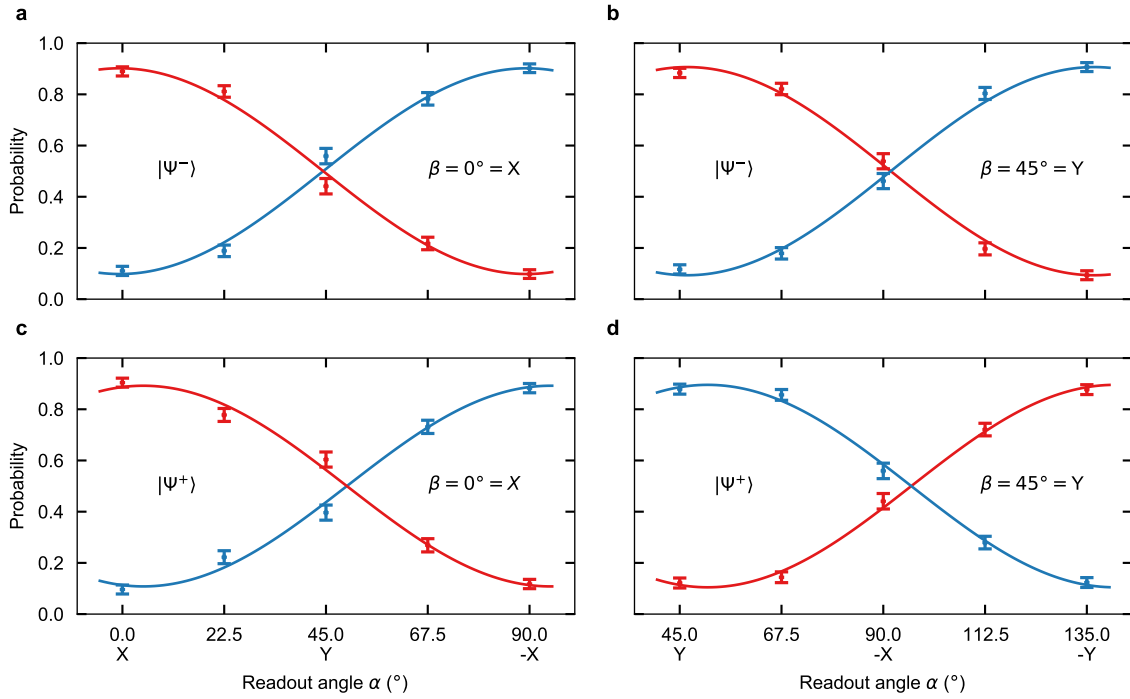
Figure 5.12: **Observation of atom-atom entanglement for $L = 6$ km.** Atom-atom state correlations for the $|\Psi^-\rangle$ (**a**, **b**) and $|\Psi^+\rangle$ (**c**, **d**) states. The correlation probability of the measurement outcome in the nodes is shown in blue, while the anti-correlation probabilities are marked in red. The data are fitted with sinusoidal functions resulting in an estimated fidelity for $|\Psi^-\rangle$ and $|\Psi^+\rangle$ relative to a maximally entangled state of 0.826(18) and 0.806(20), respectively. Shown are a total of $N = 6\,660$ entanglement generation events.
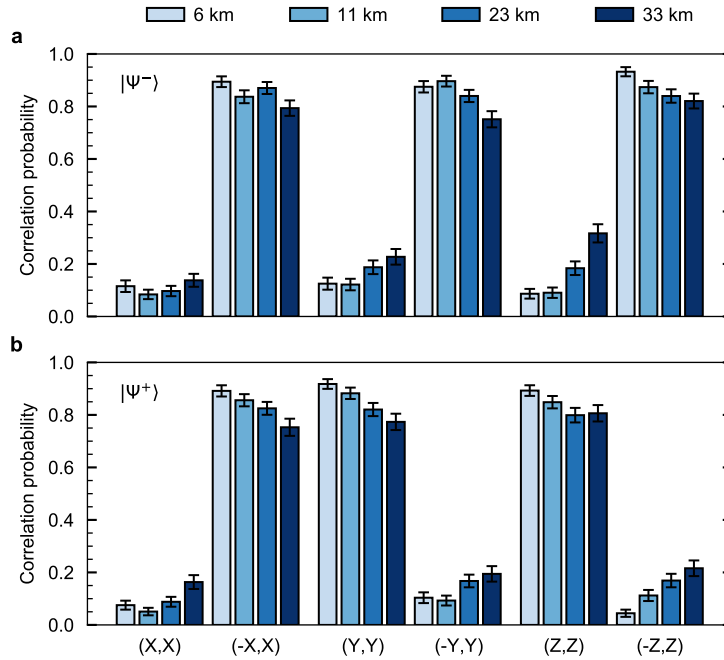
Figure 5.13: **Observation of atom-atom entanglement generated over long fibre links.**
Correlations between the measurement results when analysing the generated atom-atom Bell
states $|\Psi^-\rangle$ (**a**) and $|\Psi^+\rangle$ (**b**) for various link lengths. For each link, the states were analysed
in 3 conjugate bases (Node 1, Node 2), whereby the correlation probability of the measurement
result in the nodes equals $P_{\text{corr}} = (N_{\uparrow\uparrow} + N_{\downarrow\downarrow})/(N_{\uparrow\uparrow} + N_{\uparrow\downarrow} + N_{\downarrow\uparrow} + N_{\downarrow\downarrow})$. For the different fibre
lengths (short to long) $N = 4\,281$, $4\,271$, $4\,153$, and $3\,022$ entanglement events were recorded
within a measurement time of 11, 65, 97, and 175 h. Of these events, 62–72% was within the
two-photon coincidence acceptance window, resulting in 185–225 events per data-point.

5.5.2 Entangling atoms over up to 33 km fibre

To determine the effect of long fibre links, we performed a series of measurements generating
and observing atom-atom entanglement in fibre configurations with a length $L = 6$, 11, 23, and
33 km.

Observed atom-atom entanglement fidelities

The entanglement fidelity relative to maximally entangled states was analysed by measurements
along three bases (X, Y, and Z). Figure 5.13 shows the probability of correlated measurement
outcomes in the nodes for each measurement setting combination and fibre configuration.

The fidelity of the observed states is estimated by first determining the contrast in the
three measurement bases independently. This is done by taking the absolute difference of the
two measured correlation probabilities, $E_k = |P_{k,k} - P_{-k,k}|$ for $k \in \{X, Y, Z\}$, from which the
average contrast is computed as $\bar{E} = (E_X + E_Y + E_Z)/3$. The observed (average) contrasts
are listed in Table 5.4. When averaging over the observed states $|\Psi^\pm\rangle$—which show within our
measurement precision similar visibilities—and again assuming the 3×3 state space, this results
in a lower bound on the fidelities $\mathcal{F} \geq 0.830(10)$, $0.799(11)$, $0.719(12)$, and $0.622(15)$ relative to
maximally entangled states for $L = 6$, 11, 23, and 33 km, respectively. The estimated fidelity

Table 5.4: **List of observed atom-atom entanglement contrasts, average contrasts, and fidelities.** The observed entanglement contrast in three bases and the estimated fidelity for the $|\Psi^{\pm}\rangle$ states. The fidelities ($\mathcal{F}$) are computed from the average contrast ($\bar{E}$) according to Eq. (2.23).

L(km)	E_X	E_Y	E_Z	$\bar{E}$	$\mathcal{F}$
			$|\Psi^-\rangle$		
6	0.779(30)	0.750(32)	0.846(25)	0.792(17)	0.814(15)
11	0.753(30)	0.775(30)	0.783(31)	0.770(18)	0.796(16)
23	0.774(30)	0.657(34)	0.654(36)	0.695(19)	0.729(17)
33	0.666(38)	0.524(43)	0.504(45)	0.565(24)	0.613(21)
			$|\Psi^+\rangle$		
6	0.816(27)	0.814(28)	0.848(24)	0.826(15)	0.845(13)
11	0.805(27)	0.790(29)	0.736(32)	0.777(17)	0.802(15)
23	0.740(30)	0.646(35)	0.638(37)	0.675(20)	0.711(18)
33	0.590(42)	0.579(43)	0.590(43)	0.586(25)	0.632(22)

for the 6 km fibre configuration is in good agreement with the fidelity estimated from the fringe measurements in two bases presented in Section 5.5.1. Moreover, all observed fidelities clearly exceed the bound of 0.5 and hence witness an entangled state.

Decoherence of the atomic states

The observed fidelities are plotted in dependence of the fibre link length in Figure 5.14. Furthermore, for completeness, the atom-photon entanglement characterization measurements of Section 5.4 are shown. The solid lines are based on simulations of the generation and evolution of the two atom-photon states (see Section 2.5), from which the atom-atom state fidelity $\mathcal{F}(L)$ is computed. We estimate the visibility of the atom-atom state by the product of the two atom-photon visibilities and the interference contrast of the BSM. Evidently, decoherence of the atomic states dominates the loss in fidelity for longer fibre links. For $L = 33$ km, the states were analysed 171 and 178 μs after excitation in Node 1 and 2, respectively, which approaches the coherence time of the states. The SNR is more robust to an increase in fibre length since both the single photons as well as the QFC background are attenuated in the long links. A minor reduction in SNR (42 for $L = 33$ km) is explained by relatively more detector dark-counts and can be improved by installing better detectors or slightly reducing the bias-current of the detectors.

To verify that the memory decoherence limits the loss in fidelity for long fibre links, we
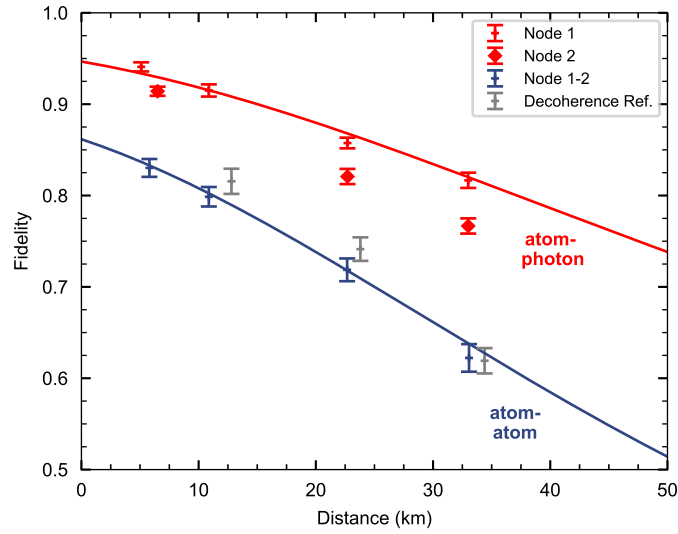
Figure 5.14: **Observed entanglement fidelity for various link lengths.** Overview of the observed atom-atom fidelities for different fibre configurations (blue). For completeness, the observed atom-photon fidelities of the nodes (red), with $L = 2 \cdot L_i$, are given. The solid lines are simulations based on a model taking into account the decoherence of the atomic memories. The gray points are reference measurements of the atom-atom state decoherence, without long fibres, but with corresponding readout delay.

performed a series of measurements without additional fibres inserted, however, with the memory readout times electronically delayed fitting the photon travel time through the long fibre links. The observed fidelities are shown in gray in Figure 5.14 at $L = \frac{2}{3}c(t_1 + t_2)/2$ (matching the two-way communication time to the middle station for distance L) and show, within the measurement accuracy, no difference in observed fidelity compared to the configuration with long fibres.

Chapter 6

Conclusion and Outlook

In this work we employed neutral single-atoms for quantum networking experiments. Here we list potential upgrades to the set-up and propose future experiments, as well as a potential research directions for the realisation of neutral single-atoms based quantum networks. We finish with a general conclusion of the work.

Suburban quantum network link

Demonstration of heralded atom-atom entanglement over tens of kilometres of spooled fibres, as is done in this work, paves the way towards the realisation of quantum network links with field employed fibres and increased line-of-sight separation between the nodes. In this respect, an appealing route is to realise a quantum link between the LMU in Munich and the Max-Planck-Institut für Quantenoptik (MPQ) in Garching—the two home institutes of our research group which are located 14 km line-of-sight apart. Below we list several ways to realise such a suburban quantum network link. Note that the expected fidelities do not (yet) meet the demanding requirements for DI-QKD.

Entanglement swapping.—Most straightforward is re-location of one of the current nodes to the MPQ and generate atom-atom entanglement via the methods presented in Chapter 5. The expected entanglement fidelity and rate are accurately estimated from the results of this work and will primarily depend on the length of the fibre connecting the institutes and the location of the middle station. Assuming a fibre length of 28 km and a middle station halfway the connection, we expect to observe a fidelity of $\mathcal{F}_{\mathsf{aa}} = 65\%$ and an entanglement generation rate of $1/226 \text{ s}^{-1}$. However, in case a middle station is not realisable and the BSM is located in the vicinity of one of the nodes, the entanglement generation rate drops to $1/452 \text{ s}^{-1}$ due to a doubling of classical communication times.

Cavity-enhanced interaction.—Another option is to generate heralded entanglement between an atom stored in one of our set-ups at the LMU and an atom in a cavity-based single-atom trap set-up developed by the Rempe group at the MPQ. This could be realised by generating atom-photon entanglement at the LMU and transferring this photon to the MPQ where the polarisation state is stored in a heralded single-atom quantum memory, for example, employing a crossed-cavity set-up [60]. For this, QFC of the photons at the LMU to telecom wavelength mitigates the attenuation losses in the optical fibre connecting the institutes while a second step of QFC at the MPQ allows to compensate for the initial frequency mismatch of the two rubidium quantum memories. Conservative estimates result in expected entanglement fidelities of $\mathcal{F}_{\mathsf{aa}} = 78\%$ and entanglement generation rates of $1/20 \text{ s}^{-1}$.

Looped field employed fibres.—Missing in the experiments presented in this work compared to quantum network links with a large physical node separation is the use of long field employed fibres. An intermediate goal could be the realisation of atom-atom entanglement over looped field employed fibres, as realised for post-selected entanglement generation in [96]. In this way, the effect of, e.g., polarisation drifts could be investigated without re-location of the set-ups.

Quantum link efficiency

In order to evaluate the performance of entanglement generation in future quantum networks the so-called quantum link efficiency was introduced recently [58], defined as

$$\eta_{\text{link}} = r_{\text{ent}}/r_{\text{dec}}, \tag{6.1}$$

where r_{ent} equals the entanglement generation rate and r_{dec} equals the entanglement decay rate. It describes how efficiently one can use entanglement as a resource in future quantum networks. Ideally, the link efficiency should exceed one, i.e., entanglement is available on demand as it is generated faster than it decays. However, the link efficiency decays rapidly with the link length due to both the exponential decrease of the signal detection probability, but, even more dominantly for the link lengths realised in this thesis, also due to the waiting times for classical communication between the nodes. In this work, the link efficiency for link lengths of 6 to 33 km was at the 10^{-5} to 10^{-6} level, mainly limited by the low photon collection efficiency, relatively short coherence times, and long fibre links. An increase of the link efficiency could be achieved by improving the memory storage time, increasing the entanglement generation rate, and parallelisation of the entanglement generation tries, which is discussed below in more detail.

Memory storage time

For the used apparatus, atomic state decoherence limits the observed atom-photon and atom-atom state fidelity for entanglement distribution over long fibre links, as predicted in Chapter 2 and experimentally verified in Chapters 4 and 5. In particular, magnetic field noise and longitudinal field components of the strongly focussed dipole trap beam reduce the memory storage time. The memory storage time can be prolonged in two steps, as we recently demonstrated [127]. First, adiabatically ramping down the dipole trap reduces the longitudinal field components— which are proportional to the dipole trap power and, in our system, introduce effective magnetic fields along the y-axis. Applying a bias magnetic field along the z-axis mitigates the residual effect of the longitudinal fields. Second, by coherently transferring the memory into another qubit encoding, the sensitivity to magnetic fields along the z-axis is reduced by more than a factor 500 [63].

The above allowed to increase the memory coherence time T_2 from 330 μs to more than 7 ms, allowing for entanglement distribution without significant memory decoherence over 101 km optical fibre [127]. Implementation of a spin-echo could potentially further increase the coherence time. Next is to improve the efficiency of the coherent state transfer, which currently equals $c_{\text{st}} = 0.97$. This is crucial since the fidelity of the atom-atom state generated in the entanglement swapping protocol presented here will depend on the state transfer efficiency as $\mathcal{F}_{\text{aa}} \propto c_{\text{st}}^4$.

Another option to mitigate the longitudinal field components of the tightly focussed dipole trap beam is the introduction of a second, counter-propagating dipole trap beam, which would cancel out the longitudinal fields. Challenging here is to precisely match the beam parameters, in particular, to achieve a good overlap of the two foci which requires alignment with an accuracy much smaller than the beam waist. Realisation of a standing wave would make the optical dipole

trap ramping obsolete, which would improve entanglement generation rates. Furthermore, and maybe even more interesting, it also allows for the storage of additional atoms.

Entanglement generation rate

Efficient employment of entanglement as a resource in quantum networks requires entanglement generation at high rates. A fitting example here is the proof-of-concept demonstration of DI-QKD presented in Chapter 3, where the system can generate a key with finite-key security only after several months of quantum communication—too long for any practical cryptographic application.

The entanglement generation rate of our system can be increased by an order of magnitude by applying several incremental improvements, such as, the installation of more efficient single-photon detectors and refining the entanglement generation process to allow for a higher excitation probability as well as a relaxation of the current time-filtering requirements. Moreover, extensive changes to the set-up, including the installation of a cavity, could increase the atom-atom rate by another two orders of magnitude, as photon collection efficiencies up to 11% have been demonstrated [60]. However, the entanglement generation efficiency cannot be increased arbitrarily high and hence it will be mandatory to parallelize the entanglement generation process to regain scalability, as will be discussed below.

Single-atom based quantum networks

Quantum networks are envisioned to facilitate the distribution of high-quality entangled states between distant as well as non-neighbouring network nodes. For this, the employed quantum systems in the nodes should enable for the implementation of quantum repeater protocols [208], entanglement distillation [71], and parallelisation of the entanglement generation process—which all three require multiple physical qubits per network node. Employing neutral single-atoms, the number of individually addressable atoms per node can be scaled up by using arrays of dipole traps [80, 82, 209] or by the generation of an optical lattice [208]. Together with atomic excitation to Rydberg states to introduce local interactions between atoms and facilitate two-qubit gates [85], this provides a promising platform to realise quantum networks.

Employing a single fibre channel connecting two nodes, parallelisation of the entanglement generation tries requires either efficient coupling to that optical fibre for multiple atoms or a communication- and memory-qubit architecture, e.g., an individual communication-atom that is efficiently coupled to the fibre which state could be transferred to nearby memory-atoms. In such an architecture, Rydberg gates could transfer states between neighbouring atoms or, to provide scalability, cavity-mediated interactions could provide any-to-any connectivity within a (multidimensional) atom array [210, 211].

To further boost efficiencies in the entanglement distribution process, non-destructive photon detection could prove valuable [154]. For example, by flagging the absence of a photon at the beginning of an optical channel, this would overcome waiting times for heralding signals that would not arrive in the first place.

Moreover, the QFC devices demonstrated in this work could provide an efficient telecom wavelength interface. Not only mitigating attenuation losses in long optical fibres, but also enabling to match operation frequencies of quantum memories.

Conclusion

Our results show how to harness the ultimate quantum advantage for secure communications and demonstrate crucial properties for neutral single-atoms to serve in quantum networks. In particular, the realisation of a proof-of-concept DI-QKD protocol employing high-quality entanglement of single-atoms indicates that state-of-the-art quantum network links can utilize the ultimate quantum advantage for secure communications. Even if it is still a long way to go; when the future quantum repeater based quantum networks provide the key resource, i.e., shared entanglement, DI-QKD—as presented in this thesis—will become the standard for secure key exchange. Moreover, thanks to the record high external device efficiency of 57% for the polarisation-preserving QFC and improved collection optics for the atomic fluorescence, we generated heralded entanglement between two atomic quantum memories over fibre links with a length as long as 33 km. Making realistic improvements on the memory coherence time and entanglement generation rate will enable to entangle two atomic quantum memories with a fidelity better than 80% over fibre lengths up to 100 km. In summary, this work presents a major step towards the goal of ultimate secure communication based solely on quantum physics and paves the way towards the realisation of long-distance quantum network links.

Appendix A

Physical Constants and Properties ^{87}Rb

Physical constants and relevant properties of ^{87}Rb. The rubidium data originates from [212].

Table A.1: **Physical constants.**

constant	description	value
$\hbar = \frac{h}{2\pi}$	reduced Planck constant	$1.054571726 \times 10^{-34}$ J s
c	speed of light in vacuum	2.99792458×10^{8} m s^{-1}
μ_0	permeability of free space	$1.25663770614 \times 10^{-6}$ N A^{-2}
$\epsilon_0 = \frac{1}{c^2\mu_0}$	permittivity of free space	$8.8541878176 \times 10^{-12}$ F m^{-1}
e	elementary charge	$1.602176565 \times 10^{-19}$ C
u	atomic mass unit	$1.660538921 \times 10^{-27}$ kg
k_B	Boltzmann constant	$1.38064852 \times 10^{-23}$ m^2 kg s^{-2} K^{-1}

Table A.2: **Atomic properties ^{87}Rb.**

| constant	description	value
Z	atomic number	37
m	mass	$86.90918020 \times u$
I	nuclear spin	3/2
τ_n	nuclear lifetime	4.88×10^{10} yr
E_0	ground state energy	4.177127 eV
	ionisation threshold	296.817 nm
Γ_{D_1}	decay rate D_1-transition	$2\pi \times 5.7500$ MHz
τ_{D_1}	lifetime excited state 5^2P$_{1/2}$	27.70 ns
d_{D_1}	dipole matrix element D_1-transition	2.537×10^{-29} C m
λ_{D_1}	wavelength D_1-transition	794.979 nm
Γ_{D_2}	decay rate D_2-transition	$2\pi \times 6.0666$ MHz
τ_{D_2}	lifetime excited state 5^2P$_{3/2}$	26.24 ns
d_{D_2}	dipole matrix element D_2-transition	3.584×10^{-29} C m
λ_{D_2}	wavelength D_2-transition	780.241 nm
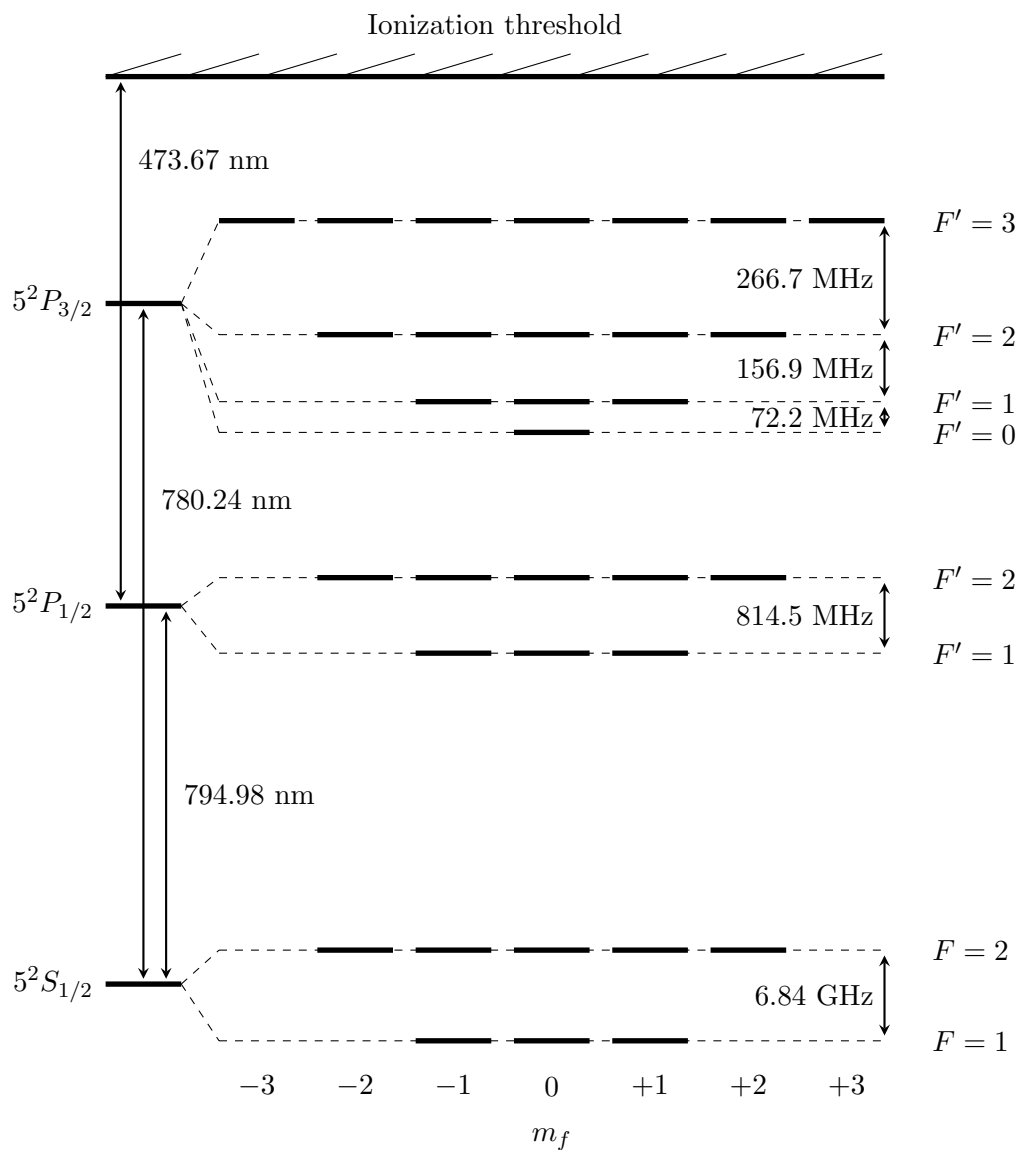
Figure A.1: **Energy level diagram [87]Rb.** The relevant energy levels of rubidium for this work.

Appendix B

Definition of the Polarization and Atomic States

For the coordinate system, photonic polarisation states, and atomic states we follow the definitions in [106], which are are summarised here.

Photonic polarisation

The definitions of the polarisation of the photonic states are listed in Table B.1. The polarisation states are defined as L for circular right-handed polarisation, R for circular left-handed polarisation, H for linear polarisation parallel to the surface of the optical table, V for linear polarisation vertical to the optical table, D for linear polarisation rotated $45°$ right-hand side in propoagation direction with respect to V, and A for linear polarisation rotated $45°$ left-hand side in propagation direction with respect to V.

Atomic states

The qubit is encoded in the Zeeman states $F = 1$, $m_F = \pm 1$ of the $5^2\mathrm{S}_{1/2}$ ground state of rubidium with the z-axis as quantization axis and $|1, -1\rangle = |\downarrow\rangle_z$ and $|1, +1\rangle = |\uparrow\rangle_z$ defined as eigenvectors to the Pauli matrix $\hat{\sigma}_z$. Thereby defining the qubit in the eigenvectors $\hat{\sigma}_y$ and $\hat{\sigma}_x$ as listed in Table B.2.

Entangled atom-photon state

The definitions in Tables B.1 and B.2 allow to write the entangled atom-photon state (Eq. (2.10)) in three conjugate bases as

$$
\begin{aligned}
|\Psi\rangle_{\mathsf{ap}} &= \frac{1}{\sqrt{2}} |\downarrow\rangle_z |L\rangle + |\uparrow\rangle_z |R\rangle \\
&= \frac{1}{\sqrt{2}} |\downarrow\rangle_x |H\rangle + |\uparrow\rangle_x |V\rangle \\
&= \frac{1}{\sqrt{2}} |\downarrow\rangle_y |D\rangle + |\uparrow\rangle_y |A\rangle.
\end{aligned}
\tag{B.1}
$$

Table B.1: **Definition of the photonic polarisation states.**

polarisation state	composition in $|\sigma^\pm\rangle$	E-field along the z-axis
$|L\rangle$	$|\sigma^+\rangle$	$\frac{1}{\sqrt{2}}\|E\| \begin{bmatrix} e^{-i\pi/2} \\ 1 \\ 0 \end{bmatrix} e^{i(kz-\omega t)}$
$|R\rangle$	$|\sigma^-\rangle$	$\frac{1}{\sqrt{2}}\|E\| \begin{bmatrix} e^{i\pi/2} \\ 1 \\ 0 \end{bmatrix} e^{i(kz-\omega t)}$
$|H\rangle$	$\frac{i}{\sqrt{2}}(|\sigma^+\rangle - |\sigma^-\rangle)$	$\|E\| \begin{bmatrix} 1 \\ 0 \\ 0 \end{bmatrix} e^{i(kz-\omega t)}$
$|V\rangle$	$\frac{1}{\sqrt{2}}(|\sigma^+\rangle + |\sigma^-\rangle)$	$\|E\| \begin{bmatrix} 0 \\ 1 \\ 0 \end{bmatrix} e^{i(kz-\omega t)}$
$|D\rangle$	$\frac{1}{\sqrt{2}}e^{-i\pi/4}(|\sigma^+\rangle_z + i\,|\sigma^-\rangle)$	$\frac{1}{\sqrt{2}}\|E\| \begin{bmatrix} -1 \\ 1 \\ 0 \end{bmatrix} e^{i(kz-\omega t)}$
$|A\rangle$	$\frac{1}{\sqrt{2}}e^{i\pi/4}(|\sigma^+\rangle - i\,|\sigma^-\rangle)$	$\frac{1}{\sqrt{2}}\|E\| \begin{bmatrix} 1 \\ 1 \\ 0 \end{bmatrix} e^{i(kz-\omega t)}$

Table B.2: **Atomic qubit state definitions.** Relation between the qubit states in x, y, and z basis and the atomic Zeeman states denoted as $|F, m_F\rangle_z$.

qubit state	in qubit z states	in $m_{F,z}$ states
$|\downarrow\rangle_z$	$|\downarrow\rangle_z$	$|1, -1\rangle$
$|\uparrow\rangle_z$	$|\uparrow\rangle_z$	$|1, +1\rangle$
$|\downarrow\rangle_x$	$\frac{-i}{\sqrt{2}}(|\downarrow\rangle_z - |\uparrow\rangle_z)$	$\frac{-i}{\sqrt{2}}(|1, -1\rangle - |1, +1\rangle)$
$|\uparrow\rangle_x$	$\frac{1}{\sqrt{2}}(|\downarrow\rangle_z + |\uparrow\rangle_z)$	$\frac{1}{\sqrt{2}}(|1, -1\rangle + |1, +1\rangle)$
$|\downarrow\rangle_y$	$\frac{1}{\sqrt{2}}e^{i\pi/4}(|\downarrow\rangle_z - i\,|\uparrow\rangle_z)$	$\frac{1}{\sqrt{2}}e^{i\pi/4}(|1, -1\rangle - i\,|1, +1\rangle)$
$|\uparrow\rangle_y$	$\frac{1}{\sqrt{2}}e^{-i\pi/4}(|\downarrow\rangle_z + i\,|\uparrow\rangle_z)$	$\frac{1}{\sqrt{2}}e^{-i\pi/4}(|1, -1\rangle + i\,|1, +1\rangle)$

Atomic readout

The atomic analysis angle is defined by the polarisation of the readout pulse (χ), resulting in a a bright $|B\rangle$ and dark state $|D\rangle$ for the atom. Table B.3 lists these states for six polarisations.

Table B.3: **Readout pulse polarisation and respective atomic bright $|B\rangle$ and dark state $|D\rangle$.**

χ	$|B\rangle$	$|D\rangle$
L	$|\downarrow\rangle_z$	$|\uparrow\rangle_z$
R	$|\uparrow\rangle_z$	$|\downarrow\rangle_z$
H	$\frac{1}{\sqrt{2}}(|\downarrow\rangle_z + |\uparrow\rangle_z)$	$\frac{-i}{\sqrt{2}}(|\downarrow\rangle_z - |\uparrow\rangle_z)$
V	$\frac{-i}{\sqrt{2}}(|\downarrow\rangle_z - |\uparrow\rangle_z)$	$\frac{1}{\sqrt{2}}(|\downarrow\rangle_z + |\uparrow\rangle_z)$
D	$\frac{1}{\sqrt{2}}e^{-i\pi/4}(|\downarrow\rangle_z + i\,|\uparrow\rangle_z)$	$\frac{1}{\sqrt{2}}e^{i\pi/4}(|\downarrow\rangle_z - i\,|\uparrow\rangle_z)$
A	$\frac{1}{\sqrt{2}}e^{i\pi/4}(|\downarrow\rangle_z - i\,|\uparrow\rangle_z)$	$\frac{1}{\sqrt{2}}e^{-i\pi/4}(|\downarrow\rangle_z + i\,|\uparrow\rangle)$

Bibliography

1. Einstein, A., Podolsky, B. & Rosen, N. Can quantum-mechanical description of physical reality be considered complete? *Physical Review* **47,** 777 (1935).

2. Bell, J. S. On the Einstein Podolsky Rosen paradox. *Physics* **1,** 195 (1964).

3. Freedman, S. J. & Clauser, J. F. Experimental test of local hidden-variable theories. *Physical Review Letters* **28,** 938 (1972).

4. Aspect, A., Dalibard, J. & Roger, G. Experimental test of Bell's inequalities using time-varying analyzers. *Physical Review Letters* **49,** 1804 (1982).

5. Hensen, B. *et al.* Loophole-free Bell inequality violation using electron spins separated by 1.3 kilometres. *Nature* **526,** 682–686 (2015).

6. Giustina, M. *et al.* Significant-loophole-free test of Bell's theorem with entangled photons. *Physical Review Letters* **115,** 250401 (2015).

7. Shalm, L. K. *et al.* Strong loophole-free test of local realism. *Physical Review Letters* **115,** 250402 (2015).

8. Rosenfeld, W. *et al.* Event-ready Bell test using entangled atoms simultaneously closing detection and locality loopholes. *Physical Review Letters* **119,** 010402 (2017).

9. Li, M.-H. *et al.* Test of local realism into the past without detection and locality loopholes. *Physical Review Letters* **121,** 080404 (2018).

10. Feynman, R. P. Simulating physics with computers. *International Journal of Theoretical Physics* **21,** 467–488 (1982).

11. Bloch, I., Dalibard, J. & Nascimbene, S. Quantum simulations with ultracold quantum gases. *Nature Physics* **8,** 267–276 (2012).

12. Georgescu, I. M., Ashhab, S. & Nori, F. Quantum simulation. *Reviews of Modern Physics* **86,** 153 (2014).

13. Greiner, M., Mandel, O., Esslinger, T., Hänsch, T. W. & Bloch, I. Quantum phase transition from a superfluid to a Mott insulator in a gas of ultracold atoms. *Nature* **415,** 39–44 (2002).

14. Deutsch, D. Quantum theory, the Church–Turing principle and the universal quantum computer. *Proceedings of the Royal Society of London. A. Mathematical and Physical Sciences* **400,** 97–117 (1985).

15. DiVincenzo, D. P. The physical implementation of quantum computation. *Fortschritte der Physik: Progress of Physics* **48,** 771–783 (2000).

16. Nielsen, M. A. & Chuang, I. Quantum computation and quantum information. *Cambridge University Press* (2010).

17. Shor, P. W. Algorithms for quantum computation: discrete logarithms and factoring. *Proceedings 35th annual symposium on foundations of computer science, IEEE,* 124–134 (1994).

18. Arute, F. *et al.* Quantum supremacy using a programmable superconducting processor. *Nature* **574,** 505–510 (2019).

19. Giovannetti, V., Lloyd, S. & Maccone, L. Advances in quantum metrology. *Nature Photonics* **5,** 222–229 (2011).

20. Degen, C. L., Reinhard, F & Cappellaro, P. Quantum sensing. *Reviews of Modern Physics* **89,** 035002 (2017).

21. Ludlow, A. D., Boyd, M. M., Ye, J., Peik, E. & Schmidt, P. O. Optical atomic clocks. *Reviews of Modern Physics* **87,** 637 (2015).

22. Pirandola, S., Bardhan, B. R., Gehring, T., Weedbrook, C. & Lloyd, S. Advances in photonic quantum sensing. *Nature Photonics* **12,** 724–733 (2018).

23. Gisin, N., Ribordy, G., Tittel, W. & Zbinden, H. Quantum cryptography. *Reviews of Modern Physics* **74,** 145 (2002).

24. Muller, A., Breguet, J & Gisin, N. Experimental demonstration of quantum cryptography using polarized photons in optical fibre over more than 1 km. *Europhysics Letters* **23,** 383 (1993).

25. Chen, Y.-A. *et al.* An integrated space-to-ground quantum communication network over 4,600 kilometres. *Nature* **589,** 214–219 (2021).

26. Kimble, H. J. The quantum internet. *Nature* **453,** 1023 (2008).

27. Wehner, S., Elkouss, D. & Hanson, R. Quantum internet: A vision for the road ahead. *Science* **362,** eaam9288 (2018).

28. Bennett, C. H. *et al.* Teleporting an unknown quantum state via dual classical and Einstein-Podolsky-Rosen channels. *Physical Review Letters* **70,** 1895 (1993).

29. Bouwmeester, D. *et al.* Experimental quantum teleportation. *Nature* **390,** 575–579 (1997).

30. Dür, W., Briegel, H.-J., Cirac, J. I. & Zoller, P. Quantum repeaters based on entanglement purification. *Physical Review A* **59,** 169 (1999).

31. Briegel, H.-J., Dür, W., Cirac, J. I. & Zoller, P. Quantum repeaters: the role of imperfect local operations in quantum communication. *Physical Review Letters* **81,** 5932 (1998).

32. Duan, L.-M., Lukin, M. D., Cirac, J. I. & Zoller, P. Long-distance quantum communication with atomic ensembles and linear optics. *Nature* **414,** 413–418 (2001).

33. Ladd, T. D. *et al.* Quantum computers. *Nature* **464,** 45–53 (2010).

34. Fitzsimons, J. F. Private quantum computation: an introduction to blind quantum computing and related protocols. *npj Quantum Information* **3,** 1–11 (2017).

35. Barz, S. *et al.* Demonstration of blind quantum computing. *Science* **335,** 303–308 (2012).

36. Komar, P. *et al.* A quantum network of clocks. *Nature Physics* **10,** 582–587 (2014).

37. Mayers, D. & Yao, A. Quantum cryptography with imperfect apparatus. *Proceedings 39th Annual Symposium on Foundations of Computer Science,* 503–509 (1998).

38. Acín, A. *et al.* Device-independent security of quantum cryptography against collective attacks. *Physical Review Letters* **98,** 230501 (2007).

39. Pironio, S. Device-independent quantum key distribution secure against collective attacks. *New Journal of Physics* **11,** 045021 (2009).

40. Murta, G., van Dam, S. B., Ribeiro, J., Hanson, R. & Wehner, S. Towards a realization of device-independent quantum key distribution. *Quantum Science and Technology* **4,** 035011 (2019).

41. Heshami, K. *et al.* Quantum memories: emerging applications and recent advances. *Journal of Modern Optics* **63,** 2005–2028 (2016).

42. Simon, C. *et al.* Quantum memories. *The European Physical Journal D* **58,** 1–22 (2010).

43. Volz, J. *et al.* Observation of entanglement of a single photon with a trapped atom. *Physical Review Letters* **96,** 030404 (2006).

44. Blinov, B., Moehring, D., Duan, L.-M. & Monroe, C. Observation of entanglement between a single trapped atom and a single photon. *Nature* **428,** 153 (2004).

45. Duan, L.-M. & Monroe, C. Colloquium: Quantum networks with trapped ions. *Reviews of Modern Physics* **82,** 1209 (2010).

46. Lukin, M. D., Yelin, S. F. & Fleischhauer, M. Entanglement of atomic ensembles by trapping correlated photon states. *Physical Review Letters* **84,** 4232 (2000).

47. Kuzmich, A *et al.* Generation of nonclassical photon pairs for scalable quantum communication with atomic ensembles. *Nature* **423,** 731 (2003).

48. Sangouard, N., Simon, C., De Riedmatten, H. & Gisin, N. Quantum repeaters based on atomic ensembles and linear optics. *Reviews of Modern Physics* **83,** 33 (2011).

49. Kurtsiefer, C., Mayer, S., Zarda, P. & Weinfurter, H. Stable solid-state source of single photons. *Physical Review Letters* **85,** 290 (2000).

50. Santori, C., Fattal, D., Vučković, J., Solomon, G. S. & Yamamoto, Y. Indistinguishable photons from a single-photon device. *Nature* **419,** 594 (2002).

51. Childress, L. I., Taylor, J. M., Sørensen, A. & Lukin, M. D. Fault-tolerant quantum repeaters with minimal physical resources and implementations based on single-photon emitters. *Physical Review A* **72,** 052330 (2005).

52. Kutluer, K., Mazzera, M. & de Riedmatten, H. Solid-state source of nonclassical photon pairs with embedded multimode quantum memory. *Physical Review Letters* **118,** 210502 (2017).

53. Laplane, C., Jobez, P., Etesse, J., Gisin, N. & Afzelius, M. Multimode and long-lived quantum correlations between photons and spins in a crystal. *Physical Review Letters* **118,** 210501 (2017).

54. Ritter, S. *et al.* An elementary quantum network of single atoms in optical cavities. *Nature* **484,** 195 (2012).

55. Hofmann, J. *et al.* Heralded entanglement between widely separated atoms. *Science* **337,** 72–75 (2012).

56. Bernien, H. *et al.* Heralded entanglement between solid-state qubits separated by three metres. *Nature* **497,** 86–90 (2013).

57. Hucul, D. *et al.* Modular entanglement of atomic qubits using photons and phonons. *Nature Physics* **11,** 37–42 (2015).

115

58. Humphreys, P. C. *et al.* Deterministic delivery of remote entanglement on a quantum network. *Nature* **558,** 268–273 (2018).

59. Wilk, T., Webster, S. C., Kuhn, A. & Rempe, G. Single-atom single-photon quantum interface. *Science* **317,** 488–490 (2007).

60. Brekenfeld, M., Niemietz, D., Christesen, J. D. & Rempe, G. A quantum network node with crossed optical fibre cavities. *Nature Physics* **16,** 647–651 (2020).

61. Reiserer, A. Colloquium: Cavity-enhanced quantum network nodes. *Reviews of Modern Physics* **94,** 041003 (2022).

62. Schupp, J *et al.* Interface between trapped-ion qubits and traveling photons with close-to-optimal efficiency. *PRX Quantum* **2,** 020331 (2021).

63. Körber, M. *et al.* Decoherence-protected memory for a single-photon qubit. *Nature Photonics* **12,** 18 (2018).

64. Bar-Gill, N., Pham, L. M., Jarmola, A., Budker, D. & Walsworth, R. L. Solid-state electronic spin coherence time approaching one second. *Nature Communications* **4,** 1–6 (2013).

65. Bluvstein, D. *et al.* A quantum processor based on coherent transport of entangled atom arrays. *Nature* **604,** 451–456 (2022).

66. Zhong, M. *et al.* Optically addressable nuclear spins in a solid with a six-hour coherence time. *Nature* **517,** 177–180 (2015).

67. Ballance, C., Harty, T., Linke, N., Sepiol, M. & Lucas, D. High-fidelity quantum logic gates using trapped-ion hyperfine qubits. *Physical Review Letters* **117,** 060504 (2016).

68. Gaebler, J. P. *et al.* High-fidelity universal gate set for be 9+ ion qubits. *Physical Review Letters* **117,** 060505 (2016).

69. Madjarov, I. S. *et al.* High-fidelity entanglement and detection of alkaline-earth Rydberg atoms. *Nature Physics* **16,** 857–861 (2020).

70. Stephenson, L. *et al.* High-rate, high-fidelity entanglement of qubits across an elementary quantum network. *Physical Review Letters* **124,** 110501 (2020).

71. Kalb, N. *et al.* Entanglement distillation between solid-state quantum network nodes. *Science* **356,** 928–932 (2017).

72. Pompili, M. *et al.* Realization of a multinode quantum network of remote solid-state qubits. *Science* **372,** 259–264 (2021).

73. Welte, S. *et al.* A nondestructive Bell-state measurement on two distant atomic qubits. *Nature Photonics* **15,** 504–509 (2021).

74. Schlosser, N., Reymond, G., Protsenko, I. & Grangier, P. Sub-poissonian loading of single atoms in a microscopic dipole trap. *Nature* **411,** 1024–1027 (2001).

75. Schlosser, N., Reymond, G. & Grangier, P. Collisional blockade in microscopic optical dipole traps. *Physical Review Letters* **89,** 023005 (2002).

76. Kuhr, S. *et al.* Deterministic delivery of a single atom. *Science* **293,** 278–280 (2001).

77. Cooper, A. *et al.* Alkaline-earth atoms in optical tweezers. *Physical Review X* **8,** 041055 (2018).

78. Norcia, M., Young, A. & Kaufman, A. Microscopic control and detection of ultracold strontium in optical-tweezer arrays. *Physical Review X* **8,** 041054 (2018).

79. Daiss, S. *et al.* A quantum-logic gate between distant quantum-network modules. *Science* **371,** 614–617 (2021).

80. Barredo, D., De Léséleuc, S., Lienhard, V., Lahaye, T. & Browaeys, A. An atom-by-atom assembler of defect-free arbitrary two-dimensional atomic arrays. *Science* **354,** 1021–1023 (2016).

81. Labuhn, H. *et al.* Tunable two-dimensional arrays of single Rydberg atoms for realizing quantum Ising models. *Nature* **534,** 667–670 (2016).

82. Endres, M. *et al.* Atom-by-atom assembly of defect-free one-dimensional cold atom arrays. *Science* **354,** 1024–1027 (2016).

83. Isenhower, L *et al.* Demonstration of a neutral atom controlled-NOT quantum gate. *Physical Review Letters* **104,** 010503 (2010).

84. Wilk, T. *et al.* Entanglement of two individual neutral atoms using rydberg blockade. *Physical Review Letters* **104,** 010502 (2010).

85. Saffman, M., Walker, T. G. & Mølmer, K. Quantum information with Rydberg atoms. *Reviews of Modern Physics* **82,** 2313 (2010).

86. Welte, S., Hacker, B., Daiss, S., Ritter, S. & Rempe, G. Photon-mediated quantum gate between two neutral atoms in an optical cavity. *Physical Review X* **8,** 011018 (2018).

87. Covey, J. P., Madjarov, I. S., Cooper, A. & Endres, M. 2000-times repeated imaging of strontium atoms in clock-magic tweezer arrays. *Physical Review Letters* **122,** 173201 (2019).

88. Bernien, H. *et al.* Probing many-body dynamics on a 51-atom quantum simulator. *Nature* **551,** 579–584 (2017).

89. Ebadi, S. *et al.* Quantum phases of matter on a 256-atom programmable quantum simulator. *Nature* **595,** 227–232 (2021).

90. Zaske, S. *et al.* Visible-to-telecom quantum frequency conversion of light from a single quantum emitter. *Physical Review Letters* **109,** 147404 (2012).

91. Ates, S. *et al.* Two-photon interference using background-free quantum frequency conversion of single photons emitted by an InAs quantum dot. *Physical Review Letters* **109,** 147405 (2012).

92. De Greve, K. *et al.* Quantum-dot spin–photon entanglement via frequency downconversion to telecom wavelength. *Nature* **491,** 421 (2012).

93. Ikuta, R. *et al.* Wide-band quantum interface for visible-to-telecommunication wavelength conversion. *Nature Communications* **2,** 537 (2011).

94. Ikuta, R. *et al.* Polarization insensitive frequency conversion for an atom-photon entanglement distribution via a telecom network. *Nature Communications* **9,** 1997 (2018).

95. Bock, M. *et al.* High-fidelity entanglement between a trapped ion and a telecom photon via quantum frequency conversion. *Nature Communications* **9,** 1998 (2018).

96. Yu, Y. *et al.* Entanglement of two quantum memories via fibres over dozens of kilometres. *Nature* **578,** 240–245 (2020).

97. Lago-Rivera, D., Grandi, S., Rakonjac, J. V., Seri, A. & de Riedmatten, H. Telecom-heralded entanglement between multimode solid-state quantum memories. *Nature* **594,** 37–40 (2021).

98. Weber, M. Quantum optical experiments towards atom-photon entanglement. *PhD Thesis, Ludwig-Maximilians-Universität München* (2005).

99. Volz, J. Atom-photon entanglement. *PhD Thesis, Ludwig-Maximilians-Universität München* (2006).

100. Rosenfeld, W. Experiments with an entangled system of a single atom and a single photon. *PhD Thesis, Ludwig-Maximilians-Universität München* (2008).

101. Henkel, F. Photoionisation detection of single Rb-87 atoms using channel electron multipliers. *PhD Thesis, Ludwig-Maximilians-Universität München* (2011).

102. Hofmann, J. Heralded atom-atom entanglement. *PhD Thesis, Ludwig-Maximilians-Universität München* (2014).

103. Ortegel, N. State readout of single rubidium-87 atoms for a loophole-free test of Bell's inequality. *PhD Thesis, Ludwig-Maximilians-Universität München* (2016).

104. Burchardt, D. A rigorous test of Bell's inequality and quantum teleportation employing single atoms. *PhD Thesis, Ludwig-Maximilians-Universität München* (2017).

105. Krug, M. Ionization based state read out of a single Rb-87 atom. *PhD Thesis, Ludwig-Maximilians-Universität München* (2018).

106. Redeker, K. Entanglement of single rubidium atoms: from a Bell test towards applications. *PhD Thesis, Ludwig-Maximilians-Universität München* (2020).

107. Garthoff, R. Efficient single photon collection for single atom quantum nodes. *PhD Thesis, Ludwig-Maximilians-Universität München* (2021).

108. Weber, M., Volz, J., Saucke, K., Kurtsiefer, C. & Weinfurter, H. Analysis of a single-atom dipole trap. *Physical Review A* **73**, 043406 (2006).

109. Rosenfeld, W., Berner, S., Volz, J., Weber, M. & Weinfurter, H. Remote preparation of an atomic quantum memory. *Physical Review Letters* **98**, 050504 (2007).

110. Henkel, F. *et al.* Highly efficient state-selective submicrosecond photoionization detection of single atoms. *Physical Review Letters* **105**, 253001 (2010).

111. Rosenfeld, W. *et al.* Towards high-fidelity interference of photons emitted by two remotely trapped Rb-87 atoms. *Optics and Spectroscopy* **111**, 535–539 (2011).

112. Rosenfeld, W., Volz, J., Weber, M. & Weinfurter, H. Coherence of a qubit stored in Zeeman levels of a single optically trapped atom. *Physical Review A* **84**, 022343 (2011).

113. Schwonnek, R. *et al.* Device-independent quantum key distribution with random key basis. *Nature Communications* **12**, 2880 (2021).

114. Reinl, A. Trap for Single Atoms. *Master Thesis, Ludwig-Maximilians-Universität München* (2022).

115. Metcalf, H. J. & Van der Straten, P. Laser cooling and trapping of neutral atoms. *Wiley Online Library* (2007).

116. Foot, C. J. Atomic physics. *Oxford University Press* (2005).

117. Grimm, R., Weidemüller, M. & Ovchinnikov, Y. B. Optical dipole traps for neutral atoms. *Advances in Atomic, Molecular, and Optical Physics* **42**, 95–170 (2000).

118. Hummel, T. Increasing photon collection efficiency for generating long-distance entanglement of atoms. *Master Thesis, Ludwig-Maximilians-Universität München* (2018).

119. Seubert, M. Analyzing and optimizing the process of single photon collection. *Master Thesis, Ludwig-Maximilians-Universität München* (2020).

120. Eppelt, S. Optimization of an atom-atom quantum network link using machine learning. *Master Thesis, Ludwig-Maximilians-Universität München* (2021).

121. Hong, C.-K., Ou, Z.-Y. & Mandel, L. Measurement of subpicosecond time intervals between two photons by interference. *Physical Review Letters* **59,** 2044 (1987).

122. Rosenfeld, W *et al.* Towards long-distance atom-photon entanglement. *Physical Review Letters* **101,** 260403 (2008).

123. Clauser, J. F., Horne, M. A., Shimony, A. & Holt, R. A. Proposed experiment to test local hidden-variable theories. *Physical Review Letters* **23,** 880 (1969).

124. Tuchendler, C., Lance, A. M., Browaeys, A., Sortais, Y. R. & Grangier, P. Energy distribution and cooling of a single atom in an optical tweezer. *Physical Review A* **78,** 033425 (2008).

125. Koschmieder, P. Efficient control of magnetic fields in single atom experiments. *Master Thesis, Ludwig-Maximilians-Universität München* (2019).

126. Taray, D. Towards increasing atomic coherence times with a standing wave dipole trap. *Master Thesis, Ludwig-Maximilians-Universität München* (2020).

127. Zhou, Y. *et al.* Robust quantum memory for atom-photon entanglement over 101 km optical fiber. *To be published* (2023).

128. Alt, W. *et al.* Single atoms in a standing-wave dipole trap. *Physical Review A* **67,** 033403 (2003).

129. Bennett, C. H. & Brassard, G. Quantum cryptography: Public key distribution and coin tossing. *Theoretical Computer Science* **560,** 711 (2014).

130. Ekert, A. K. Quantum cryptography based on Bell's theorem. *Physical Review Letters* **67,** 661663 (1991).

131. Elliott, C. & Yeh, H. DARPA quantum network testbed. *Final technical report, BBN Technoligies* (2007).

132. Peev, M. *et al.* The SECOQC quantum key distribution network in Vienna. *New Journal of Physics* **11,** 075001 (2009).

133. Sasaki, M. Field test of quantum key distribution in the Tokyo QKD Network. *Optics Express* **19,** 1038710409 (2011).

134. Zhang, Q., Xu, F., Chen, Y.-A., Peng, C.-Z. & Pan, J.-W. Large scale quantum key distribution: challenges and solutions. *Optics Express* **26,** 24260–24273 (2018).

135. Boaron, A. *et al.* Secure quantum key distribution over 421 km of optical fiber. *Physical Review Letters* **121,** 190502 (2018).

136. Schmitt-Manderbach, T. *et al.* Experimental demonstration of free-space decoy-state quantum key distribution over 144 km. *Physical Review Letters* **98,** 010504 (2007).

137. Ursin, R. *et al.* Entanglement-based quantum communication over 144 km. *Nature Physics* **3,** 481–486 (2007).

138. Nauerth, S. *et al.* Air-to-ground quantum communication. *Nature Photonics* **7,** 382–386 (2013).

139. Liao, S.-K. *et al.* Satellite-to-ground quantum key distribution. *Nature* **549,** 43–47 (2017).

140. Liao, S.-K. *et al.* Satellite-relayed intercontinental quantum network. *Physical Review Letters* **120,** 030501 (2018).

141. Xu, F., Ma, X., Zhang, Q., Lo, H.-K. & Pan, J.-W. Secure quantum key distribution with realistic devices. *Reviews of Modern Physics* **92,** 025002 (2020).

142. Barrett, J., Hardy, L. & Kent, A. No signaling and quantum key distribution. *Physical Review Letters* **95,** 010503 (2005).

143. Reichardt, B. W., Unger, F. & Vazirani, U. Classical command of quantum systems. *Nature* **496,** 456–460 (2013).

144. Vazirani, U. & Vidick, T. Fully device-independent quantum key distribution. *Physical Review Letters* **113,** 140501 (2014).

145. Miller, C. A. & Shi, Y. Robust protocols for securely expanding randomness and distributing keys using untrusted quantum devices. *Journal of the ACM* **63,** 1–63 (2016).

146. Arnon-Friedman, R., Dupuis, F., Fawzi, O., Renner, R. & Vidick, T. Practical device-independent quantum cryptography via entropy accumulation. *Nature Communications* **9,** 1–11 (2018).

147. Brunner, N., Cavalcanti, D., Pironio, S., Scarani, V. & Wehner, S. Bell nonlocality. *Reviews of Modern Physics* **86,** 419–478 (2014).

148. Ho, M. *et al.* Noisy preprocessing facilitates a photonic realization of device-independent quantum key distribution. *Physical Review Letters* **124,** 230502 (2020).

149. Zhang, W. *et al.* A device-independent quantum key distribution system for distant users. *Nature* **607,** 687–691 (2022).

150. Nadlinger, D. *et al.* Experimental quantum key distribution certified by Bell's theorem. *Nature* **607,** 682–686 (2022).

151. Liu, W.-Z. *et al.* Toward a photonic demonstration of device-independent quantum key distribution. *Physical Review Letters* **129,** 050502 (2022).

152. Gisin, N. & Thew, R. Quantum communication. *Nature Photonics* **1,** 165–171 (2007).

153. Zapatero, V. *et al.* Advances in device-independent quantum key distribution. *arXiv preprint arXiv:2208.12842* (2022).

154. Niemietz, D., Farrera, P., Langenfeld, S. & Rempe, G. Nondestructive detection of photonic qubits. *Nature* **591,** 570–574 (2021).

155. Gisin, N., Pironio, S. & Sangouard, N. Proposal for implementing device-independent quantum key distribution based on a heralded qubit amplifier. *Physical Review Letters* **105,** 070501 (2010).

156. Kołodyński, J. *et al.* Device-independent quantum key distribution with single-photon sources. *Quantum* **4,** 260 (2020).

157. Zukowski, M., Zeilinger, A., Horne, M. A. & Ekert, A. K. " Event-ready-detectors" Bell experiment via entanglement swapping. *Physical Review Letters* **71** (1993).

158. Zhao, J., Ma, C., Rüsing, M. & Mookherjea, S. High quality entangled photon pair generation in periodically poled thin-film lithium niobate waveguides. *Physical Review Letters* **124,** 163603 (2020).

159. Eberhard, P. H. Background level and counter efficiencies required for a loophole-free Einstein-Podolsky-Rosen experiment. *Physical Review A* **47,** R747 (1993).

160. Giustina, M. *et al.* Bell violation using entangled photons without the fair-sampling assumption. *Nature* **497,** 227–230 (2013).

161. Christensen, B. G. *et al.* Detection-loophole-free test of quantum nonlocality, and applications. *Physical Review Letters* **111,** 130406 (2013).

162. Vivoli, V. C. *et al.* Challenging preconceptions about Bell tests with photon pairs. *Physical Review A* **91,** 012107 (2015).

163. Tsujimoto, Y. *et al.* Optimal conditions for the Bell test using spontaneous parametric down-conversion sources. *Physical Review A* **98,** 063842 (2018).

164. Liu, Y. *et al.* Device-independent quantum random-number generation. *Nature* **562,** 548–551 (2018).

165. Shen, L. *et al.* Randomness extraction from bell violation with continuous parametric down-conversion. *Physical Review Letters* **121,** 150402 (2018).

166. Shalm, L. K. *et al.* Device-independent randomness expansion with entangled photons. *Nature Physics* **17,** 452–456 (2021).

167. Woodhead, E., Acín, A. & Pironio, S. Device-independent quantum key distribution with asymmetric CHSH inequalities. *Quantum* **5,** 443 (2021).

168. Sekatski, P. *et al.* Device-independent quantum key distribution from generalized CHSH inequalities. *Quantum* **5,** 444 (2021).

169. Xu, F., Zhang, Y.-Z., Zhang, Q. & Pan, J.-W. Device-independent quantum key distribution with random postselection. *Physical Review Letters* **128,** 110506 (2022).

170. Xiang, G.-Y., Ralph, T. C., Lund, A. P., Walk, N. & Pryde, G. J. Heralded noiseless linear amplification and distillation of entanglement. *Nature Photonics* **4,** 316–319 (2010).

171. Bruno, N. *et al.* Heralded amplification of photonic qubits. *Optics Express* **24,** 125–133 (2016).

172. Primaatmaja, I. W. *et al.* Security of device-independent quantum key distribution protocols: a review. *arXiv preprint arXiv:2206.04960* (2022).

173. Matsukevich, D., Maunz, P., Moehring, D. L., Olmschenk, S. & Monroe, C. Bell inequality violation with two remote atomic qubits. *Physical Review Letters* **100,** 150404 (2008).

174. Farkas, M., Balanzó-Juandó, M., Łukanowski, K., Kołodyński, J. & Acín, A. Bell nonlocality is not sufficient for the security of standard device-independent quantum key distribution protocols. *Physical Review Letters* **127,** 050503 (2021).

175. Stockill, R. *et al.* Phase-tuned entangled state generation between distant spin qubits. *Physical review letters* **119,** 010503 (2017).

176. Van Leent, T. *et al.* Entangling single atoms over 33 km telecom fibre. *Nature* **607,** 69–73 (2022).

177. Liu, X. *et al.* Heralded entanglement distribution between two absorptive quantum memories. *Nature* **594,** 41–45 (2021).

178. Renner, R. Security of quantum key distribution. *International Journal of Quantum Information* **6,** 1–127 (2008).

179. Tan, E. Y.-Z. *et al.* Improved DIQKD protocols with finite-size analysis. *arXiv preprint arXiv:2012.08714* (2020).

180. Braunstein, S. L. & Pirandola, S. Side-channel-free quantum key distribution. *Physical Review Letters* **108,** 130502 (2012).

181. Fürst, H. *et al.* High speed optical quantum random number generation. *Optics Express* **18,** 13029–13037 (2010).

182. Bancal, J.-D., Redeker, K., Sekatski, P., Rosenfeld, W. & Sangouard, N. Self-testing with finite statistics enabling the certification of a quantum network link. *Quantum* **5,** 401 (2021).

183. Thinh, L. P., de la Torre, G., Bancal, J.-D., Pironio, S. & Scarani, V. Randomness in post-selected events. *New Journal of Physics* **18,** 035007 (2016).

184. Wright, T. A. *et al.* Two-way photonic interface for linking the Sr+ transition at 422 nm to the telecommunication C band. *Physical Review Applied* **10,** 044012 (2018).

185. Bock, M. Polarization-preserving quantum frequency conversion for trapped-atom based quantum networks. *PhD Thesis, Universität des Saarlandes* (2021).

186. Merkel, B., Ulanowski, A. & Reiserer, A. Coherent and Purcell-enhanced emission from erbium dopants in a cryogenic high-Q resonator. *Physical Review X* **10,** 041025 (2020).

187. Uphoff, M., Brekenfeld, M., Rempe, G. & Ritter, S. An integrated quantum repeater at telecom wavelength with single atoms in optical fiber cavities. *Applied Physics B* **122,** 46 (2016).

188. Albota, M. A., Wong, F. N. & Shapiro, J. H. Polarization-independent frequency conversion for quantum optical communication. *JOSA B* **23,** 918–924 (2006).

189. Ramelow, S., Fedrizzi, A., Poppe, A., Langford, N. K. & Zeilinger, A. Polarization-entanglement-conserving frequency conversion of photons. *Physical Review A* **85,** 013845 (2012).

190. Krutyanskiy, V, Meraner, M, Schupp, J & Lanyon, B. Polarisation-preserving photon frequency conversion from a trapped-ion-compatible wavelength to the telecom C-band. *Applied Physics B* **123,** 1–9 (2017).

191. Dudin, Y. O. *et al.* Entanglement of light-shift compensated atomic spin waves with telecom light. *Physical Review Letters* **105,** 260502 (2010).

192. Albrecht, B., Farrera, P., Fernandez-Gonzalvo, X., Cristiani, M. & de Riedmatten, H. A waveguide frequency converter connecting rubidium-based quantum memories to the telecom C-band. *Nature Communications* **5,** 3376 (2014).

193. Krutyanskiy, V *et al.* Light-matter entanglement over 50 km of optical fibre. *npj Quantum Information* **5,** 1–5 (2019).

194. Tchebotareva, A. *et al.* Entanglement between a diamond spin qubit and a photonic time-bin qubit at telecom wavelength. *Physical Review Letters* **123,** 063601 (2019).

195. Boyd, R. W. Nonlinear optics. *Academic Press* (2020).

196. Shoji, I., Kondo, T., Kitamoto, A., Shirane, M. & Ito, R. Absolute scale of second-order nonlinear-optical coefficients. *JOSA B* **14,** 2268–2294 (1997).

197. Zaske, S. Quantum frequency down-conversion of single photons in nonlinear optical waveguides. *PhD Thesis, Universität des Saarlandes* (2013).

198. Pelc, J. S., Langrock, C., Zhang, Q. & Fejer, M. M. Influence of domain disorder on parametric noise in quasi-phase-matched quantum frequency converters. *Optics Letters* **35,** 2804–2806 (2010).

199. Kaiser, F. *et al.* Quantum optical frequency up-conversion for polarisation entangled qubits: towards interconnected quantum information devices. *Optics Express* **27,** 25603–25610 (2019).

200. Rohde, F. *et al.* A diode laser stabilization scheme for 40Ca+ single ion spectroscopy. *Journal of Physics B: Atomic, Molecular and Optical Physics* **43,** 115401 (2010).

201. Zaske, S., Lenhard, A. & Becher, C. Efficient frequency downconversion at the single photon level from the red spectral range to the telecommunications C-band. *Optics Express* **19,** 12825–12836 (2011).

202. Van Leent, T. *et al.* Long-distance distribution of atom-photon entanglement at telecom wavelength. *Physical Review Letters* **124,** 010510 (2020).

203. Cuomo, D., Caleffi, M. & Cacciapuoti, A. S. Towards a distributed quantum computing ecosystem. *IET Quantum Communication* **1,** 3–8 (2020).

204. Maring, N. *et al.* Photonic quantum state transfer between a cold atomic gas and a crystal. *Nature* **551,** 485–488 (2017).

205. Krutyanskiy, V *et al.* Entanglement of trapped-ion qubits separated by 230 meters. *arXiv preprint arXiv:2208.14907* (2022).

206. Luo, X.-Y. *et al.* Postselected entanglement between two atomic ensembles separated by 12.5 km. *Physical Review Letters* **129,** 050503 (2022).

207. Shi, Y., Poh, H. S., Ling, A. & Kurtsiefer, C. Fibre polarisation state compensation in entanglement-based quantum key distribution. *Optics Express* **29,** 37075–37080 (2021).

208. Langenfeld, S., Thomas, P., Morin, O. & Rempe, G. Quantum repeater node demonstrating unconditionally secure key distribution. *Physical Review Letters* **126,** 230506 (2021).

209. Dordević, T. *et al.* Entanglement transport and a nanophotonic interface for atoms in optical tweezers. *Science* **373,** 1511–1514 (2021).

210. Ramette, J. *et al.* Any-to-any connected cavity-mediated architecture for quantum computing with trapped ions or Rydberg arrays. *PRX Quantum* **3,** 010344 (2022).

211. Huie, W., Menon, S. G., Bernien, H. & Covey, J. P. Multiplexed telecommunication-band quantum networking with atom arrays in optical cavities. *Physical Review Research* **3,** 043154 (2021).

212. Steck, D. A. Rubidium 87 D line data. *Available online at http://steck.us/alkalidata* (2021).

Acknowledgments

I would like to thank everyone that, in one way or another, contributed to this work. In particular, Harald Weinfurter, for providing an inspiring and productive work environment, being approachable, and supporting social activities. Moreover, for his high standards—witnessed by, for example, the large sets of constructive comments to paper drafts, especially at moments when all other authors already seemed to be satisfied, or the simple request to repeat a 4-month measurement, which, when looking back, was time was well spent. At last, for his trust, for instance, by letting me present our work on conferences were I was, by far, the most junior speaker.

A special thanks to my colleagues with whom I spent most time in the lab. Including Robert Garthoff, my one and only office mate and the PhD student that started before me on the atom project. In the first place for the very careful design, construction, and implementation of the improved photon collection optics, enabling many experiments presented in this thesis, but also for making conferences to Barcelona or Bad Honnef more amusing. Wei Zhang, the motivated postdoc that joined the group half a year after me, thereby providing me the opportunity to introduce our experiment to someone that not yet had the knowledge about our specific implementation, while having a broader physics background. Thank you for never being more than 50% full and, when leaving the lab for weeks in row at 03:00 in the morning, always agreeing with me that this measurement will be *the* measurement. Matthias Bock, of course, for the design and construction of the quantum frequency conversion system and thereby laying the basis for a very successful collaboration. But also for the drive and dedication he brought to the lab during the multiple stays in Munich. This drive is not limited to the lab environment, however, and is one of his great strengths, demonstrated by our ski trip on June(!) 2nd or our visit to the Katapult. Lastly, Florian Fertig, for his graphical design skills that greatly improved the appearance of our papers (and this thesis) and, certainly, for managing Atom 2 during the multi-month measurement periods of the long fibre atom-atom entanglement experiments.

I want to thank all that assisted me during my first steps in the lab, as well as all that I assisted during theirs. For instance, Wenjamin Rosenfeld, for his many years spent on the experiment and balancing my sometimes too optimistic views. Yiru Zhou, for her dedication to the experiments. Kai Redeker, for his guidance during my first atom-atom entanglement measurements, conceptual understanding of device-independent QKD, vacuum skills, and great memory. Pooja Malik, for inviting the complete team for dinner or Oktoberfest after winning conference poster prizes—indeed, plural. Sebastian Eppelt, for his pro-active attitude, wide interests, and proper programming skills. And, at last, Daniel Burchardt, for his parallel efforts to introduce the experiment and Munich to me. In addition, I would like to thank the master students on our experiment: Timon Hummel, Paul Koschmieder, Matthias Seubert, Derya Taray, and Anastasia Reinl.

Collaborations with the research groups from both Charles Lim (National University of

Singapore) and Christoph Becher (University of Saarland) greatly attributed to the results presented in this thesis, for which I would like to thank them.

Furthermore, I would like to thank my fellow students working on other experiments in our research group, notably, for making the Monday morning meetings interesting and the yearly Ringberg retreats enjoyable, for example, through Schafkopf, four-handed chess, hikes, and so on. This includes Jan Dziewior, Carlotta Versmold, Florian Huber, Lukas Knips, and Jasmin Meinecke from the Garching team, the Cryptos Peter Freiwang, Lukas Knips (again), Rengaraj Govindaraj, Michael Auer, and Adomas Baliuka, and, of course, the last Diamond, Martin Zeitlmair. In addition, and despite not having worked with them directly, I would like to thank the other PhD students that worked on atom project in the last two decades for developing many of the methods employed in this work.

I want to thank our experimental physics chair Theodor W. Hänsch and all the chair-members, including the support staff Nicole Schmidt, Anton Scheich, and, of course, Head of Office Gabriele Gschwendtner.

Last but not least, I want to thank my old friends from Amsterdam and new friends from Munich for reminding me that there is life outside of the lab. I want to thank my sisters— Mandy, for paving the way, Daphne, for our similarities, and Inge, for championing family values. I want to thank my parents for *always* being there, but especially for providing me with seemingly unlimited opportunities and unconditional support. And finally, I want to thank Carolin, for her motivation, inspiration, and encouragement, in particular, for doing so day after day, thereby enabling this work.